High-Resolution Observations of Wind Conditions in a Ski-Flying Hill — A Fairness Assessment of the Wind Factor Compensation

Jonas Harestad

Master's Thesis in Meteorology

March 15, 2023

Contents

0.1 Acknowledgements

Wow, where to start... Even though this master project was an innovative idea I had almost three years ago, and I have become my own "boss" (which I am certainly not comfortable with), there are some key persons that I would not have been able to reach my goal without.

First and foremost I would like to express my deepest appreciation to my supervisor Joachim Reuder for encouraging me to cultivate my interest in ski jumping. I remember one of the first supervisor meetings with him that he insisted that I should go all in for my first idea of the ski-jumping hill "thing". Even on the days I was on the verge of giving up this plan due to irrelevant fears he supported me and assured me that there was nothing to be afraid of. He also gave me the ability to set up a campaign in the world's largest ski-flying hill in Vikersund using state-of-the-art meteorological instruments. Honestly, I cannot put words on how thankful I am. I would also like to extend my deepest gratitude to my co-supervisor Stephan Kral for putting a lot of effort into giving me feedback and advice on my work, both in the weekly supervisor meetings and in the MET group meetings every Thursday. He also helped out in the planning of the campaign in Vikersund. He also joined me on the setup later on. Further, I want to thank Christiane Duscha for helping me (and teaching me) with LiDAR setup in Vikersund, and data processing afterward. I would also like to thank Shokoufeh Malekmohammadi, Jan Markus Diezel, and Mauro Ghirardelli for joining me and helping with the setup/recovery of the instruments in Vikersund. Thank you Anak Bhandary for helping out with technical instrumental work and logistics. I would also like to give a huge thanks to all the members of the MET group for all the discussions in the weekly meetings, and of course, also to my fellow students for being so sociable and nice. I would also like to thank Bjørn Espen Hovde and Ole Gunnar Fidjestøl for the opportunity to use Vikersund Ski-flying hill as the observation site for this master thesis. Thank you for letting me stay in the hut beside the judge tower, and for getting the opportunity to join the Raw Air final in Vikersund from Mar 17 to Mar 19. I can't wait!

There are so many people that deserve to be in this list. My family, including my mother Sissel, my father Ingebrigt, and my two sisters Stine and Maren have been there supporting me from day one, both in context to the master, but also the socialization in my earlier life. It is no secret that my mother is a "bauta" in my life, and I call her whenever I feel sad, stressed out, and even happy. In addition, I would like to thank my friends in Stavanger and Bergen for cheering me on, giving me motivation, and believing in me. Thank you Angelina for the late-night reading gatherings that ended up playing Yahtzee. Thank you Eirin for the warmth you give me when we are together. Thank you Michael for spending hours reading through my thesis and give me improvement advice. I could ram up forever. Thank you to all my true friends, you know who you are!

Jonas Harestad
Bergen, Norway, Mar 14, 2023

0.2 Abstract

The aim of this thesis is to evaluate fairness connected to the Wind Factor (WF) compensation used by the International Ski Federation in ski jumping competitions by wind measurements of higher spatiotemporal resolution than those used during competitions. There are two main research questions (RQ) linked to this thesis; one of which is based on the understanding of the current idealized wind factor (WF) model, and under which conditions the linear estimates of the mean along-slope component of the wind speed ($\overline{v_{tan}}$) hold and vice versa. The other focus is whether more advanced estimates of the wind vector **u**, including sidewind and slope perpendicular aerodynamic forcing, would improve fairness in ski jumping. More specifically, this study tries to provide answers to the following RQs:

- Is it possible to capture persistent events of significant deviations between an interpolated $\overline{v_{tan}}$ and a directly measured v_{tan}, and if so, can these deviations be associated with certain mean wind conditions?
- Does the collected data capture significant variations in the tilt of the measured v_{tan}, which evidently depends on the horizontal wind direction (WD), and would an advanced WF compensation including this effect be more appropriate?

To provide answers to the RQ above, an observational campaign was conducted in Vikersund ski-flying hill in the period October 12-26, 2021. Three sonic anemometers were strategically placed on the knoll of Vikersundbakken, and a scanning LiDAR of type WindCube 100s (WC100s) scanned in a plane that intersected the sonic anemometers from around the hill size (HS) position close to the bottom of the hill. The evaluation of the current WF compensation is done by describing the non-linear effects (not represented in WF) as a function (F1), where the output value is a real number scalar in ms^{-1} being the deviation in the FIS current $\overline{v_{tan}}$ (F) based on the observed true **u**. F1 includes two terms. One of the terms is simply the deviation of a reproduction of the FIS estimate of $\overline{v_{tan}}$ and the observed v_{tan} in the center of the hill (referred to as v_{diff}), and the other is an aerodynamic effect caused by anomalies in the slope-perpendicular component w_r, referred to as the wind vector tilt effect (v_{θ_v}). The latter term is approximated by a first-order Taylor expansion around the axis of the mean wind direction.

The data collected during the campaign in Vikersund reveals that this ski-flying slope is influenced by a tangential wind speed of larger magnitude in the center of the hill compared to its cross-sectional boundaries (reference positions). The mean wind speed in the center of the hill was typically about 5-10 % higher than at the reference positions. The largest cross-sectional wind shears, producing the largest expected $\mathrm{v}_{diff} \approx -0.3\ \mathrm{ms}^{-1}$, were found in relatively close to along-slope conditions where v_{ref} < -1.5 ms^{-1}. The standard deviation of the mean wind did also show a dependency on the expected v_{diff}, where the small standard deviations were associated with a v_{diff} close to zero until $\mathrm{v}_{ref} \sim$ -1.8 ms^{-1}. The mean tilt effect term v_{θ_v} was positive for v_r < -0.3 ms^{-1}, and close to zero otherwise. The maximum value $\mathrm{v}_{\theta_v} \approx 0.6\ \mathrm{ms}^{-1}$ was found for $\mathrm{v}_r \approx$ -1.8 ms^{-1}, which compensated for the negative v_{diff} resulting in a total F1 $\approx 0.4\ \mathrm{ms}^{-1}$ peaking at $\mathrm{v}_{ref} \approx 0.4\ \mathrm{ms}^{-1}$. Based on the results we suggest a requirement of a 10-min wind containing well above 68 % of the 10 s time window standard deviation of v_{tan} lower than 0.2 ms^{-1}.

Chapter 1

Introduction

Ski jumping is one of the outdoor sports where meteorological conditions play a significant role for the competitor's performance. In particular the hill-parallel upslope-/downslope component, leading to headwind (HW) or tailwind (TW) conditions for the jumper, is known to effect the jump length significantly. Before 2010, the ski jumper's final score was only a function of the jump length and style (*Czarnecki*, 2020). In the 2010/2011 season, the International Ski Federation (FIS) introduced a wind factor (WF) compensation based on observed wind conditions close to the ski jumpers' path. The WF is designed to award points to the ski jumpers according to an expected jump length effect associated with the actual wind conditions (*Jung et al.*, 2021a). The jump length effect is the expected modification in the achieved jump length in HW/TW conditions. HW/TW is commonly used to describe wind conditions with an upslope/-downslope tangential wind speed (v_{tan}) parallel to the jumping hill. One noteworthy factor is that v_{tan} is the true tangential wind speed in the path of the ski jumper. This value is difficult to measure and estimate appropriately during competitions, especially under turbulent conditions.

The WF is computed as a score compensation dependent on the observed mean tangential wind speed ($\overline{v_{tan}}$) around the time period the jumper is in the air. For ski jumping competitions in large hills (LH), $\overline{v_{tan}}$ is a weighted mean based on wind measurements of seven anemometers (five for normal hills (NH) and ten for ski-flying hills (FH)) located on both sides of the jumping hill (*Mikko and Juha*, 2022; *Pietschnig et al.*, 2020). The anemometers measure three-dimensional (3D) wind with a sampling frequency of 4 Hz, according to confidential wind data received from SWISS Timing from the World Championships held in March 2021, in Vikersund, Norway. The WF is dependent on hill size (HS), meaning that a typical NH ends up with a WF of 6.4 pts (per unit change in wind), whereas a typical FH is awarded 10.8 pts (*Aldrin*, 2015). Initially, WF was a completely linear function of v_{tan}, which was in 2013 changed to a piece-wise linear function including a factor of 1.21 for TW conditions. This was done after a study conducted by *Virmavirta and Kivekäs* (2012a), using data simulation to estimate the jump length effect as a function of $\overline{v_{tan}}$. Through this study, it was concluded that the jump length effect was significantly larger for TW conditions compared to HW conditions. Another study by *Jung et al.* (2021a) estimates the coefficients of drag and lift to be used in such simulations.

In addition to the HS, there is a jump length mark called the calculation point (K), which is defined to represent the required achieved jump length to reach 60 length

points in a certain ski jumping hill (*FIS*, 2022). The K position is dependent on the HS, and jump lengths longer/shorter than K are awarded ± 1.2 points per meter (pts m^{-1}) in ski-flying hills (K $>$ 185 m), ± 1.8 pts m^{-1} in large hills (110 m $\leq$ K $<$ 185 m), and ± 2.0 pts m^{-1} in normal hills (85 m $\leq$ K $<$ 110 m). The style for each individual jump is evaluated by five professional judges, watching the jump live from the judge tower. Each individual judge can award the jumper with jury marks ranging from 0 to 20 (*Aldrin*, 2015). The score achieved from jump length is shown to have more impact on the total score than the jury marks; especially since the judge's individual style points typically only range between 10 to 20 points. Score values outside this range are rare and typically given if the ski jumper falls, whereas a regular jump typically ranges between 15 and 20 points. Jury marks correlate positively with both jump length and $\overline{v_{tan}}$, which means the $\overline{v_{tan}}$ is more influential on the total score than if the jury evaluated the style in a certain wind condition(*Czarnecki*, 2020). To illustrate this conundrum, imagine if a stably strong competitor is unlucky and experiences the strongest TW in the competition. The current leader jumped much further, but the wind conditions were much better. Assume the two jumps were identical except for the wind condition, and the WF based on the JL effect was perfectly fair. Even though the two performances were identical, the competitor with the longest jump is expected to receive the highest total score due to the biased style evaluation.

The motivation for this thesis builds on the current method by FIS to estimate a tangential wind speed which is supposed to be sufficiently close to v_{tan}. This estimation has been difficult to address correctly, and meta-analytic statistics evaluated in the two seasons from 2016 to 2018 done by *Pietschnig et al.* (2020) have shown that the total score still correlates negatively with WF, and with great significance. Despite estimates indicating this mean correlation, there are still large variations of the correlation evaluated in individual races. However, further statistical analysis of $\overline{v_{tan}}$ in the center of the hill, together with the boundary observations available in FIS competitions, can be utilized to provide quality control (QC). The QC can be utilized to provide a quality assurance (QA) method, where the purpose is designed to negate the mentioned mean negative correlation, and, more importantly, the variance of it. By conducting micro-meteorological observations with a finer spatial resolution than FIS', one can increase their knowledge of the true spatial distribution of the wind vector in a certain ski-jumping hill and potentially exploit this knowledge to increase fairness in the sport of ski jumping.

The objective of this work is to investigate whether a sufficient solution can be reached for the judgment of ski jumping competitions. With this in mind, the question becomes whether or not this task is manageable within a reasonable cost. The most common adjustment method of the WF compensation system has been to obtain data simulation of jumps in certain conditions to identify shortcomings in the current WF compensation system (*Jung et al.*, 2021a). The purpose of this study is to find a solution of how the fairness in ski jumping can be improved by searching for malfunctions in the WF compensation system connected to deviations between $\overline{v_{tan}}$ and v_{tan}. While also investigating the effects of the differential tilt on the wind vector. With this in mind, the aim is to answer the following research questions (RQ):

- Is it possible to capture persistent events of significant deviations between an interpolated $\overline{v_{tan}}$ and a directly measured v_{tan}, and if so, can these deviations be

associated with certain mean wind conditions?

- Does the collected data capture significant variations in the tilt of the measured v_{tan}, which evidently depends on the horizontal wind direction (WD), and would an advanced WF compensation including this effect be more appropriate?

The main method to provide the potential answers is a statistical analysis of the 3D wind in the across-hill center of the knoll (together with two boundary measurements). Additional remote sensing wind measurements are meant to catch the 2D spatial distribution of the flow in a linear plane above the hill surface.

The content of this thesis follows with background (2), which is supposed to grasp the relevant theory for this study. This chapter has two main parts, where the first part is about methods used in micrometeorology to understand different small-scale events in the atmosphere. The second part is about the fairness challenge in ski jumping, where details about the WF compensation and advantages/disadvantages of the use of it in the evaluation of fairness. The thesis continues with the instrumentation setup in the campaign in Vikersund, Norway (Chapter 3), which includes instrumentation. This is followed by methods (Chapter 4), which contain three sections. The first section is about data processing and the second is about a tangential wind speed function which is supposed to estimate an error in $\overline{v_{tan}}$ used in WF. The third section is an additional analysis that compares a remote sensing observation of v_{tan} by LiDAR with observations of v_{tan} by a sonic anemometer. Results in Chapter 5 present the meteorological observations and the spatial distribution of the flow and its consistency. This is followed by discussion and conclusions in Chapter 7. Finally, we present the concluding remarks and outlook in Chapter 7, followed by appendices A.

.

Chapter 2

Background

2.1 Dynamics of the Atmosphere

The wind is a fluid (air) motion relative to the earth's surface (**u**) that originates from forcing by gradients in air pressure due to differential heating from the earth's surface or other heating sources. According to Newton's 2^{nd} law, every object changing momentum (mass$\times$velocity) experiences a net force, where the total kinetic energy changes when absolute speed changes (*Ha and Kim*, 2020). The net acceleration is the sum of every force acting on the object. In the context of fluids, all movements originate from the gravity force and the normal force acting against it. An air parcel with no vertical acceleration is supported by the air parcel underneath it such that the sum of gravity and normal force equals zero. As soon as the parcel is displaced vertically, the normal force of one or more air parcels was not sufficiently large to withstand the gravitational pull on it. This is more commonly known as the Archimedes principle, that the air parcel displaces a weight of the underlying air parcel equal to its own weight (*Tonboe et al.*, 2021). Upward vertical forcing is in fluid theory commonly called buoyancy, which is a net force upwards due to the upward pressure gradient force being larger than the constant downward gravitational pull.

Given no pressure gradient, the evolution of **u** depends on its relative speed to the underlying rotating earth and to the surrounding fluid. There are also viscous/frictional forces between the air molecules which (always) act as a sink of the fluid speed. One must note that **u** is a velocity in a none-inertial frame of reference, which means that a constant **u** is accelerated seen from the inertial frame of reference (from space). Since the value of **u** is of interest in the study of fluid dynamics, it must be applied fictitious accelerations to Newton's 2^{nd} law.

Due to the Earth being a rotating sphere, the tangential velocity of the rotation must have a horizontal shear everywhere. This is responsible for the well-known Coriolis effect. Coriolis is a fictitious acceleration pointing perpendicular to **u**, and its magnitude is a function of latitude and wind speed. Since it is perpendicular to the momentum vector, it cannot do any form of mechanical work on anything (*Macchiavelli et al.*, 2020).

Forcing in fluid dynamics can be described mathematically by a non-linear inhomogeneous differential equation known as the Navier-Stokes equation. This equation is

devised by mathematician Leonard Euler in the 18^{th} century using the Newtons 2^{nd} law in a non-accelerating reference frame and assuming that the fluid is incompressible. Claude-Louis Navier and George Gabriel Stokes worked on this by introducing a viscosity (friction) term in the equation (*Hosch*, 2009).

$$\frac{\partial \mathbf{v}}{\partial t} + \mathbf{v} \cdot \nabla \mathbf{u} = -g\mathbf{k} - f\mathbf{k} \times \mathbf{u} - \frac{1}{\rho}\nabla p + \nu \nabla^2 \mathbf{u} \tag{2.1}$$

The two first terms in 2.1 represent the material (total) derivative of the three-dimensional fluid motion **u**. The three components (u,v,w) represent three perpendicular directions in space, where w usually represents the vertical component for the fluid motion (out of the earth's center). This component is often neglected in synoptic scale meteorology, and it becomes more and more important for smaller scales due to the increasing interest in topographic forcing.

The second term, $f\mathbf{k} \times \mathbf{v}$, is the effect of rotation (Coriolis effect). This term is in general not crucial on similar scales as a ski flying hill compared to the pressure gradient force.

The last term on the right-hand side (RHS) is viscous or frictional forces, which is proportional to the divergence of the momentum flux. In the nocturnal boundary layer (NBL), however, $\frac{\partial}{\partial z}\left(\overline{u_a' w'}\right)$ is decreasing with height until it reaches zero at approximately $\frac{2}{3}$ of the NBL - height.

Computational fluid dynamics (CFD) is a set of methods using the equations of motion to predict the fluid motion one time step into the future. Unsurprisingly, there is no analytical solution to the equations of motion, so the method is (only) state-of-the-art numerical prediction. *Zikanov* (2010) provides a definition of CFD as follows:

"CFD (computational fluid dynamics) is a set of numerical methods applied to obtain approximate solutions of problems of fluid dynamics and heat transfer."

This set of methods applies to different schemes to approximate an appropriate solution of the fluid motion. This scheme is a numerical set of equations that is idealized for its purpose. For instance, the synoptic scale weather prediction includes completely different assumptions to parameterize the equation than a completely different spatiotemporal scaled prediction include. In the former scale, it is often done approximations by neglecting vertical motion (hydrostatic balance) and viscous effects (no divergence), whereas a non-hydrostatic scheme for mesoscale modeling includes the effects of vertical motion.

Moving into the mesoscale and microscale regime, the importance of the topographic representation becomes more important. The idea behind this is to compute where the strongest/ weakest flows usually go if we have wind from a certain direction. Hopefully, this will help us to give a better estimate/picture of a closer true value of the flow field on the path of the ski jumper.

2.2 Microscale Wind Variability

High frequent meteorological/wind observations in complex terrain are often associated with boundary layer meteorology. Depending on what is investigated, more specific scales are defined when choosing the spatiotemporal resolution and range of the observations. The microscale is defined as phenomena such as turbulence with space scales smaller than 3 km and temporal scales shorter than about 1 h (*Stull*, 1988a). Some typical atmospheric events are classified within spatiotemporal scales in Fig. 2.1.

Micrometeorologists typically investigate details of meteorological variables in the surface layer. The surface layer consists of the smallest eddies in the atmosphere, and turbulence energy has started cascading to heat energy. As described by the Kolmogorov scale explained in Fig. 2.1b, the fluid in these small eddies has been in larger eddies and experienced growth in turbulence energy, and also through the inertial subrange experiencing no/small growth/cascade. On this scale, deterministic description and forecasting are virtually impossible. To understand the surface layer better, micrometeorologists have developed three primary avenues for exploring their subject (*Stull*, 1988a):

- stochastic methods
- similarity theory
- phenomenological classifications

The stochastic methods use statistical parameters, such as mean and standard deviation, which can be described in a histogram or in a continuous probability density function. Similarity theory creates an expected evolution and its uncertainty under a given atmospheric condition, based on an empirical fit of large observed data sets. The phenomenological classification takes advantage of classifying the largest eddies, such as thermals or katabatic flows (*Stull*, 1988b).

Under statically (very) stable conditions and a nocturnal boundary layer (NBL) height oscillating in the height of the study area, the signal from a longer time scale eddy might generate turbulence and change mean wind conditions. Oscillations like this originate from forcing giving a statically stable air parcel potential energy. In the context of a steep slope, this typically happens under statically (very) stable conditions with wind conditions such that the air has enough momentum to reach the top of it.

The strongly stable NBL supports the formation of gravity waves, but the effect of increasing stability also decreases its amplitude. The statically stable air will have a negative contribution to turbulence during night time, but the mixed layer from the day becomes a narrower residual layer above the stable boundary layer disconnected to the surface with higher friction than the stable boundary layer it now is feeling (*Stull*, 1988a). At this height, the wind is forced to accelerate to a nocturnal low-level jet. This enhances turbulence because of the strong vertical wind shear close to the boundary between the residual layer and the stable boundary layer. (*Markowski and Richardson*, 2010) In Fig. 2.2, the evolution of the nocturnal low-level jet based on a mean daily evolution measured by a wind profiler in Vici, Oklahoma in June-July 2006, is an illustration of how the momentum close to the surface is lost to the residual layer above

during NBL (referred to as Stable Boundary Layer in 2.2). In a large enough ski jumping hill, the generation of nocturnal low-level jets after sunset might be the direct cause of mixing the relatively cold inversion layer beneath the hill up towards the hilltop. In such a scenario, the TW conditions with warm and less dense air are rapidly replaced by HW conditions with denser air. If a competition is held under those conditions, the change in wind conditions will of course be a challenge for the jury, mainly because the wind corridor is on the positive edge. Another factor, not considered in the WF compensation, is the differential air density due to the change in the average temperature on the hill. The jump length effect is only a function of tangential wind forcing, but the "true" jump length effect is a function of the whole 3D wind and also air density. More details about the total aerodynamic forcing of a ski jumper can be found in 2.4.

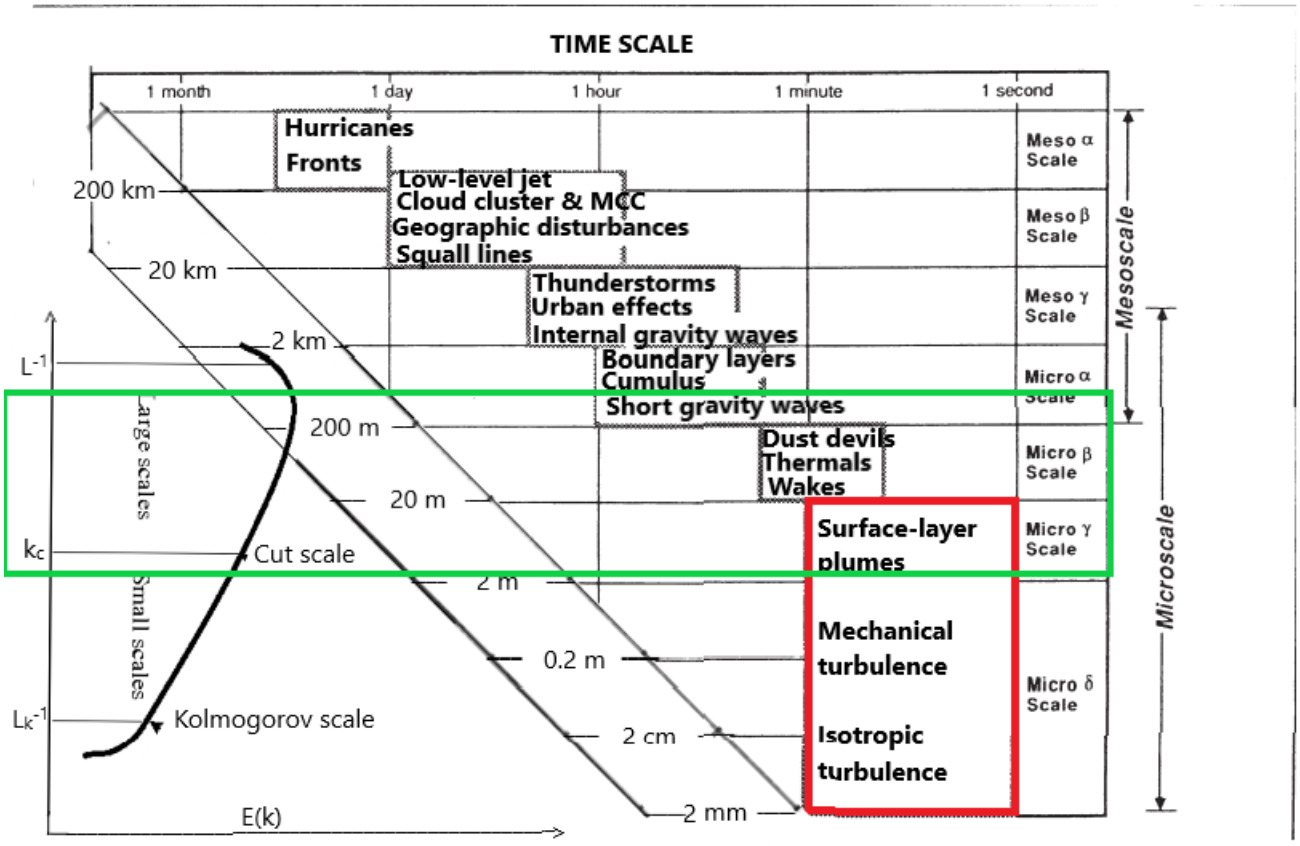

Figure 2.1: (a): Typical atmospheric events as a function of atmospheric time - and length scale. (b): Loglog-plot of a typical turbulence energy spectrum of the time series from a sonic anemometer under turbulent conditions. The internal subrange (marked in blue) approaches a slope of $\frac{5}{3}$ where the energy cascade overtakes the energy feeding from the eddies. The green box highlights the length scales examined in this master thesis.

Changes in weather conditions of larger scales can also be fatal for competitions, and sometimes the final round is canceled. This happened in the ski flying competition in Kulm on Feb 16, 2020. During this competition, variable wind conditions with oscillations between HW and TW were replaced with consistent and strong TW for the last three competitors in the final round (*Dolhar and Greger*, 2022). Luckily, such

lower frequent changes in wind conditions are often somehow predictable; both if it is a diurnal signal like drainage flow generation after sunset, but also if it is a synoptic scale signal.

2.2.1 Turbulence Kinetic Energy (TKE)

To arrange ski jump competitions, there is set a range (corridor) of $\overline{v_{tan}}$ which is not more than 2 ms^{-1} wide, which is often between -1 ms^{-1} and 1 ms^{-1} or close to that range. A range of v_{tan} within a time window is connected to its standard deviation, which also is connected to turbulence. The standard deviation of the wind vector, described in 2.3.1, is a direct measure of the total amount of turbulent kinetic energy (TKE) per unit mass. This quantity is preferably as low as possible under competition. To understand the concept of how turbulence generates and cascades, we present the generation of TKE as a differential equation ($\overline{e} = TKE/m$) (*Stull*, 1988a)

$$\begin{aligned}
&\frac{1}{m}\frac{D}{Dt}(TKE) = \frac{1}{2m}\frac{D}{Dt}(\sigma_{\mathbf{u}}^2) \\
&= \frac{g}{\overline{\theta_v}}\left(\overline{w'\theta_v'}\right) - \overline{u_i'u_j'}\frac{\partial \overline{U}_i}{\partial x_j} - \frac{\partial\left(\overline{u_j'e'}\right)}{\partial x_j} - \frac{1}{\overline{\rho}}\frac{\partial\left(\overline{u_i'p'}\right)}{\partial x_i} - \varepsilon \\
&\qquad\qquad\qquad\qquad\qquad\qquad\qquad\qquad\qquad\qquad \text{i, j} = 1, 2, 3 \\
&\qquad\qquad\qquad\qquad\qquad\qquad\qquad\qquad\qquad\qquad (u_1, u_2, u_3) = (u, v, w), \quad (2.2)
\end{aligned}$$

where the operator $\frac{D}{Dt}$ is the Lagrangian material derivative which includes the local rate of change and the influence on it by advection of the quantity by **u**. The variables $\overline{\rho}$ and **p'** represent mean air density and air pressure anomaly respectively. The letter **g** represents the gravitational acceleration, $\overline{\theta_v}$ is the potential virtual temperature, which often can be replaced by T_v in a stable surface layer.

- The first term on the right-hand side (r.h.s) is turbulence generation by buoyancy forcing. On fair weather days, this term typically switches from positive to negative after sunset, which cools the air above the surface and contributes as a sink on the TKE budget.
- The second term is shear production. This term is typically the dominating term in the surface layer, where the vertical component of this term dominates the horizontal components when approaching the surface.
- Third term is turbulent transport. This one is similar to the advection term, but the transport is by transient eddies, not the mean wind. The amplitude of this term through an eddy period is a function of total TKE, but the long-term mean contribution by this term is zero.
- Fourth term is the pressure correlation, which describes how TKE is redistributed by pressure anomalies. It is usually small compared to the other terms and neglected in many turbulent numerical models.

- Fifth term is the consumption of TKE by dissipation, which is the conversion from TKE to heat or other energy forms.

In the surface layer when wind speeds are high enough, the TKE is approximately the difference between the shear generation and dissipation, especially during nighttime when the buoyancy term is negative and small. The depth of the surface layer is defined as being 10% of the ABL height (*Stull*, 1988a), which typically is shallow in the transition from the mixed surface layer to the stable boundary layer (see Fig. 2.2).

In this study, we investigate the turbulent flow on a steep slope (34°). Compared to a flat surface, the TKE budget terms are often quite similar on a steep slope. However, there are some substantial differences during transition periods, which originate from the buoyancy term. On a steep hill facing the sun during sunrise/sunset, the buoyancy term changes sign to positive/negative. The steeper the hill is, the faster rate of change of the buoyancy, which induces upslope/drainage flows. The diurnal movement of air parcels up/down a hill is associated with the gain/loss of the potential energy of the system, where the largest transition rate happens immediately after sunrise/sunset.

The transition to potential energy can be partially observed by a rapid change in TKE on slopes. Observations of TKE in Inn Valley, Austria, on a 27° slope on a clear night (0400 LT) in July 2015 caught an increase in TKE before sunrise due to a drop in the buoyancy term generating drainage flow (*Goger et al.*, 2018). The drainage signal is also captured from observations on the valley floor by a substantial increase of the buoyancy term due to the intrusion of cold air from the mountain tops. The fact that this happened several hours after sunset indicates the event was not a diurnal signal, but likely an effect caused by i.e cloud cover reduction.

2.2.2 Diurnal Periods

In order to get a ski jumping competition as fair as possible, it is plausible to look for periods of stationary HW/TW conditions. If the weather is fair, the diurnal radiative forcing is what dominates the total flow field. This makes the winds in the hill stably change as a function of time.

During daytime, the surface heats up due to radiative forcing, and a slope facing the sun with a certain tilt heats up even faster given that the elevation of the sun relative to the heating surface is closer to perpendicular than the horizontal plane. As a response, the overlaying air heats up in contact with the surface and gains buoyancy. This makes the air rise. After a while, the pressure will be lower on the surface, and higher on the mountain top, so the circulation tends to have a horizontal component towards the high pressure (mountain top). The sum of the upward buoyant force and the horizontal pressure force points approximately toward the mountaintop parallel to the topography. In the night the whole picture is typically reversed, and it is the downslope flows that dominate the mountainside (*Rampanelli et al.*, 2004).

2.2.3 The Role of the Gravity Force

Looking at the dynamics of air parcels and particles in the air, there are two key forces contributing to vertical acceleration. The difference between the negative gravity force and the vertical pressure gradient is the main contributor to air parcel acceleration. On hydrostatic weather prediction models, often used for synoptic scale NWP these two forces are balanced

$$\frac{\partial p}{\partial z} = -\rho g, \tag{2.3}$$

where no vertical accelerations are possible. Since the air parcels always search for an equilibrium state the factor of two adjacent air parcels is often close to 1. However, in turbulent air pressure perturbations are typically in the order of 0.04 Pam^{-1} for WS$\approx 2\ ms^{-1}$, and propagates in the mean wind direction above the surface disturbance (*Mohr et al.*, 2017). For isotropic turbulence, the vertical pressure perturbations are in the same order as the horizontal. According to the study from *Mohr et al.* (2017), pressure perturbations are close to proportional to wind speeds above the canopy.

Fluctuations in the topography perpendicular wind component (w_r) are typically contributed by the surface heat flux, the horizontal shear of w_r, pressure correlation, and the dissipation rate (see eq. 2.2).

In a slope, we have the gravity dependency in both the wind component in the along-slope direction (v_r *or* v_{tan}) and the perpendicular w_r direction. Since the first term on R.H.s of eq. 2.2 is typically positive close to the surface during daytime, and largest when the sun is facing the slope, this term generates turbulence in both w_r and v_r direction. The mean part of the surface heat flux contribution ($m \cdot g\overline{w}$) in the generation of TKE is also positive, giving a mean positive w component, indicating a positive $\overline{v_{tan}}$.

The kinetic energy for negative $\overline{v_{tan}}$ is typically peaking in the first hours after sunset. This is mostly due to the peak in negative surface heat flux contributing to the largest accelerations in w_r and v_{tan}, which is related to the cooling rate of the surface layer (*Villagrasa et al.*, 2013). Air density rises due to the radiative cooling and the potential energy difference between the valley floor and the hilltop peaks. The peak in the drainage flow is close to the time when the temperature gradient between the surface and the center of the surface layer is the largest. This can be variable from slope to slope, and it depends on the orientation of the hill compared to the sun's position, surface albedo/emissivity, and surface heat conductivity.

Vertical displacement of colder air due to mesoscale advection of the stable boundary layer air is also gaining potential energy to the local energy budget. This is now caused by advection of cold air from the stable boundary layer below, which the surface heat flux now will contribute in the opposite direction of the gravity force. However, the result is an oscillation with the frequency as given by the Brünt Väisala relation in eq. 2.9. It is important to note that oscillations follow the slope and surface friction might slow this frequency down substantially (related to wind along-slope wind speed and surface roughness).

2.3 Turbulence Statistics

One of the primary avenues in micrometeorology is the stochastic approach (*Stull*, 1988a). The transient nature of the turbulence is not well understood, and empiric observations of the behavior of the turbulent fluid might be helpful in finding recognizable patterns which can be used in parameterization methods. We want to characterize the transient and mean state of properties in the air to be able to evaluate the WF compensation in a characteristic period. Statistical parameters such as small-scale means, standard deviations, covariances, and grade of normal distribution (skewness, kurtosis) might be helpful to answer the RQ in 1. Wind gust parameters might also be of interest in this study. The wind gust parameters provide information about the period/amplitude distribution of a defined running mean time window.

2.3.1 Statistical Measures

The statistical mean/median/mode, standard deviation, and covariance are fundamental statistical measures used in fluid dynamics. They are used to describe the empirical behavior of atmospheric variables and also The mean value is a measure of an expected value of a given set of samples as the sum of the set normalized by the cardinality (N) of the set (*Stull*, 1988a).

$$\overline{X} = \frac{1}{N}\sum_{i=1}^{N} X_i \tag{2.4}$$

Where $\overline{X}$ is the mean of N samples of X. The variable X can be sampled representing either a time or a spatial point or in some cases both time and space (Lagrangian dynamics).

The median is also a measure of an expected value of the set, but now as the data point on index $\frac{N+1}{2}$ in the sorted set. If N is an even number, the median becomes the mean of the two indexes $\frac{N}{2}$ and $\frac{N}{2}+1$.

A box standard deviation is a measure of the variability of the set. The standard deviation is defined as (*Stull*, 1988a)

$$\sigma = \sqrt{\sigma^2} = \overline{X'^2}^{\frac{1}{2}} = \sqrt{\frac{1}{N}\sum_{i=1}^{N}(X_i - \overline{X})^2}, \tag{2.5}$$

where σ is the standard deviation of the data X, and N is the number of data points σ yields for. This standard deviation could be nicely used in time series of non-circular meteorological variables such as temperature, fluid motion, precipitation, radiation, and pressure. For circular measures, such as wind direction (especially horizontal), a classical standard deviation is described in eq. 2.5 could be very misleading. Especially if a significant part of the data points has values close to the $0/2\pi$ direction. To fix this problem, (*Turner*, 1986) looked at twenty different functions using variables obtained in a single-pass of wind data. *Turner* (1986) found the best function by testing the maximum and minimum errors of the methods in conditions of true σ_a ranging from 10 to 100°. The Yamartino method performed well with relatively small errors (maximum

1.2° for $\sigma_a \approx 100^\circ$). The standard deviation in horizontal wind direction following the Yamartino method is defined as

$$\sigma_a = sin^{-1}(\varepsilon)\left[1-\left(1-\frac{2}{\sqrt{3}}\right)\varepsilon^3\right],$$

$$\varepsilon = \sqrt{1-(\overline{sin(WD_a)})^2-(\overline{cos(WD_a)})^2}$$

$$sin(WD_a) = \frac{u}{\sqrt{u^2+v^2}}$$

$$cos(WD_a) = \frac{v}{\sqrt{u^2+v^2}}. \tag{2.6}$$

The letters u and v represent the two horizontal wind components. In micrometeorology, the variance, σ^2, is directly related to the TKE, and also Turbulence Intensity (TI). TKE is the kinetic energy created by the transient eddies, and the mean TKE per unit mass can be written as (*Stull*, 1988a)

$$\frac{TKE}{m} = \frac{1}{2}\overline{(u'^2+v'^2+w'^2)} \tag{2.7}$$

where u', v' and w' are the instantaneous perturbation of a predefined mean state of the 3D velocity components. TI is a measure of the variability normalized by a predefined mean state, which is the standard deviation normalized by the mean wind speed and is a key factor that affects energy production (especially individual wind turbines and wind farms) (*Mataji*, 2022). This is a more common statistical parameter in height well above the atmospheric surface layer (ASF), since it kind of acts as an overestimation of the lowest wind speeds influenced by shear or buoyancy production.

The covariance is a measure of the covariability between two sets (S_1 and S_2) of equal cardinality. It is mainly used when determining fluxes and stress (*Stull*, 1988b). If a scatter of S_1 and S_2 are perfectly linear the covariance becomes simply the product of σ_1, σ_2, and the sign of the covariance. The covariance is a measure that can be positive and negative which gives a measure of how the two variables depend on each other. The sign of the scalar is positive when the two variables depend on each other in the same direction and vice versa. The covariance is given by the average product of two variables A and B as the following (*Stull*, 1988a)

$$covar(A,B) = \frac{1}{N}\sum_{i=0}^{N-1} A'_i B'_i = \overline{A'B'} \tag{2.8}$$

The covariance is a measure of the correlation between the two variables A and B. There are three cases to look closer to

- $\overline{A'B'} = 0$: No correlation. The variables are independent of each other. Two cubed dice (A and B), designed to give equal probability on every six outcomes, thrown $N \to \infty$ times is expected to have no correlation. This is because the events are stochastic and not dependent.
- $\overline{A'B'} > 0$: Positive correlation. The variables seem to depend on each other such that an increase in A is associated with an increase in B and vice versa. A group of people where ages range from 0-20 years (A) and their height (B) are expected to correlate positively.

- $\overline{A'B'} < 0$: Negative correlation. The variables seem to depend on each other such that an increase in A is associated with a decrease in B and vice versa. Cloud cover fraction (low clouds) (A) and incoming shortwave radiation to the surface (B) are expected to correlate negatively.

The correlation is a statistical measure used as a tool to find the significance of the dependency between observed events. In the atmosphere, observations of spatial gradients of a correlation between two variables (fluxes) are often used to create an expected behavior in certain weather conditions. The similarity theory method in turbulence uses empirical measures of the atmospheric variables to represent unresolved processes (*Stull*, 1988b). The purpose of doing this is to make models perform better due to high-quality empirical expectations of variables in unresolved positions. The similarity theory uses non-dimensional parameters derived from the Buckingham Pi method to describe atmospheric relations with as few degrees of freedom as possible.

In the context of ski jumping, the covariance can sometimes be used to predict an expected duration of certain atmospheric conditions. For example, in SBL, such as strong inversion events with cold and heavy air in the valley and warmer air above, the duration of HW is fairly predictable when we know the temperature difference in the valley and at a predefined height level above this. If we know the height difference between the surface layer in the valley and the position in the slope where temperature (T) and 3D wind are measured, we have an estimate of T in the valley. Vertically displaced stable air parcels caused by orographic forcing horizontal wind generate short gravity waves. The length and time scale is ranging between 200 m - 500 m and 60 s - 3600 s illustrated in 2.1. Duration of the upward flow is dependent on the background vertical gradient in virtual potential temperature $\theta_v(T,z)$, where the Brunt Vaisala relation gives the frequency

$$N = \sqrt{-\frac{g}{\rho_0}\rho_z} \tag{2.9}$$

which is, when assuming unsaturated air, proportional to the square root of the background virtual potential temperature gradient $\overline{\theta_v}$ (*Markowski and Richardson*, 2010)

$$N = \sqrt{\frac{g}{\overline{\theta_v}}}\sqrt{\frac{\partial\overline{\theta_v}}{\partial z}} = \sqrt{\frac{g}{\overline{\theta_0}}}\sqrt{\frac{\partial\overline{\theta}}{\partial z}} \tag{2.10}$$

where g is the gravitation acceleration and ρ is the density of the air depending on the temperature T and the pressure p. θ_0 and $\overline{\theta}$ is the potential temperature of the environment at a predefined z position z_0 and the potential temperature of the environment as a function of vertical displacement z. Air masses forced up above the boundary layer height have gained $g \cdot H$ total energy per unit mass. Since it is much denser than the surroundings gravity will pull the parcel towards the center of Earth until it reaches the position where the surroundings are denser than the parcel. A mesoscale short gravity wave is formed, and we have two or more atmospheric layers oscillating with frequency N after induced, and the correlation between the properties of the air masses and the wind is often very high.

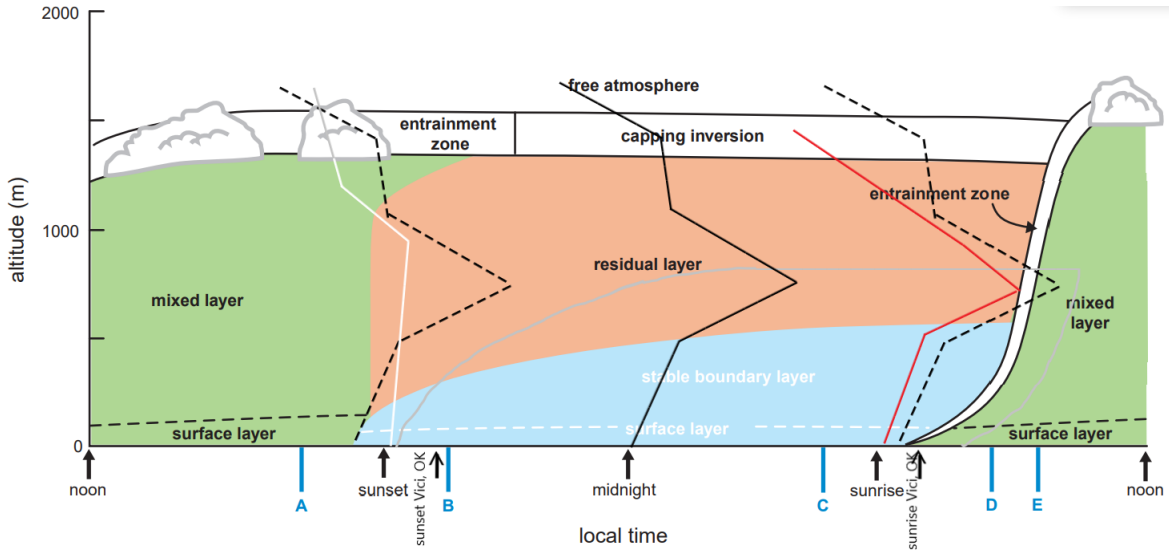

Figure 2.2: The boundary layer in relatively tranquil conditions, consisting of a mixed layer, nocturnal boundary layer (NBL), and residual layer. NBL is characterized by sporadic turbulence, e.g low-level jets. ***Solid lines****: Vertical profiles from (Markowski and Richardson, 2010) of mean* $\overline{U_a}$ *in Vici, Oklahoma, US, measured by wind profiler during summer 2006. The surface value is positioned at the LT of the yielding* $\overline{U_a}$*.* ***Dashed lines****: 0200 LT profile (compared to the afternoon/morning profiles). Vertical profiles are drawn over a schematic drawing of the diurnal evolution of the ABL, which also comes from (Markowski and Richardson, 2010)*

2.3.2 Stochastic Probability Distribution

Given that a sample distribution is normally distributed, 68.27% of the data has an absolute difference to the mean less than a standard deviation, and 95.45% of the data falls within two standard deviations. In a turbulent period without a significant trend, the probability distribution is close to a normal distribution due to the strong stochastic forcing dominating the lower-frequency eddies (*Stull*, 1988a). If we have a perfect normal distribution, there is only stochastic forcing, and the eddy forcing sums up to zero. A histogram of the frequency of a normally distributed variable (in this case, the wind vector) follows the equation

$$f(\mathbf{U}) = (2 \cdot \pi)^{-\frac{1}{2}} \sigma_{\mathbf{U}}^{-1} \cdot e^{-\frac{1}{2}\left(\frac{\mathbf{U}-\overline{\mathbf{U}}}{\sigma_{\mathbf{U}}}\right)^2}, \tag{2.11}$$

where $\mathbf{U}$ is the wind vector with three components (u,v,w), $\sigma_{\mathbf{U}}$ is its standard deviation, and e is Eulers' natural number. The area bounded by f($\mathbf{U}$), the $\mathbf{U}$-ax and the vertical lines $\mathbf{U} = \mathbf{U}_{min}$ and $\mathbf{U} = \mathbf{U}_{max}$ is the relative frequency of occurrence where $\mathbf{U}$ falls within the interval ($\mathbf{U}_{min}$,$\mathbf{U}_{max}$), and this holds for all probability distributions.
The distribution of a variable can be described by a probability density function (PDF), which often follows a log-normal distribution in the surface layer (*Slyz et al.*, 2005). A histogram of wind speed over a period of more than a week is often left skewed $S_{\mathbf{U}} > 0$ due to the diurnal effect present over a surface surrounded by high thermal conductivity and a shallow absorption layer. Night times often have a narrower distribution with lower wind speeds, and day times are more turbulent and also have higher mean wind speeds. The PDF has a characteristic shape given by its skewness and kurtosis, which

is defined as the following (*Muhammad*, 2021)

$$\begin{aligned} sk &= \frac{\sqrt{N^2-N}}{N-2}\frac{N}{\sigma^3}\sum_{i=1}^{N}\left(U_i-\overline{U}\right)^3 \\ ku &= \frac{N}{\sigma^4}\sum_{i=1}^{N}\left(U_i-\overline{U}\right)^4-3, \end{aligned} \tag{2.12}$$

where the factor $\frac{\sqrt{N^2-N}}{N-2}$ defines a Fisher-Person coefficient of skewness, and approaches 1 when N gets large.

2.4 Atmospheric Forcing on a Ski Jumper

The drag and lift produced by a flow are, as previously mentioned, controlled by the relative speed between the airflow and an object in the air. This object could in theory be a parcel containing air containing turbulence and it can also be something with completely different properties, such as a ski jumper. When the air is accelerated, the relative speed between the air and the object changes, and so are the drag and lift.

The vertical wind component, w, can have a large influence on the aerodynamic forcing of a ski jumper. The aerodynamic forcing has the following relation

$$F_d = \frac{1}{2}\rho D\mathbf{w}^2,\ F_l = \frac{1}{2}\rho D\mathbf{w}^2, \tag{2.13}$$

where F_d is the drag forcing parallel to the wind vector **w** and F_l is the lift forcing perpendicular to the drag forcing (see Eq. 1 in *Jung et al.*, 2021b). D and L are the drag - and lift area respectively scaled by drag and lift coefficients c_D and c_L. T he **w** is the airflow velocity in m/s. Drag force can be used to derive 2D acceleration (xz plane) which together with the gravitational forcing $F_g = m\mathbf{g}$ determines the path of the ski jumper. This will be affected by the factors in **equation 4.1**. By increasing the area in which airflow hits underneath the ski jumper, the lift forcing increases and consequently decreases the downward acceleration due to the gravity force. The well-known v-style invented by Jan Boklöv in the late 1980s is an example of a technique to increase the area of attack by the airflow in a way to accelerate the ski jumper upwards (*Maryniak et al.*, 2009).

2.4.1 Micrometeorological Modeling – Similarity Methods or Measurement Resolution Improvements

Modeling of microscale wind evolution requires high-resolution grids and short time steps and requires huge data power per domain volume and time unit. Microscale modeling has been done for .... decades, and in the last two decades, it has become more and more prominent because of the rapid resource and technology development. A state-of-the-art microscale wind model used for almost 30 years until today is WAsP, which is a wind atlas model. WAsP is designed mostly for wind resource mapping, wind farm micro-sitting, and energy estimate purposes (*Carvalho et al.*, 2013). The

model is supposed to predict long-term and high-resolution wind energy in local spots, and the concept of the wind atlas arose from the need to estimate wind energy influencing a bridge with observation inputs only on one side of it.

Numerical prediction of the microscale wind pattern in a ski jumping hill (especially in turbulent conditions) might never be realistic. The scale is simply too small to be able to make appropriate assumptions in order to lower the degree of freedom sufficiently to compute derivatives of meteorological variables numerically. In reality, infinitely many variables to a common challenge in the field of turbulence called the closure problem (*Stull*, 1988a). Our knowledge about computational fluid dynamics (CFD) consists of prognostic equations, which, not surprisingly, do not provide analytical solutions, which force meteorologists to predict the weather numerically. Smaller spatial scales are related to smaller temporal scales in the field of numerical weather prediction (NWP), which makes downscaling to the scale of a ski jumping hill require an astronomically huge amount of computation power. Nevertheless, while wind conditions are within a certain low turbulent corridor, wind observations as boundary conditions in a microscale model might be realistic and usable for ski jumping competitions. The required time window of the modeling is only a few seconds while the ski jumper passes the anemometer in the air, and there are ten boundary condition values to investigate. Given the requirement of low turbulence to use this model, it might not be necessary due to the fact that local isotropy and horizontal homogeneity can often be assumed. If so, a linear interpolation between two across-slope boundary anemometers gives an appropriate estimate of v_{tan}. This creates an expected difference v_{tan}^{diff} as a function of jump length and reference wind estimated from the sides $\overline{v_{tan}}$, which under stable conditions often (but not always) is close to zero. We are not necessarily interested in the total spatial wind energy differences as engineers building bridges would be, but rather in the partial spatial wind energy under certain horizontal mean wind conditions.

In a ski jumping hill, it would make more sense to use only observations. This is because the area of interest is narrow enough to have only three measurements across the hill, and three to five cross-sections along the hill depending on the HS. This is a maximum of 15 anemometers. Unfortunately, non-remotely wind measurements in the middle of the hill are not possible in competitions, which is why such observations outside competitions might be in use for the prediction of $\overline{v_{tan}}$. This data can be used to provide statistical analysis of the spatial distribution of $\overline{v_{tan}}$ and vertical component in classes of the horizontal wind components (u, v).

2.4.2 Wind Conditions in Ski Jumping – a Fairness Challenge

The effect of wind conditions on a ski jumper is complex, but the jump length effect of HW/TW conditions has for a long time been known to be negative/positive. Compared to other outdoor sports, the fairness in ski jumping was evaluated to be much poorer due to the wide range (evaluated over short time periods) of competitors ending top ten (*Czarnecki*, 2020). The unfairness is likely connected to the relatively strong influence on expected jump length due to small changes in wind conditions.

The wind effect on a ski jumper has been debated since 1927 when (*Straumann*, 1927) made an aerodynamic analysis with an analytical model using wind tunnel measurements of lift and drag forces on a ski jumper. A lot of wind tunnel experiments are done in the 20^{th} Century after (*Straumann*, 1927). However, results from these studies are no longer in use because equipment and flight style changed, which includes the groundbreaking V-style invented by Jan Boklöv in 1985 (*Müller et al.*, 1996).

Even though our knowledge of the aerodynamical effect on a ski jumper has been sufficient to understand the jump length effect from v_{rad} for several decades, there has been no compensation for this effect until the wind factor (WF) system was introduced in the 2009/2010 season.

2.4.3 Wind Measurements for Ski Jumping Competitions

In the sport of ski jumping, it is crucial to provide wind measurements with a very high spatiotemporal resolution. This is to be able to estimate the true instantaneous wind forcing, which might deviate substantially within a few meters of radial distance. However, micrometeorological approaches such as similarity theory and stochastic methods can be helpful in the interpolation to estimate a v_{tan} more appropriately, even with similar wind measurement techniques. This requires higher-resolution observations for the area of interest, which does not need to be during a competition, but it is likely that winter-season observations are more reliable than observations in summer. From this observation data, we have knowledge of the more fine-scale spatiotemporal distribution of v_{tan} and are able to construct a potential similarity theory, which can be used in measurements of lower resolution. The reliability of the suggested similarity theory can be evaluated with the stochastic methods.

More specifically, the scale of interest in this study becomes between the micro γ scale and micro β scale, but lower frequent events such as short gravity waves might also be of interest. The spatiotemporal area of interest is indicated as a green box in Fig.2.1a.

Starting from the high standard deviation periods, which typically is not suitable for competitions. Since turbulence in the surface layer often can be approximated to be proportional to mean wind speed This kind of period is most common during the daytime (due to diurnal forcing), which is often associated with the shear production of turbulence is high. The standard deviation can also be high because of synoptic scale features, such as low-pressure systems (i.e fronts) close by, also generating turbulence by wind shears. More details about shear production can be found in 2.2.1. The presence of short gravity waves is difficult to compensate by the current wind factor (WF) described in 2.4.5. Such events typically include two different (and consistent) v_{tan} periods lasting from a minute to around ten minutes.

2.4.4 Wind Factor (WF) Compensation

The idealized WF compensation model is supposed to address the fairness problem in ski jumping by using estimates of $\overline{v_{tan}}$ as input. The $\overline{v_{rad}}$ is measured by anemometers on different sites in the hill, and the mean tangential wind speed is calculated in a predefined measurement time. The chosen anemometer height on its lateral position is based on an expected ski jump curve (*House*, 2022), which is not published and might be very different depending on the hill profile and required inrun speed.

To compensate for the clear jump length effect addressed above, the WF is adding/subtracting a certain amount of points when the observed $\overline{v_{tan}}$ is negative/positive. More precisely, the current WF is a piece-wise linear function where the assumed effect of $\overline{v_{tan}}$ changes depending on its value. The piece-wise function, which becomes a function of $\overline{v_{tan}}$ and anemometer position, has the following form (*Jung et al.*, 2021c; *Mikko and Juha*, 2022)

$$
\begin{aligned}
v_{1tan}^{n\neq 1} &= \quad v_{0tan}^{n\neq 1} \text{ if } v_{0tan}^{n\neq 1} > 0 \\
v_{1tan}^{n\neq 1} &= 1.21 \cdot v_{0tan}^{n\neq 1} \text{ if } v_{0tan}^{n\neq 1} < 0
\end{aligned}
$$

$$
\begin{aligned}
&\text{which for } n = 1: \\
v_{1tan}^{1} &= \quad -v_{0tan}^{1} \text{ if } v_{0tan}^{1} \geq -1 \\
v_{1tan}^{1} &= v_{0tan}^{1} + 2 \text{ if } v_{0tan}^{1} < -1
\end{aligned}
$$

$$n = 1,2,3,4,5, \quad (2.14)$$

where n is the anemometer position of the evaluated $\overline{v_{tan}}$ ordered after jump length position (i.e n=1 is the anemometer closest to the inrun edge). The underscore numbers (0 and 1) represent the measured $\overline{v_{tan}}$ and the adjusted value of it respectively.

The piece-wise equation 2.14 adjusts the jump length effect depending on both the measured tangential wind and the position of the wind measured on the hill. This was not sufficiently taken to account in the first competitions, because WF was computed as a mean of all the ten anemometers. The fact that all the anemometers counted equally was criticized by competitors since the wind conditions in the early flight are crucial for if the ski jumper even reaches the jump distance further than K where the last anemometers measure wind conditions (*Virmavirta and Kivekäs*, 2012b). Data simulations of ski jump paths in LH with HS of 140 m have shown that the first 20 m of the flight experiences a "reverse" jump length effect, where actually TW conditions are advantageous (*Jung et al.*, 2018).

The WF is also dependent on hill size (HS), meaning that a typical NH ends up with a WF of 6.4 pts (per unit change in wind), whereas a typical FH is awarded 10.8 pts (*Aldrin*, 2015).

2.4.5 Measures to Improve Fairness

Initially, WF was a completely linear function of v_{tan}, which was changed to a piecewise linear function including a factor of 1.21 for TW conditions in 2013. This was done after a study conducted by (*Virmavirta and Kivekäs*, 2012a), using data simulation to estimate the JL effect as a function of $\overline{v_{tan}}$. Through this study, it was concluded that the jump length effect was significantly larger for TW conditions compared to HW conditions. After the WF was introduced, a study from (*Pietschnig et al.*, 2020) established that the total score and the wind points (WF) correlated negatively. The results from this study indicate that HW conditions are advantageous, even after the WF was added to the length score. The ideal model has no such correlation in every single race.

Another aspect to take into consideration is that the WF has been shown to perform sufficiently well in stable wind conditions, whereas periods of small changes in v_{tan} are associated with a WF performing poorly. The latter problem arises from poor spatial resolution in the wind measurements, which in the worst case estimates of $\overline{v_{tan}}$ are "reversed" from the true v_{tan}. In such situations, the WF will make the results more unfair than if not used. The competitions held in turbulent conditions make the variation in the performance of WF larger, and sometimes it fails to have an assessment basis.

The poor spatial resolution of the wind measurements is connected to the positions of the 3D anemometers that are too far away from the ski jump trajectory curve. Shortcomings of the WF by FIS have been discussed, and five major challenges were introduced by (*Czarnecki*, 2020):

- **tardiness**: The difference between the mean 5-second average tangential wind and the instantaneous tangential wind at the anemometer position when the ski jumper passes it.
- **Spatial error**: Sensors are not situated in the expected X-position the jumper passes, but on the jump hill boundaries (10-20 meters from the center depending on the Y-position of the anemometers). The uncertainty connected to the WF, which typically compensates for the real wind conditions in $3/4$ jumps, is mostly due to errors connected to the input value $\overline{v_{tan}}$.
- **cross-wind (u) effects on the WF**: WF is a 5 s temporal mean 3D wind vector. When this mean includes a large enough crosswind component, the flow is likely to be higher turbulent due to the more complex terrain across-slope than along-slope. The wind vector is also expected to be more horizontal with a cross-wind component since the steepest slope is (often) along the hill.
- **Wind Corridor**: The range of $\overline{v_{tan}}$ is simply too wide. After the WF was introduced, the fairness has been more sensitive to changes in wind conditions due to more frequent "reversed" $\overline{v_{tan}}$ estimates.
- **vertical (or v_{tan}-perpendicular) effects not compensated for in WF**: The interaction between the lift - and drag force is responsible for accelerating the ski jumper is also a function of the angle of attack by the wind vector(*Jung et al.*,

2018, 2021a). The anemometers used in FIS competitions measure 3D wind and are able to estimate a v_{tan}-perpendicular wind component. The vertical wind component is typically for a higher v_{tan} magnitude, and changes in horizontal wind direction are also likely to affect it.

Unfortunately, points **a) - d)** have not been focused on in studies of data analytics, and point **e** is modeled and shown to change the jump length effect dramatically (*Jung et al.*, 2018), especially when wind speeds exceed 1 ms^{-1}. In spite of the fact that the aerodynamic effect of the vertical wind component has been shown to be influential on the jump length effect, this effect is not yet directly included in WF. However, this effect is likely indirectly included in the WF since it is based on both aerodynamic modeling and empirical statistics of ski jump performance influenced by a certain $\overline{v_{tan}}$. The main issue might be the fact that wind conditions where the vertical effect comes to play are likely to be very rare, and there is simply not enough performance data to catch this effect properly.

In order to improve fairness in ski jumping by revising the scheme computing the WF, it is natural to evaluate points **a) - e)** to classify them into "easy" and "difficult" issues to be resolved. Before the WF computation and the observation method used to provide its input can be revised, there has to be a study that justifies that the revised scheme is going to work better than the currently used one. The point about tardiness is rather easy to adjust for, by shrinking the period where $\overline{v_{tan}}$ is estimated. This might also require higher-frequency measurements such that the temporal mean has enough instantaneous data points.

The spatial error, which is what this thesis tries to make a QC/QA about, is somewhat difficult to deal with. More measurements and/or parameterization methods from turbulence statistics could be potential measures to improve the $\overline{v_{tan}}$ input. This is a shortcoming in the WF that (surprisingly) has not been studied yet. The measurement resolution error and the cross-wind effects are closely related, where an increase in cross-wind also is associated with an increase in the "requirement" of higher resolution on wind measurements.

By making the corridor length of $\overline{v_{tan}}$ small enough (and perhaps also a sidewind corridor), the non-linear effects due to the hill profile become negligible. With the requirement of wind corridor used today, non-linear effects are sufficiently small ($\leq 0.5 meter$) only if the inrun speed is set correctly. However, if the inrun speed is set to low, the expected jump length will decrease faster as a function of v_{tan} than the linear WF predicts. This means that the ski jumper is rewarded with too few compensation points, especially when v_{tan} has a negative anomaly. For HW the non-linear effects make the expected jump length increase slower as a function of HW tangential wind than the WF prediction.

Point **e** has studies justifying that the aerodynamic forcing leads to longer jumps when the competitor is affected by a positive vertical wind component (*Jung et al.*, 2018), but this is given the ski jumper maintains an ideal flight position as if he/she was prepared for the upward velocity component. The lift-to-drag ratio $\frac{F_l^2}{F_d}$ is ideal when the angle of

attack between skis and fluid flow is around 30° (*Virmavirta and Kivekäs*, 2019). This means that the ski jumper must adjust the skis to changes in the airflow direction. For positive changes in the vertical wind component, the lift is maintained, but drag is reduced due to a slight cross-section decrease due to the ideal flight position now being tilted towards the airflow.

Point **e** is also likely to be present in stable inversion conditions during the late afternoon where the stable air layer in the valley stops the downslope flow and forces it outwards giving the wind vector a larger horizontal component. This creates a positive anomaly in horizontal acceleration $\dot{v}_y$ and also a positive anomaly in the vertical acceleration $\dot{v}_z$ with constant v_{tan}.

Chapter 3

Campaign and Instrumentation

To investigate the wind conditions in a ski jumping hill, an observational campaign was conducted between October 12 and 26 at the ski flying hill of Vikersund in South-Eastern Norway. The campaign combined in a novel approach in-situ wind measurements by sonic anemometers across the jumping hill with wind LiDAR remote sensing. The reference position (59.93778° N, 10.01000° E) defines the vertical line (0, 0, Z) in Fig 3.2b.

3.1 Site Description

The slope profile (SP) of the ski-flying hill is located on the East side of a long valley with 600-700 m high mountains and a valley floor oriented North/South. The terrain in the vicinity of SP is illustrated in Fig 3.1a. The focus area consists of a steep easterly slope of more than 30° steep for the entire 10 km across, and the valley consists of forest, buildings, and water from Tyrifjorden.

The area of interest covers approximately 15000 m^2 in steep and complex terrain. The direction of the slope profile of VH is defined as the Y-direction in a righthanded Cartesian coordinate system. The Y-direction is close to the direction of the steepest mean topographic gradient of 34°. This mean gradient corresponds to an elevation difference of around 100 m for every 150 m horizontal distance. The area consists of a smooth ski-flying hill profile containing rocks and gravel, surrounded by vegetation (forest) and constructions/buildings in complex terrain as illustrated in the 3D satellite image from Google Earth in Fig 3.2a.

In this study, we apply a Cartesian coordinate system (X, Y, Z). This means that the wind components (u, v, w) are parallel to the (X, Y, Z) axis. The Y-direction defines the horizontal direction of the hill profile, with a positive direction upslope as indicated in Fig 3.1b, which also sketches a rotation of the XY plane by an angle of θ_r. This defines the new coordinates Y_r and Z_r. An along-slope rotation of the XY plane in the SA position is estimated by the mean slope of the wind vector in wind conditions with a small cross-component (u). This rotation is used for SAs measurements (and LiDAR measurements, which have a fixed component rotated 34.4°). In addition, SP defines another coordinate (non-linear), which is based on landing slope parameters given by

Weeger (2022). The model of the landing slope, which has a rather poor resolution, is interpolated in between the given YZ positions. The interpolation between two given positions (p_n, p_{n+1}) is a polynomial of the length away from p_n relative to the total length between p_n and p_{n+1}. The new coordinate y_p, which defines the slope profile, is represented as a parameter equation as the following

$$y_p(y,\, z) = \left\{ \begin{array}{l} y(k) = y_0 + \frac{L_n}{N} \cdot \sum_{i=0}^{k} \cos\left(\alpha_n - \left(\frac{i}{N}\right)^{c_n} (\alpha_n - \alpha_{n+1})\right) \\ z(k) = z_0 - \frac{L_n}{N} \cdot \sum_{i=0}^{k} \sin\left(\alpha_n - \left(\frac{i}{N}\right)^{c_n} (\alpha_n - \alpha_{n+1})\right) \end{array} \right\}$$

$$\begin{aligned} 0 \leq k \leq N \\ n &= 1, \quad 2, \quad 3\,, ..., \quad 11 \\ c_n &= 1.5,\ 1.2,\ 0.9,\ ...\ ,0.8 \end{aligned} \tag{3.1}$$

where the order of the polynomial is given by the coefficient c_n, and n is the partition between two given positions. The angle α_n is given by *Weeger* (2022), and c_n is a best-fit exponent for every given partition position and instantaneous growth.

A rotation of $\theta_{rl} = 34.4°$ is used in a QC/QA approach done on LiDAR measurements, which is done by comparing its output of the radial wind speed v_{rad} with the SAs computed component aligned with the LiDAR scan. Further information about the use of θ_{rl} can be found in 4.3. The new coordinates Y_r, y_p and y_{rl} are sketched in 3.2b, where the partitions used in the estimation of y_p are given by the vertical lines.

3.2 Setup for the Campaign in Vikersund, Norway

The observational setup consisted of three SA masts positioned upslope of a scanning LiDAR elevated such that the scan plane hits the Z-position of the three SA. A detailed description including the precise (X, Y, Z) position of the instruments is shown in Fig 3.2a & b.

The Y position of the three sonic anemometers was planned to be fixed at 66 m jump length along the slope profile. This was not possible, and the final positions of S1, S2, S3, and LiDAR were as shown in Table 3.1.

Table 3.1: 3D position for instruments defined from the origin at 59.93778° N, 10.01000° at the height of the out-run. XYZ-coordinates are describing the vertical displacement from the origin (Z) and horizontal (XY) displacement

Instrument	Y-position [m]	X-position [m]	Z-position [m]
S1	151.4	-40.5	112.7
S2	149.6	-30.9	113.7
S3	152.1	-19.5	112.4
WC100s	302.7	-31.0	9.7

The three SA and the WC100s LiDAR operated from these positions for 14 days in the period from Oct 12 to Oct 19, and from Oct 20 to Oct 26.

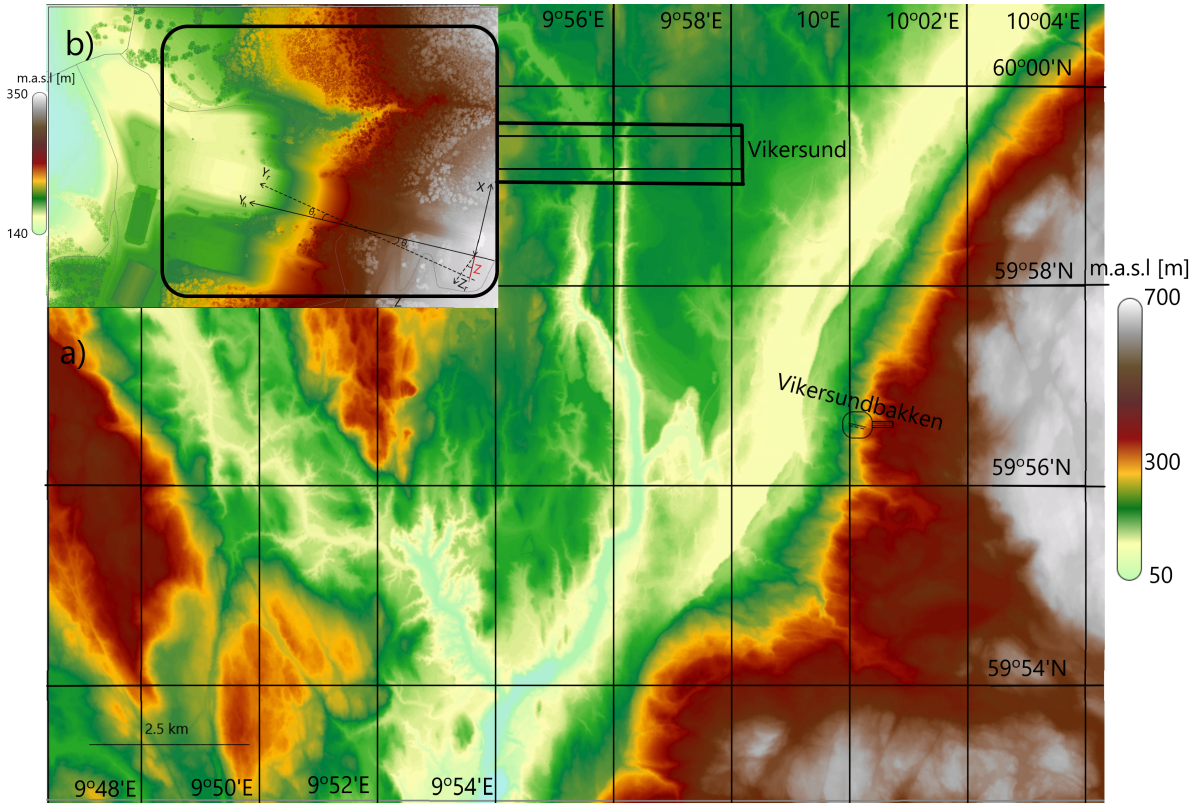

Figure 3.1: Overview of site area and applied Coordinate System. ***a:*** *Elevation and terrain of the valley around the investigated slope by Digital Terrain Model by Kartverket licensed under CC BY 4.0.* ***b:*** *Cite area (15000 m^2). Axes used to describe the cite are drawn in a right-handed 3D Cartesian coordinate system (X, Y, Z). θ_r is a rotation angle defining the along-slope axes Y_r and Z_r.*

Table 3.2: LiDAR Windcube 100S pitch/roll for the given date at 1300 UTC

date	pitch [°]	roll [°]
13^{th} *Oct*. 2021	0.016	0.016
14^{th} *Oct*. 2021	0.016	0.016
15^{th} *Oct*. 2021	0.023	0.014
16^{th} *Oct*. 2021	0.010 to 0.045	-0.009 to 0.035
17^{th} *Oct*. 2021	0.016	0.016
26^{th} *Oct*. 2021	0.001	-0.002

3.3 Instrumentation

In this campaign, a set of instruments are used to obtain a detailed picture of the spatial and temporal variability of the flow in the ski flying hill in Vikersund, Norway. During the campaign, the following meteorological instruments were used.

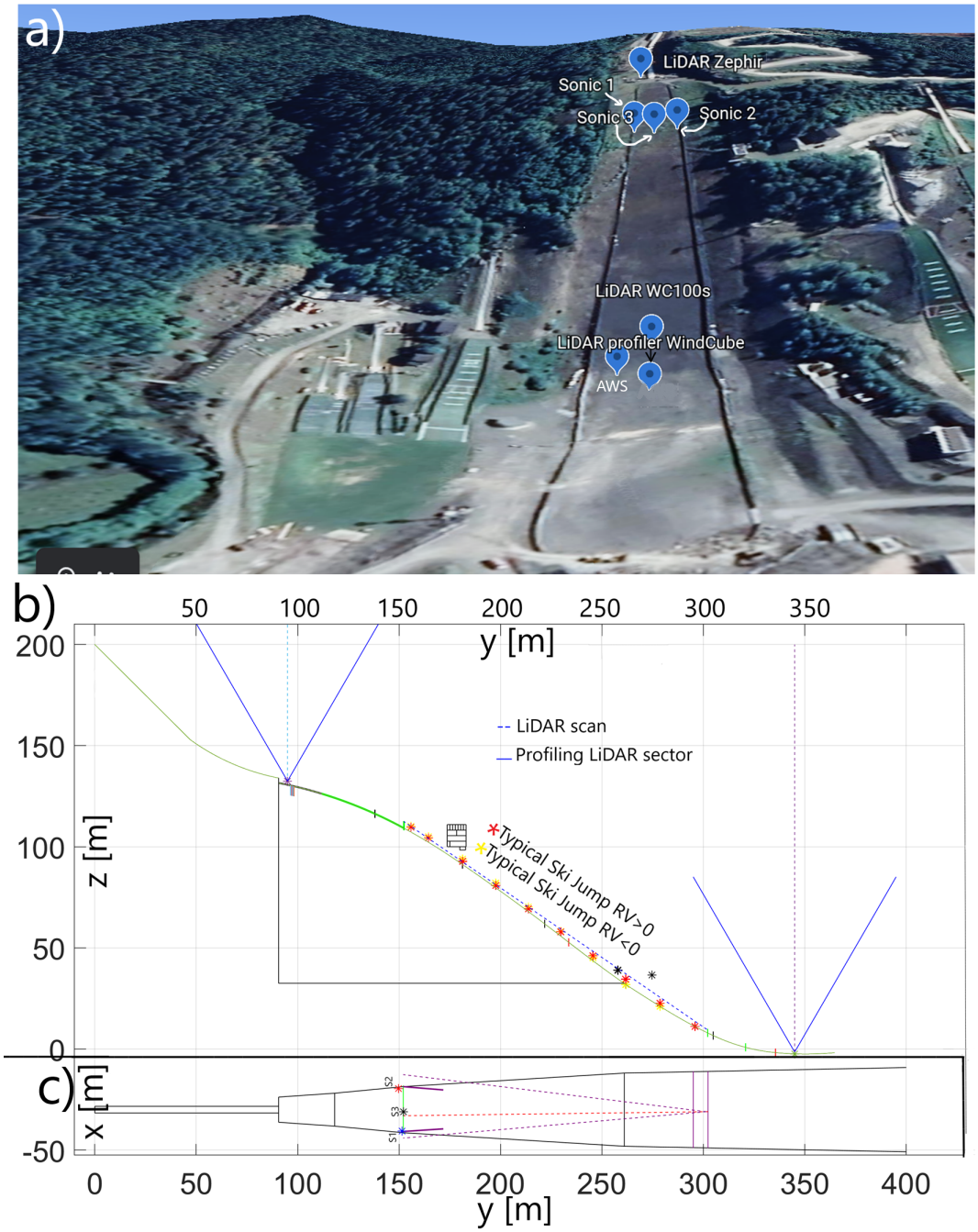

Figure 3.2: ***a:*** *Image of the Vikersund site with positions of the four instruments (Source: Google Earth).* ***b/c:*** *Sketch of Vikersund Ski-flying hill (VH) viewed from the side (b) and from above (c) modeled using parameters given in the FIS Certificate of Jumping Hill for VH (Weeger, 2022). YZ-plane ax defined by the LiDAR is illustrated in* ***b****, and the XY plane spanned by the ppi scan is defined by the area bounded by the two dashed (purple) lines in* ***c****.*

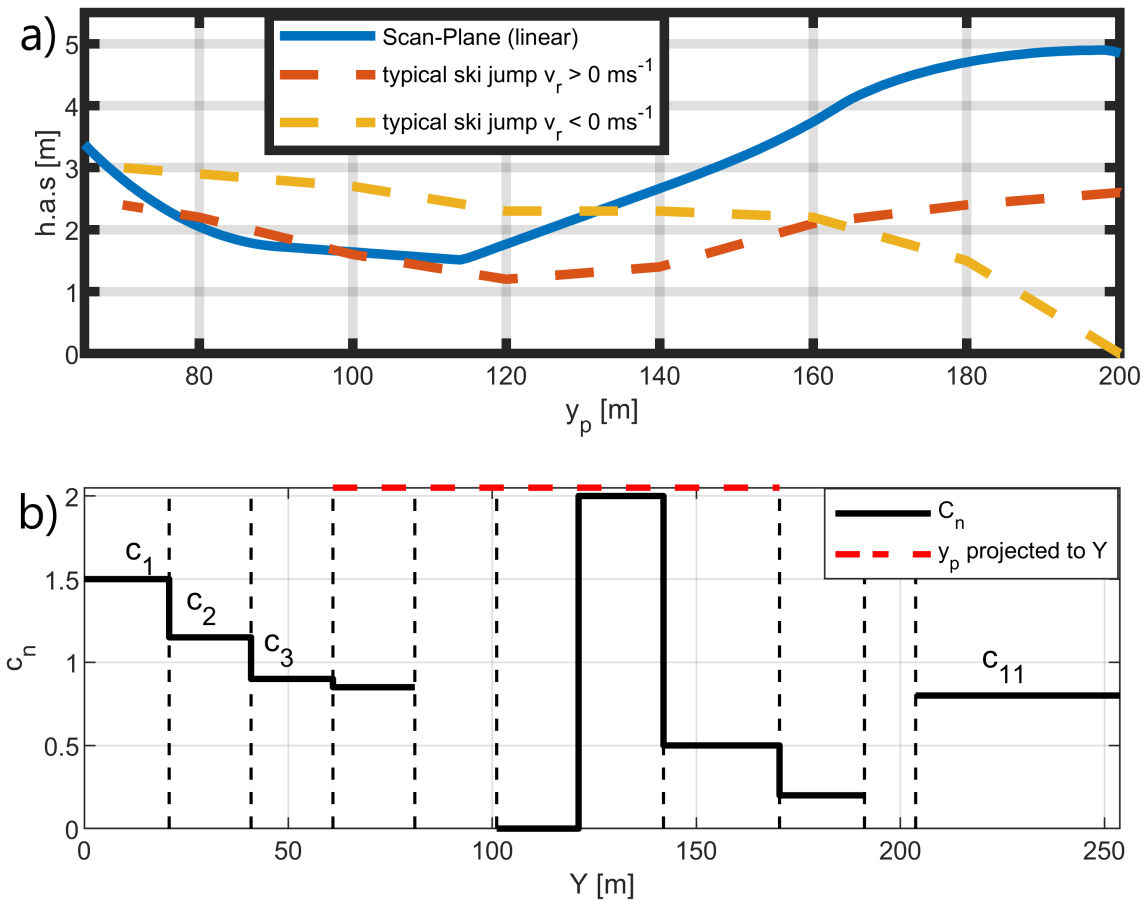

Figure 3.3: a: Scan plane height above the slope profile, y_p, as a function of jump length along the slope profile ax (y_p). This is plotted together with a typical ski jump trajectory in headwind/tailwind conditions. The position of the LiDAR would be at y_p = 247 (not shown in the plot). b: polynomial order used in slope profile as a function of Y position (or partition n). The gaps in n=5 and n=10 are there because of c_5 and c_{10} being so large.

3.3.1 Sonic Anemometer

Three Campbell CSAT3 3D Sonic Anemometers were used in the Campaign in Vikersund. The instrument is able to measure the 3D velocity from three pairs of transducers spaced by a radial distance d. It does so by using the time of flight for two pulses in opposite direction (*Campbell Scientific*, 2022). The relation between flight times and radial velocity of each pair of transducers is given by

$$t_o = \frac{d}{c + u_a} \quad t_b = \frac{d}{c - u_a}, \tag{3.2}$$

where t_o is the time of flight out and t_b is the time of flight the opposite way. The unknown, u_a, is the radial velocity along the transducer axis which can be solved using the two equations in 3.2 giving:

$$u_a = \frac{d}{2}\left(t_0^{-1} - t_b^{-1}\right) \tag{3.3}$$

Since the speed of the airflow along the transducer axis is known, the unknown speed of sound c can be found, since it is the only unknown in equation 3.2. The square

of c is proportional to $\frac{P}{\rho}$, which again are proportional to the virtual temperature:

$$(\gamma_m(q))^{-1}c^2 = \frac{P}{\rho} = R_d T_v = R_d T(1+0.61q) \tag{3.4}$$

where γ_m=$\frac{c_{pw}}{c_{vw}}$ and c is the speed of sound. Note that γ is a function of specific humidity. γ is translated to a factor containing q multiplied by the constant specific heat for dry air C_{vd}. The low dependency of q in this relation allows us to neglect this term, and we end up with:

$$T_s = \frac{c^2}{\gamma_d R_d}\ [K] \quad , \quad c^2 = \frac{d^2}{4}(t_0^{-1}+t_b^{-1})^2 \tag{3.5}$$

The transducers are tilted 30 ° horizontally which corresponds to $\Delta z = 10.0$ cm and Δxy = 5.8 cm. The coordinate transformation to a Cartesian, instrument-fixed system is done internally. A detailed description of the instrument can be found in Fig 3.4a.

Table 3.3: Outputs of SA and their limitations. Note (*): These errors only apply for azimuth angles $> \pm 10°$ away from the axis shadowing the SA sensors

Outputs	u_{xy}	u_z	WD_a	T_a
sample frequency	20 Hz	20 Hz	20 Hz	20 Hz
resolution	.001 $m\ s^{-1}$ rms	.0005 $m\ s^{-1}$ rms	0.06° rms	0.025 $°C$
range	$\pm 30\ m\ s^{-1}$	$\pm 8\ m\ s^{-1}$	0-360°	-30 to 50 $°C$
offset error*	$< \pm .08\ m\ s^{-1}$	$< \pm .08\ m\ s^{-1}$		
gain error*	$< \pm 6\%$	$< \pm 6\%$	$\pm 0.7°$	

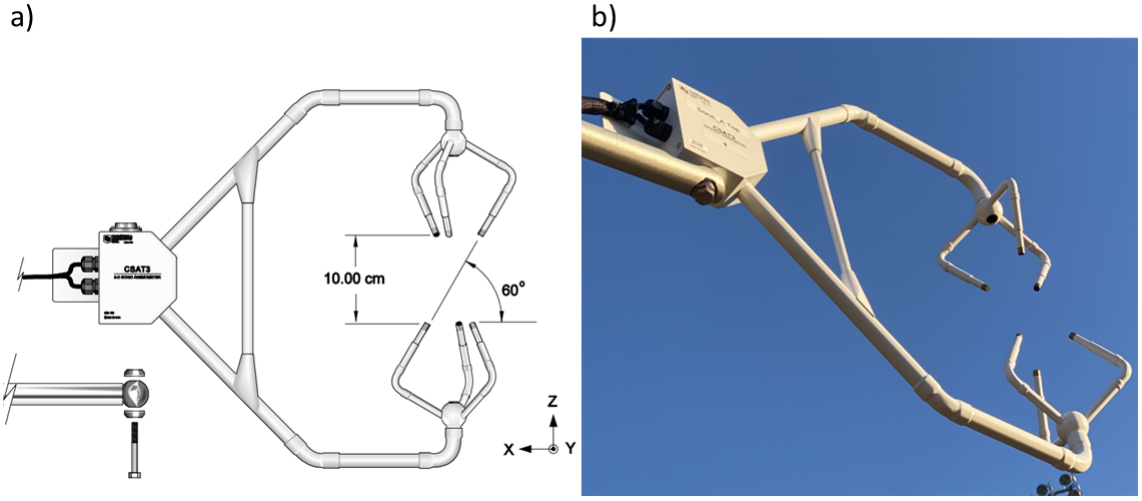

Figure 3.4: (a):Sketch of SA from Campbell of type CSAT3. (b):S1 on its operating position in Vikersund Ski Flying Hill.

3.3.2 Scanning LiDAR

A pulsed Doppler wind LiDAR from Leosphere (Wind Cube 100s) is used in the Vikersund Campaign. The instrument emits 10 thousand laser beams a second with a given

energy (250 mJ) and frequency spectrum (*Kavaya et al.*, 2014). The emitted signal is backscattered and received by LiDAR, and the mean frequency shift (Doppler shift) is related to the mean line of sight particle velocity, also called radial wind speed (RV). The amount of measured energy reflected back to the LiDAR sensor is related to the carrier-to-noise ratio (CNR), which can be used as a measure of the quality of the RV data. The phase shift of the frequency spectrum of the reflected signal is related to the relative motion of the scattering medium and the LiDAR sensor (Doppler effect). The LiDAR is able to create a picture of the airflow in a "continuous" 2D plane by scanning several azimuth directions and fixed elevation (ppi), or in several elevation angles with fixed azimuth (rhi). Specifications connected to the instrument are displayed in Table 3.4.

The scanning LiDAR on its operating position around $y_p = 245$ m is shown in 3.5

Figure 3.5: left: Scanning LiDAR of type WindCube 100s from Leosphere (WC100s) in its operating position in the slope of the ski jump hill. right: Sonic anemometer S3 seen from the position of the WC100s. Note that the scan plane hits at the S3 sensor height in the default PPI scan

3.4 Scan Schedule for WC100s

The first thing to emphasize is the motivation of this study. The small-scale wind structure in a ski-flying hill could have large differences depending on the upwind topography. Therefore, the best spatial resolution is required. When deciding the scanning plan, the focus is to catch the radial wind speed on different along-slope positions as a function of the across-slope position. The scan area of interest is inside a sector spanned by the LiDAR and the two boundary SAs. Therefore, the scan sector ended

Table 3.4: LiDAR WC100s: Specifications

Wavelength	1.55 μm
Dimensions	0.8 m $\times$1.0 m $\times$1.2 m
Weight	230 kg
Emitted power	2.5 W
Pulse rate	10 kHz
Measurement distance	50 m to 6000 m
Range resolution	25 m
Measurement range	-30 ms^{-1} to 30 ms^{-1}

up only 14° wide, which is covering all X-coordinates inside the hill for Y-positions between 150-170 m in 3.2b.

The schedule of the LiDAR scan was set to a loop of 40 scans of type Plan Position Indicator (PPI) and **one** scan of type Range Height Indicator (RHI). The PPI scans are set to a probe length of 25 m, starting from 50 m. The range gates are spaced by increments of 1 m and the integration time of 0.5 sec which in combination with the scan rate of $1^\circ\ sec^{-1}$ results in an azimuthal resolution of 0.5°. The computation of the 25 increments per range gate requires 25 times more data storage per unit scan range, resulting in a maximum range of only around 300 meters. The interest area of the radial wind speed is only from 50 m to 185 m distance from the LiDAR.

The main PPI scan was set to an elevation of 34.43°, corresponding to the intersection elevation with the three SAs. The azimuth angle (Φ_a) ranged $-5^o\circ < \Phi_a < 7^\circ$ with a scan speed of $1\ ^\circ\ s^{-1}$ and azimuthal resolution of 0.5° (x-resolution). This sector is just wide enough to intersect with the position of all three SAs, and the XY plane it spans is illustrated in 3.2c. This gives an increment area $1 \times 0.5\ m\ ^\circ$ which corresponds to approximately 1 m^2 at the SA positions. The resolution of the increments, however, is likely lower than 1 m, where the true resolution is unknown due to uncertainties in the range weighting function.

To capture the boundary layer height, cloud base height, or the along-slope synoptic scale wind speed, the LiDAR was also set to do an RHI scan. This was set to 1 scan every 10 min, with the azimuth of 0° aligned with the ski jumping slope. Its elevation angle θ_v was set in the range of $35\circ < \theta_v < 75\circ$ with scan speed of $\frac{2}{3}\ ^\circ\ s^{-1}$ and resolution of 3°.

Additional PPI scans of different elevations were tested in the period from Oct 12 to Oct 17, where one scan was lower (34.1°), and the other was higher (35.0°). Wind data from all the PPI test scans were insufficient with very low CNR-values. The chosen elevation was supposed to give wind data from positions comparable to a typical ski flyer trajectory, where a visual imagination of the scan plane can be seen in 3.5. The main PPI scan was set to 34.54°, hitting the SA position close to the SA height and having a height comparable to a typical ski-flyers' path down to jump length 140 m, which is illustrated in 3.3. The scan plane makes a linear trajectory from the position of the SAs and all the way down to 200 m jump length. The expected trajectory of a ski flyer differs in different wind conditions. However, independent of the wind conditions, the trajectory of a ski flyer is typically less steep than 34.54° close to the SA positions. Further down, at some point, the ski jumper has to have a steeper path. If

not, the maximum height will be reached above the K-point and exceed 5 m above the surface as the scan plane curve shows in 3.3.

In addition, manual checks of the pitch and roll were done to estimate possible sources of random errors in the elevation plane for seven days at 1300 UTC. The pitch and roll were relatively stationary throughout the campaign period as indicated in 3.2. On Oct 16, there were some small deviations around the mean pitch angle (approximately 0.020°) which could be related to high v_r this day (see 5.1 b).

3.5 Data availability

The data availability from the SAs and the WC100s is shown in Fig 3.6b. The Sonic Anemometers were available for the entire period between 12 and 26 October, except for one gap between 0000 UTC Oct 19 and 1630 UTC Oct 20. Data loss is likely related to snowfall in the nighttime of Oct 19 and maybe some accumulation of water on the transducer path. The data quality during this entire period is simply too poor to make it usable.

Another measure of the data quality can be defined in terms of the number of spikes detected in the evaluated time window. This QC method is done in 4.1.2, and the data points defined as spikes are simply removed from the data set. In Fig 3.6b, the time series of the number of detected spikes for S1, S2, and S3 is lower than 40 for every 10 min window, which means 99.7 % of the data did not define as spikes.

The WC100s data used in this study was decided given the requirements suggested in 4.1.2. The data availability from the LiDAR was considered of sufficient quality as shown in Fig 3.6 a, shaded as time series of CNR as a function of jump length position. Except for the two periods used in the instrument comparison done in 4.3, periods of sufficient LiDAR data was barely ever overlapping with the sufficient SA data. This comparison indicated that LiDAR data in this period was of good quality, and this also strengthen the reliability of the LiDAR data in the non-overlapping period between 0000 UTC Oct 19 and 1630 UTC Oct 20.

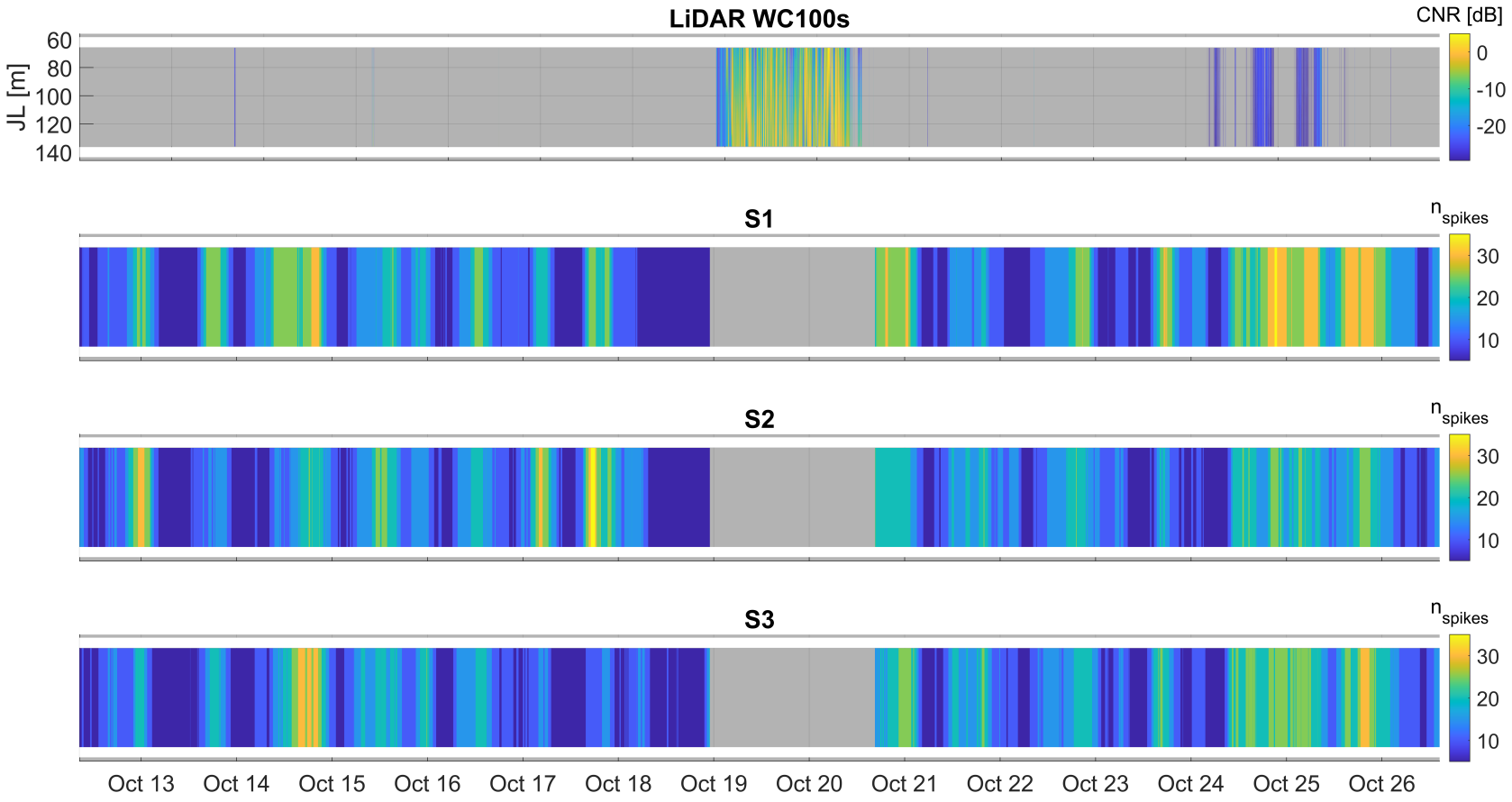

*Figure 3.6: data availability for LiDAR WC100s (**a**), and S1, S2 and S3 (**b**). Shaded regions are defined as time periods with good data availability. The shading in **a** also provides time series of CNR as a function of jump length position (JL) in VH. The shading in **b** indicates the time series of the number of spikes detected in a 10-min window.*

Chapter 4

Methods

4.1 Data Processing

This section contains a description of the data analysis methods in this study. The main goal is to provide statistical analysis of a reference wind ($\mathbf{u}_{ref}$) together with the observed wind in the center of VH by SAs. The variable $\mathbf{u}_{ref}$ is typically estimated with measurements from the X-boundaries of the hill. We conduct a statistical analysis of wind and its variance in categories/classes of horizontal wind direction and speed. The purpose of this class division is that the horizontal wind direction (hereinafter, θ_a) of the mean wind and its magnitude could have a significant influence on the transient behavior of v_r. The resulting statistics of 3D wind measurements by SAs in positions S1, S2, and S3, in between S1 and S2. More information about statistical parameters used in this thesis can be found in 2.

4.1.1 Averaging

To analyze the wind statistics, different means (i.e. spatial and temporal means) and the associated standard deviations are calculated. Mean wind data collected from the three SAs are expected to diverge from the horizontal plane, because of the steep terrain. For the SA data, temporal means of 10 s, 10 min, and 3 h are used. The full 20 Hz data is also plotted to illustrate the total range of turbulent fluctuations in the time series. The 3-hour mean is used to catch the low frequent background u, v, w, T_s. This is represented as a moving mean from the *smoothdata.m* function in MATLAB. In addition, a 1 s temporal mean is used for the comparison of SAs with LiDAR, described in detail in 4.3.1.

A linearly estimated S3 position variable (S_{ref}, or reference) is calculated taking the "spatial" mean between S1 and S2. When using the 10 s temporal means,

S_{ref} should be an appropriate recreation of $\overline{v_{tan}}$ used to calculate the WF used in FIS competitions. Similarly, a reference v_r (Li_{ref}) can be estimated from the LiDAR by using three spatial means around the SAs to reproduce the positions S1, S2 and S3. Details about how this is done are presented in 4.3.3.

The scanning LiDAR's line-of-sight is rather well aligned with the slope, so measurements of v_r by this instrument provide a good estimate of the along-slope flow. Together with the raw scan data, it is used 10 min temporal mean (corresponding to 45 scans).

This is to catch the lower frequent spatial distribution of v_r, which can be used to find out positions where v_r can be expected to deviate significantly from the reference.

4.1.2 Quality Control and Quality Assurance (QC/QA)

Some QC methods are done in order to capture potential malfunctions in the raw data from SAs and LiDAR. The quality of the SA data was tested by spike detection using the MATLAB function *gfispikes.m*. This was done with the method Mean Absolute Deviation (MAD)(*Mauder et al.*, 2013), a threshold of 3 median deviations, and a window of 10 minutes (12000 data points). The detected spikes are removed from the time series by replacing the data points with "NaN". In addition, the period from 0000 UTC Oct 19 to 1630 UTC Oct 20 is replaced by "NaN" based on a visual evaluation of u, v, w, and T_s in this time period.

Sufficient data from the WC100s is defined for scans where all the three Y-positions, represented as a spatial mean, measured a spatial mean Carrier to Noise Ratio (CNR) > -28 dB for $152 < Y < 172$ in Fig. 3.2a. It is also required that none of the individual increments in this region < -32 dB. The scans falling outside of this required CNR for sufficient data are also considered precipitation free. In addition, the quality of the WC100s measurements is tested by comparing the time series of the SA position WC100s data and 1-sec mean SA data for the synchronized period. QC/QA done with the LiDAR data is also based on comparison with SA data as described in 4.3.1. This analysis found a linear regression line with a slope of 0.9, which is considered as a bias in the LiDAR data due to its larger measurement volume.

4.1.3 Statistical Analysis from World Championships in Vikersund

In addition to the data sampled from the campaign, this study includes statistical analysis based on the World Championship results in Vikersund in March 2021. This statistical analysis is based on the mean weighted $\overline{v_{tan}}$-data. This weighted wind is compared with the competitors' achievements in jump length. This analysis consists of 6 competition rounds in the period from 11 th of March until 14 th of March 2022. The wind data is represented as a 5-second mean from 10 anemometers operated by FIS, where the averaging period starts 3 seconds prior to the ski flyer passing the first anemometer position (*Czarnecki*, 2020). The instrument data is collected by FIS during the competitions. In this competition, the gate position was changed at least once in rounds 3 to 6. This is accounted for in the total score, giving -7.4 points per gate in gate compensation. Instead of point compensation, the jump length is adjusted corresponding to units of jump length gate compensation translates to. This analysis can be seen in Fig. A.3 in A.4. The wind data is sampled by 10 SAs positioned at Y-positions corresponding to 10 %, 40 %, 60 %, 80 %, and 100 % of the K-point at 200 meters (*Virmavirta and Kivekäs*, 2012c), and have an output of u,v, and w with a sampling frequency of 4 Hz according to the wind data used in World Championship in Vikersund in March 2021. Data are confidential, and received by Swiss Timing.

4.1.4 Coordinate Rotation

In order to analyze the wind vector between S1, S2, and S3, it is important to have the instruments aligned parallel to the mean streamlines in the investigated area. Because of high inclination and complex terrain with inhomogeneous surface roughness in the vicinity, the wind vector becomes very unpredictable. In addition, random or statistical uncertainties are introduced when the instruments are mis-aligned relative to each other. This uncertainty could be in the order of 10° since the orientation was roughly (without using a compass) such that the v-component became along-slope. One method to fix this uncertainty is to search for a relatively long period of relatively weak variation in horizontal wind direction. To point out an appropriate period to use for defining a reference coordinate system, we search for a period where the standard deviation of the mean 10-minute azimuthal wind direction is less than $\sigma_a = 20^\circ$. This is calculated using the Yamartino methodology (*Turner*, 1986), using the difference between variances of the trigonometric periodic functions of the angle, and the mean trigonometric value squared. More details about angular statistics can be found in 2. The time series of the 10-min mean of σ_a is shown in Fig. 5.2 in 5. By assuming that the flow is parallel in this period and that it has a similar azimuth direction on S1, S2, and S3, we can set this direction as the orientation of the hill (0°). Thereafter we rotate the xy plane spanned by the S1, S2, and S3 orientations such that the mean u-component is zero. The new u component, which is calculated for a period of stable HW conditions from 0900 to 1700 UTC on Oct 15, becomes

$$\begin{aligned} \overline{\theta_1} &= 7.3^\circ \\ \overline{\theta_3} &= -3.4^\circ \\ \overline{\theta_2} &= 3.8^\circ \end{aligned}$$

$$u_n = \pm|\mathbf{U}_{xy}| \cdot sin\left(sin^{-1}\left(\frac{\overline{u_n}}{\pm|\mathbf{U}_{xy}|}\right) - \theta_n\right), \quad n = 1,2,3 \qquad , \quad (4.1)$$

where θ_n is the azimuth deviation for sonic n. Sign of $\pm|\mathbf{U}_{xy}|$ is determined by which quadrant the instantaneous wind vector belongs to because $sin^{-1}\theta$ only is defined for $-90^\circ \leq \theta \leq 90^\circ$.

We find the corrected v-component by simply using the Pythagorean theorem and choose the sign of the new v by the sign of the corrected u and w, and the original sign of v (from the RAW data coordinate plane).

To get a better understanding of how mean and fluctuating flow behave on a steep hill, we use a coordinate system rotated along the hill. The y-axis is now aligned with the center line of the landing area, and the z-axis is perpendicular to a terrain-following plane (x-y-plane). In the y-position of the center Sonic Anemometer, the slope is approximately 26-28°. The slope of the mean flow was used to create a fitting coordinate system.

The angle of 28.1 ° presented as $\overline{\theta_{hw}}$ in 4.2 defines the terrain following and stationary

plane used in this study and is used in 4.3 for the axis rotation on the SAs. This angle is calculated in the same stable HW conditions as used in the xy plane rotation. We define a new w-component not parallel to the gravity vector, but rather an anomaly in the topography perpendicular component.

The other angle, 26.1°, was found in a 10-hour TW period starting from Oct 12 at 1600 UTC. Only the mean wind vector in the HW period is used in the stationary rotation, mainly because the anomaly in the new w-component for TW conditions is an important aerodynamic effect which is described more in 4.2. The new w component can be calculated from the raw data v, w (assuming v - direction is parallel to the hill)

$$\begin{aligned} \overline{\theta_{hw}} &= \overline{tan^{-1}\left(\frac{\overline{w}}{\overline{v}}\right)_{hw}} = 28.11^\circ \\ \overline{\theta_{tw}} &= \overline{-tan^{-1}\left(\frac{\overline{w}}{\overline{v}}\right)_{tw}} = -26.07^\circ \end{aligned} \quad , \tag{4.2}$$

where $\overline{\theta_{hw}}$ and $\overline{\theta_{tw}}$ are given by mean tilt in the position of S3 during the periods mentioned above. By rotating the yz-plane, the new w component becomes

$$\begin{aligned} w_{hw} = w_r &= |\mathbf{U}_{yz}| \cdot sin\left(\theta_v - \overline{\theta_{hw}}\right) \quad \text{for v} > 0 \\ w_{tw} &= |\mathbf{U}_{yz}| \cdot sin\left(-\theta_v - \overline{\theta_{tw}}\right) \quad \text{for v} < 0 \end{aligned}$$

$$\theta_v = sin^{-1}\left(\frac{w}{|\mathbf{U}_{yz}|}\right), \tag{4.3}$$

where w_{hw} and w_{tw} are the rotated w-components perpendicular to the rotated terrain following xy plane for HW and TW conditions, respectively. θ_v is the tilt of the wind vector spanned from the non-rotated xy plane. The component w_{tw} is only looked at as an anomaly component given TW conditions and is not used in the coordinate rotation.

4.2 Tangential Wind Speed Function (F_1)

In order to evaluate the fairness connected to the WF compensation system from FIS, there are some aspects to analyze. The system used in the FIS competition is based on a linear model only taking two boundary tangential wind measurements similar to the reference in this thesis as explained in detail in 2.4.4. The lack of information on the tangential wind in the center of the hill during competitions, and also the unstudied tilt effects from the wind vector due to anomalies in the slope perpendicular w-component, can in some situations be fatal for a competitor. In other words, the linear estimation of the true wind conditions might on some occasions deviate from the true wind, and several competitors have experienced that the competition score often contradicts how the wind conditions felt (*Czarnecki*, 2020). To investigate these two shortcomings in the computation of the WF, this study proposes to use a function (F_1) to capture the difference between $\overline{v_{tan}^{ref}}$, v_{tan}^{diff}. Another term in F_1 is supposed to compensate for a tilt effect

(v_{θ_v}). v_{θ_v} approximates the JL effect of the tilt of the wind vector from the perspective of a ski jumper θ_W and represents the JL effect with the $\overline{v_{tan}}$ it is corresponding to. The value from F_1 is a scalar output (ms^{-1}) as a sum the two terms mentioned above. The scalar represents the deviation between a replica of the FIS estimated $\overline{v_{tan}}$ by measurements of v_{tan}^{ref}, and observed $\overline{v_{tan}}$ by S3. F_1 is supposed to catch the periods of wind conditions deviating significantly from the FIS model estimation, according to available wind data collected for this study. The function includes the tangential wind speed difference (v_{tan}^{diff}) from F, and also effects from the tilt of the wind vector. To build this function, and especially the term including θ_v, we need to dig into prognostic equations of a ski jumper with a ground velocity v_s and a wind vector $\mathbf{u}$. F_1 output gives an indication on the influence from true aerodynamic forcing compared to the estimated one using $\overline{v_{tan}}$, where drag and lift are a function of angle of attack (AoA) (θ_v) and the true air speed of a ski jumper (W), as defined in 4.7. This study only uses a predefined ski jumper velocity of -30 ms^{-1} parallel to the xy plane tilted for HW conditions. In reality, the ski jumpers' velocity at the Y-position of the SAs is not fixed. It is also to some extent expected to be a function of θ_v because of the loss of drag connected to TW conditions.

The function F_1 assumes that the effects of density can be neglected as they are much smaller than the ones of v_{tan}^{diff} and θ_v. The only input for calculating the WFC factor is a reference tangential wind speed measured from two boundary X-positions on five different Y-positions as described in 2 as the average between two boundary positions. We create a function $F_1(v_{tan}^{diff}, \theta_{v3})$ estimating the error in the method using $F(\overline{v_{tan}})$ used by FIS. F_1 defines the difference between the "true" tangential wind v_3 and the reference wind v_{tan}^{ref}. In addition, an estimated WF contribution caused by θ_v is added to the function. The function has the following form

$$
\begin{aligned}
F_1(v_{tan}^{diff}, \theta_v) &= v_{tan}^{diff} + v_{\theta_v} \qquad \text{for v} > 0, \\
F_1(v_{tan}^{diff}, \theta_v) &= v_{tan}^{diff}(1 + 0.21\varepsilon_{i,j}) + v_{\theta_v} \qquad \text{for v} < 0, \\
v_{\theta_v} &= \chi \cdot \theta_W', \\
\theta_W &= \theta_W(\theta_v), \qquad (4.4)
\end{aligned}
$$

where χ is an unknown proportional factor for anomalies in θ_W (θ_W'). θ_W is the total angle of the wind vector relative to a ski jumper with velocity parallel to the HW-rotated xy plane in a predefined speed of 30 $m\ s^{-1}$, with an expected value of -28.1°. The unit tensor $\varepsilon_{i,j} = 1$ when F_1 is compared to the WF between the 2009/2010 - 2012/2013 season which did not include the 0.21 factor for TW conditions, and $\varepsilon_{i,j} = 0$ for the current WF (0.21 factor included). The unit tensor illustrates the 21 % positive anomaly connected to the (negative) JL effect for TW conditions due to the non-linear slope profile described in 1. The new variables introduced in 4.4 are defined as:

$$v_{tan}^{diff} = v_3 - v_{tan}^{ref}, \qquad v_{tan}^{ref} = \frac{v_1 + v_2}{2} \tag{4.5}$$

$$W = v_3 + v_s, \qquad v_s = (-30, 0) \tag{4.6}$$

$$\chi = \frac{d\,\dot{v}_y}{d\,\theta_W}\left(\frac{d\,\dot{v}_y}{d\,W}\right)^{-1} + \frac{d\,\dot{v}_z}{d\,\theta_W}\left(\frac{d\,\dot{v}_z}{d\,W}\right)^{-1} \tag{4.7}$$

(4.8)

The fraction χ is obtained from (*Jung et al.*, 2021a) calculating the derivatives of the accelerations with respect to θ_W and W from the given equation of motion

$$\dot{v}_y = -\frac{F_d cos\theta_W + F_l sin\theta_W}{m} \tag{4.9}$$

$$\dot{v}_z = -\frac{F_d sin\theta_W - F_l cos\theta_W}{m} - g \tag{4.10}$$

where F_d and F_l are the drag and lift force respectively. The lift and drag forces on a ski jumper in different v_{tan}^{diff} conditions and the effect of θ_W are illustrated in Fig. 4.1. By applying first-order Taylor approximation around $\theta_v = 28.11^\circ$ we can approximate the θ_W effect on the function for $\theta_v \neq 0$ to find the expression for χ. Drag and lift are both proportional to the square of W, and by assuming the area of the cross-section and the air density to be independent of W, the derivative of F_d and F_l with respect to W is $2W \cdot F_d$ and $2W \cdot F_l$. Thus, the derivative $\frac{d\ \dot{v}_{yz}}{d\ W}$ becomes

$$\frac{d\ \dot{v}_y}{d\ W} = 2W\dot{v}_y \tag{4.11}$$

$$\frac{d\ \dot{v}_z}{d\ W} = 2W(\dot{v}_z + g) \tag{4.12}$$

and $\frac{d\ \dot{v}_{yz}}{d\ \theta_W}$ becomes

$$\frac{d\ \dot{v}_y}{d\ \theta_W} = -\frac{F_l cos\theta_W - F_d sin\theta_W}{m} \tag{4.13}$$

$$\frac{d\ \dot{v}_z}{d\ \theta_W} = -\frac{F_l sin\theta_W + F_d cos\theta_W}{m} \tag{4.14}$$

resulting in χ as the fraction between the right-hand side (RHS) of 4.13 and 4.11 added with the fraction between RHS of 4.14 and 4.12. By substituting $F_d = \rho/2W^2 \cdot D$ and $F_l = \rho/2W^2 \cdot L$ we get the second term in 4.4

$$\chi \cdot \theta'_W = \frac{1}{2} \cdot W \left(\frac{Dcos\theta_W + Lsin\theta_W}{Dsin\theta_W - Lcos\theta_W} + \frac{Lcos\theta_W - Dsin\theta_W}{Lsin\theta_W + Dcos\theta_W} \right) \theta'_W, \tag{4.15}$$

where D and L are the drag and lift areas for a ski jumper. In this thesis, the areas are set to a constant value $D = A \cdot c_D = 0.59 \cdot 0.75m^2$ and $L = 0.90 \cdot 0.75m^2$ which corresponds to a fixed AoA between 28 to 30° from (*Virmavirta and Kivekäs*, 2019). This AoA is giving an optimal lift-to-drag ratio $L^2/D \approx 1.37$ given the optimal form of 15° yaw angle and 10° edge angle as explained in Fig. 4.2. F_1 uses v_{tan}^{diff} as a reference and adds on the v_{tan}^{diff}-equivalent θ_W effect in a fixed angle of attack (AoA).

4.3 Comparison of Wind Measurements from Sonic Anemometer and LiDAR WC100s

This section will contain an explanation of different methods applied in this study in order to make a QC/QA of the LiDAR measurements by comparing it to SAs measurements. The purpose of making this QC/QA on the LiDAR is that LiDAR data of radial

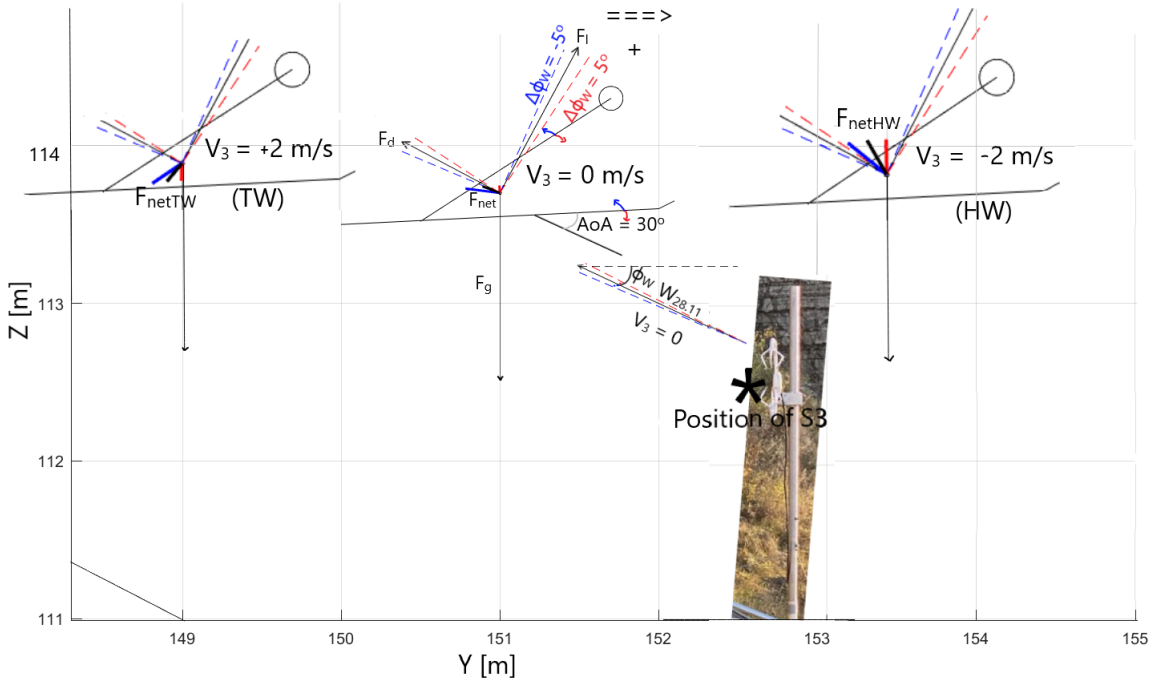

Figure 4.1: 2D forcing (YZ) on a ski jumper with optimal form and constant AoA = 30° having an along-slope speed of 30 ms^{-1}. θ_W-effects by wind conditions rotating $\theta_W \pm 5°$ from reference $\theta_W = 28.11°$ is presented in dashed and coloured lines. F_{net} is the net acceleration where the colouring represent the different θ_W conditions.

wind speed (v_r) might answer RQ(1) in 1 about finding deviations between $\overline{v_{tan}}$ and v_{tan} in other Y-positions that the SAs. By comparing the output of v_r from LiDAR in the position of the SAs with calculated v_r by the SAs, we can provide a measure of the predicted true v_r and its uncertainty. The chosen data points to compare are two periods with sufficient LiDAR and SA data between Oct 24 and Oct 25, with time series of 10-min mean v_r shown in Fig. 4.4b. Sufficient data quality for WC100s, S1, S2, and S3 are defined in 3.6. This comparison is based on the 1-sec temporal average of measurements by SA together with a spatial average of six $1m \times 0.5°$ increments around the SA positions as shown in Fig. 4.3. The method used to make this comparison is explained in detail in the following three subsections.

4.3.1 Radial Velocity from SAs

To be able to compare wind measurements by SA and LiDAR, the first thing to note is the 1D output by WC100s might not be aligned with any of the SA components. Therefore, it is crucial to define an expected solid angle from each individual SA to the LiDAR. The expected YZ-plane is 34.4° since the SAs are leveled to the gravity plane (0.0°) and LiDAR scan is elevated to fit its scan-plane at the elevation of the SAs as illustrated in 3.2 b. The azimuthal wind component for all three SAs in the WC100s line of sight direction is calculated assuming all SAs are leveled and oriented sufficiently close to perpendicular to the LiDAR horizontally after a rotation of the u - component done in Section 4.1. However, the line of sight direction for positions S1, S2, and S3 is not parallel, which also has to be taken to account when comparing the SAs to the

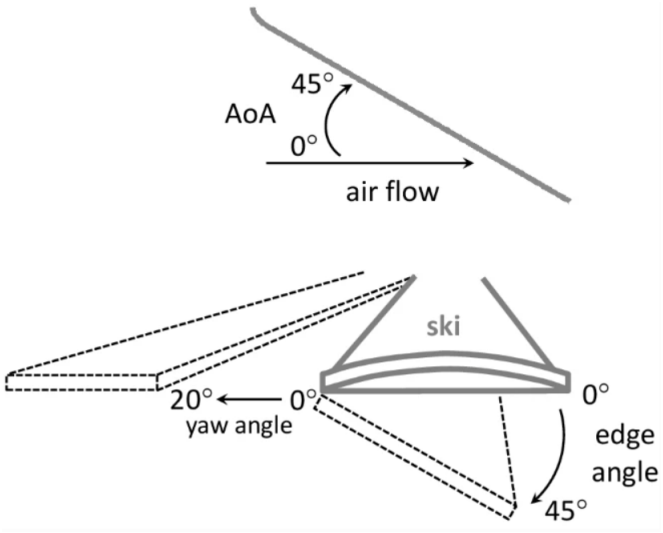

Figure 4.2: Form angles for ski jumper: Assumptions in F_1; AoA = 30°,yaw angle = 15°, edge angle = 10°. Sketch made by (Virmavirta and Kivekäs, 2019).

LiDAR. This is simply fixed by rotating the horizontal component of S1, S2, and S3 the angular position of the associated SA derived from CNR-maxima in Fig. 4.3.

4.3.2 Time Synchronization between LiDAR and SA Data

In order to compare in situ measurements of v_r by S3 with the scanning LiDAR it is essential to ensure that the time of the scan through the S3 position matches the time of the compared S3 measurement. We search for the time shift in which the correlation between the two measurements peaks. The highest linear correlation coefficient of 0.90 was found when comparing LiDAR scans with a (forward?) time shift of 59.5 ± 1.0 seconds on the SA system represented as a 1-second temporal mean. This time shift is used in the comparison analysis of LiDAR and SAs.

In addition, unphysical scan measurements by the LiDAR are removed by only allowing data points within the requirement of $-4\,ms^{-1} < v_r < 4\,ms^{-1}$, which is outside 3 standard deviations from the mean of the SA measurements in this period.

4.3.3 LiDAR Measurement Volume

To eliminate the random error introduced by the shadow region of the SA masts inside the measurement volume of the LiDAR, the LiDAR measurements are represented as spatial means of six increments surrounding the SA positions as illustrated with boxes in the CNR array in Fig. 4.3. The range gate with a probe length of 25 m are spaced with increments of 1 m radially, and an azimuthal resolution of 0.5° as stated in 3 The best representation of the location of the SAs in the LiDAR array is estimated as the three peaks in CNR in an arbitrary scan.

The comparison between the LiDAR and SAs indicated that LiDAR measurements were fairly good. Scatter plot and regression analysis are shown in Fig 4.4 a, and the resulting correlation coefficient (R) was close to 0.90 for all three sonic positions. However, the incline of the regression line indicated a 10 % underestimation of the

LiDAR wind, which is likely to be due to the measurement volume of the LiDAR which is more like upwind/downwind weighted spatial mean. Downwind of the SA position are relatively much closer to the surface, which probably slowed down radial wind speed here. The mean wind actually had the opposite effect, which can be seen in time series of the 10-min rm in Fig 4.4 b. The scatter of the rm confirmed this and had a regression line with 1.02 incline rate (not shown in figure).

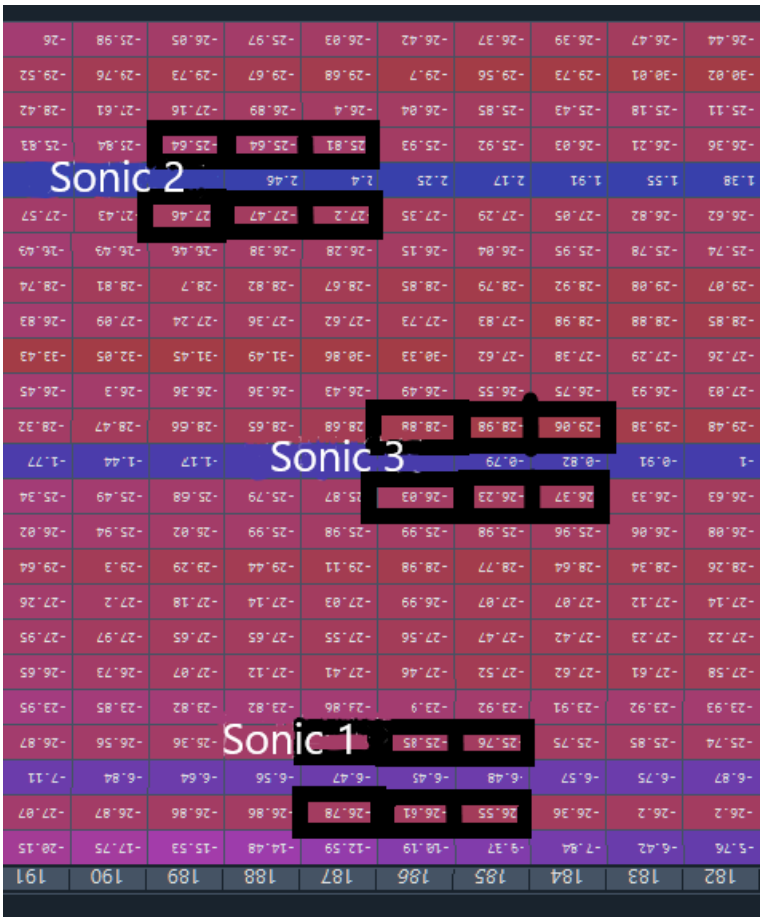

Figure 4.3: CNR - array in the area surrounding the SA positions. The position of the SAs is estimated in the center of the 6 black boxes.

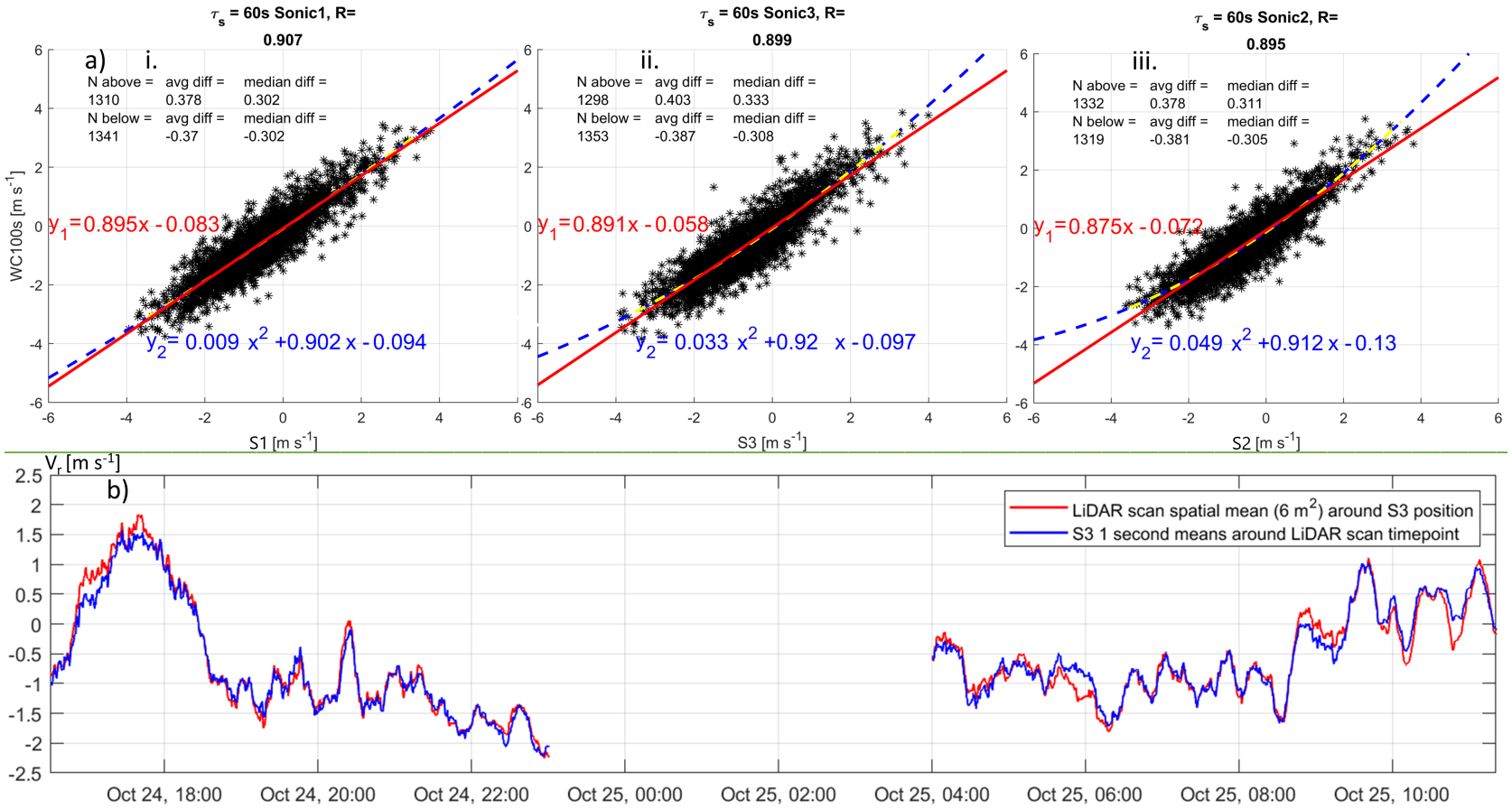

Figure 4.4: Comparison of LiDAR WC100s and SA measurements between Oct 24 at 1500 UTC and Oct 25 at 1120 UTC. a): Scatter of WC100s measurements as function of S1 (i), S2 (iii) and S3 (ii). The color of regression functions is associated with the color of the associated regression line. b): Time series of S3 and LiDAR WC100s during the associated comparison periods of the 10-min moving mean of v_r.

Chapter 5

Results

In the following sections, we present the spatial distribution of the wind component $\overline{v_{tan}}$ (or v_{ref}) in a linear plane above the surface of the Vikersund ski flying hill. This plane is defined by the position of three sonic anemometers (S1, S2, and S3), where the y-axis is aligned with the slope gradient of Vikersundbakken at the position of S3 (28.1°), and with an xz plane orientated such that it forms a righthanded Cartesian coordinate system (see Section 3.1). A scanning LiDAR, aligned with the mean slope gradient (34.4°), caught the $\overline{v_{tan}}$ further downslope, which also extended the observational plane in the y-direction. Time series of the three rotated velocity components (u_r, v_r, w_r) derived in Section 4.1 and T_s are plotted in Fig 5.1a, b, c, and d respectively. The observed data set allows for a detailed investigation of the wind conditions in complex topography. The main focus of this thesis, however, is on wind conditions within the wind corridor for ski jump competitions. This is defined in Section 4.1 as 10 s mean $\overline{v_{ref}}^{10s} < 2.5\ ms^{-1}$ with a standard deviation of $\sigma_{ref}^{10s} < 0.2\ ms^{-1}$.

Note that LiDAR data is only based on 10-min means or more, which does not capture the variability of the spatial distribution. However, the cross-sectional variability from the sonics is assumed to represent the approximate short-term variability in the LiDAR cross-sections. Especially for periods with $u_r < 0.5$ ms^{-1}.

5.1 Observed Meteorological Conditions

The 14-day period of the campaign in Vikersund was characterized by clear weather days and cloudy days, and only relatively few periods of precipitation. The observations of u_r, v_r $(or v_{tan})$, w_r, and T_s on the knoll in the slope profile (y_p=66 m) is shown in Fig 5.1. Temperature and precipitation data from a weather station on the valley floor (Geithus, Modum) is also shown. The 10-min mean horizontal wind direction (WD_a) and tilt relative to the $(xy)_r$-plane are shown in Fig 5.2a and b respectively. The overall weather conditions fit well with the expected synoptic/diurnal signal at this time of the year, which is explained by (K. Gislefoss, personal communication, Dec 2022):

The North/South-directed valley generates dominant wind directions along the valley floor, which is the case both when over bare ground and snow-covered surface. When cloudy (domination of synoptic scale signals), the North/South channeling normally gives a small mean wind speed (WS) above the hill slope, and the variability

(or above slope turbulence) typically correlates well with the synoptic scale WS. In the spring (around March/April) föhn wind is often present, when synoptic scale easterly winds from the mountains are forced towards the valley floor. This will, especially under cloud-free conditions (domination of diurnal signal), be replaced by HW condition and gusty conditions around 13 LT (or 11 UTC in Fig 5.1). The gusty conditions originate from the statically unstable heated air in the boundary layer above the valley floor being replaced by dense air with relatively high momentum from the mountains in the west-northwest. The gusty period in the daytime is slowly replaced with more calm conditions in the evening transition. After sunset, the HW conditions are replaced with a TW (v_r<0 ms_{-1}), accelerating towards the statically stabilizing valley floor due to the relatively rapid radiative cooling upslope of the Vikersund hill.

The diurnal effect described above is especially seen in the data from Oct 15, Oct 16, Oct 17, and Oct 21, which shows that rapid heating of the valley floor (Geithus) from 10 UTC to 12 UTC is connected to a rapid increase in mean v_r and its variability (see Fig 5.1b and d). Except for evenings on Oct 17-18, and around noon on Oct 13 (and full days on Oct 19 and Oct 20), WS was too high or conditions too gusty for competitions to be held. The horizontal wind direction (WD_a),shown in Fig 5.2a, was typically HW conditions close to 0° along-slope and more widely spread between 135° and 225° during TW conditions. The strongest wind speeds during TW are found for positive u_r component around 160° WD_a, as illustrated in Fig 5.3, which also seams to be typical for most of the periods with a strong negative v_r.

The 24-h periods with the clearest diurnal signal, turbulence was higher in the daytime, where the slope experienced consistent HW conditions ($v_r > 0$), associated with anabatic upslope flow. This time of the day was also associated with the highest wind speeds (WS), highest TKE content (standard deviations), and the highest T_s values. The highest wind speeds were measured between 12 UTC and 14 UTC local time on Oct 15, Oct 16, and Oct 21 shown in Fig 5.1 b, where the former two dates were clear weather days. As seen in Fig 5.1b, the two clear days mentioned above Oct 15 and Oct 16 were characterized by a large TKE content (large velocity fluctuations). Oct 15 and Oct 16 were also characterized by a strong diurnal forcing, with a maximum 3-h running mean close to 5 ms^{-1}, and a minimum $\sim$ -2 ms^{-1}. Higher frequent diurnal signals were present during some of the clear days, i.e a local maximum v_r around 1630 UTC, especially on the S1 position (not shown).

Around noon on Oct 13 was also relatively calm, but is rapidly replaced by gusty TW conditions at 14 UTC and advection of warm air from the East. This advection of warm air did not reach the valley floor in Geithus before sunrise on Oct 14, and at its most, the resulting inversion was more than 6°C. This made the nocturnal boundary layer beneath the altitude of the sonic measurements very stable, and the high turbulent wind conditions forced colder air while strong enough TW - gusts were present. This effect is more closely discussed in 5.3.3.

On Oct 14, which was one of the 6 days not having consistent HW conditions, the wind varied between a positive and negative v_r, but the afternoon maximum peak of v_r was still present. However, HW conditions are captured around midnight. The change in v_r, $\frac{dv_r}{dt}$, was positive a few hours before midnight and changed sign afterward. The sign change of $\frac{dv}{dt}$ around midnight was followed by a higher rate of T_s decrease.

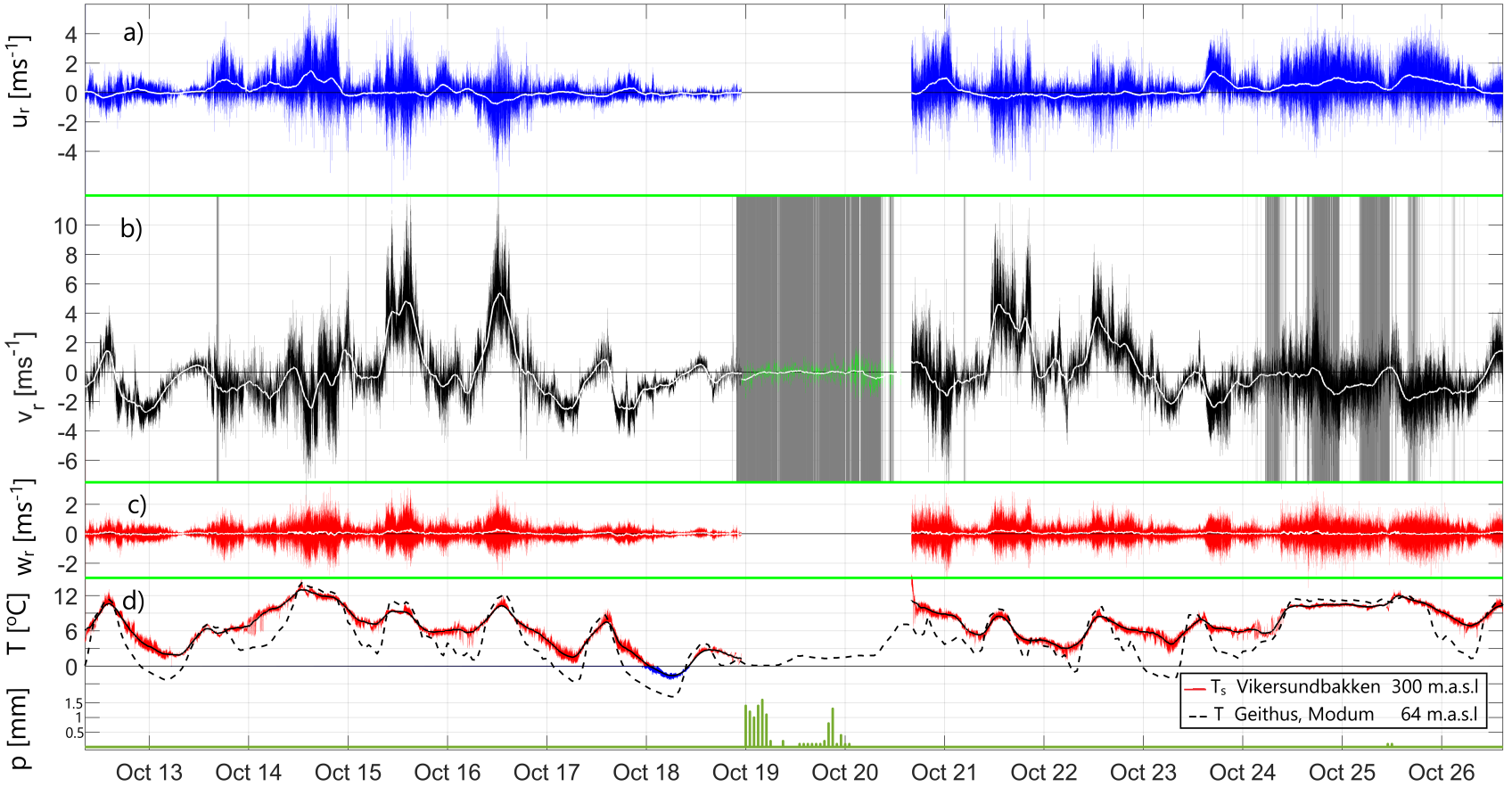

Figure 5.1: Time series of atmospheric variables in boxes a, b, c and d which corresponds to the variables u_r, v_r, w_r, and T_s respectively. For the boxes a, b, and d, the lower frequent line represents a 3-h running mean (rm), which for c corresponds to a 10-min rm. Gray shading in b represents time periods where variable v_r from LiDAR was sufficient. The dashed line in d represents observed T in the official national weather station in Geithus, Modum every 1-h (green bars - 1-h precipitation).

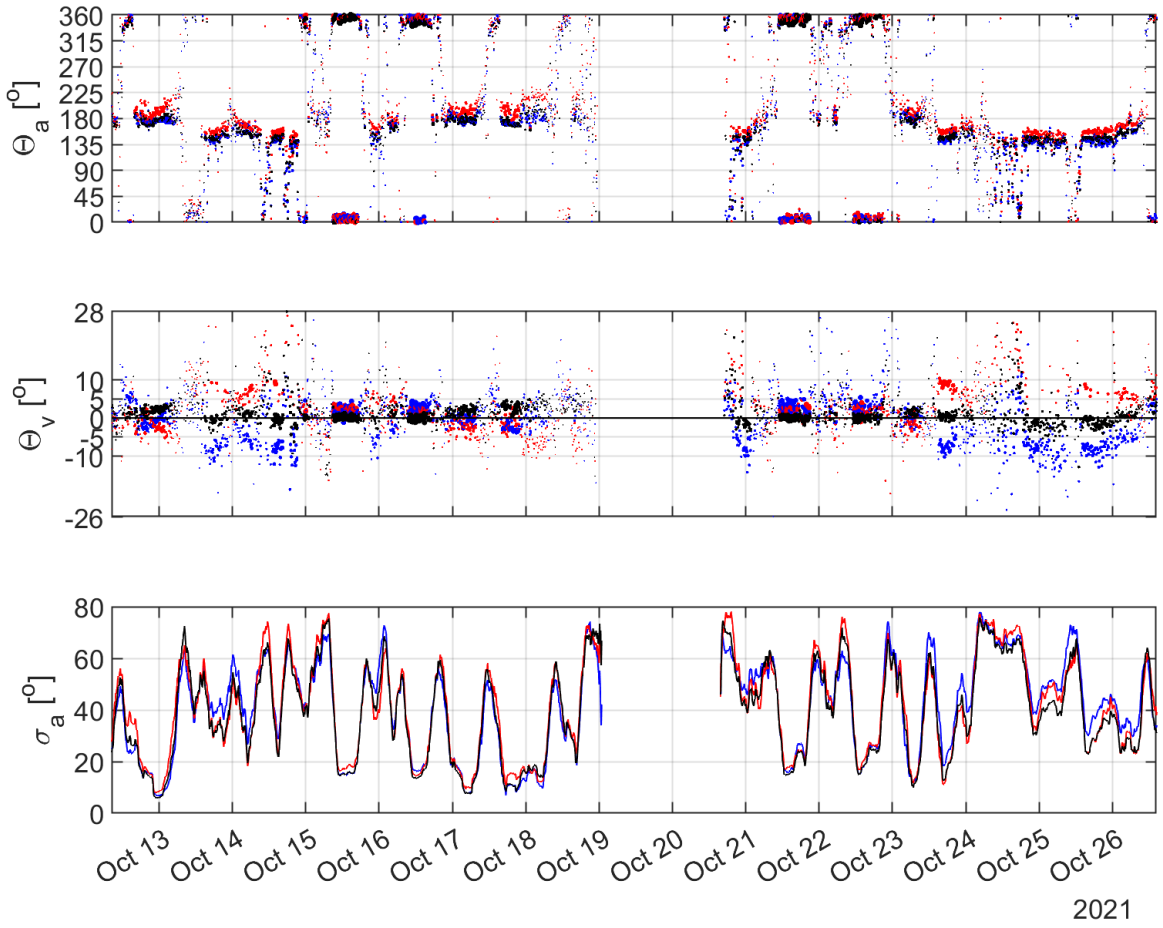

Figure 5.2: S1, S2, and S3 (colored) (a): 10-min mean WD_a, (b): Tilt of the wind vector from the $(xy)_r$-plane, θ_{v_r}, and (c): 10-min standard deviation of θ_a, σ_a.

5.1.1 Low-Frequency Variability of u_r, v_r, w_r, and T_s

To distinguish between synoptic scale forced and diurnally forced wind conditions in the ski-flying hill, the 24-h periods are divided into two main categories; "clear weather days", which are considered diurnal forced days, and cloudy days, which did not have a clear diurnal signal. Oct 12, Oct 15, Oct 16, Oct 17, Oct 18, Oct 21, Oct 22, and Oct 26 shown in Fig 5.1 are considered cloud-free days. The eight cloud-free dates have a strong daily/diurnal signal, especially visible in the along-slope wind component, v_r, and in observed temperature, T_s, on the knoll in Vikersundbakken. The difference between T_s and the observed valley floor temperature (1.5 km South, 250 m height difference), which exceeded $5°C$ during some of the nights, justifies the visual categorization based on the diurnal forcing.

The wind components revealed a clear diurnal signal, with a maximum wind speed and v_r around 90 minutes after noon local time, and a minimum v_r around 90 minutes after the time when T_s decreased the fastest. The simultaneous relation between v_r and T_s was (not surprisingly) strongest during the clear weather days, and the 24-h

Table 5.1: Statistical parameters of $u_r, v_r, w_r, WS, WD_a, \theta_v$, and T_s for reference S1/S2.

variables	$u_r[m\ s^{-1}]$	$v_r[m\ s^{-1}]$	$w_r[m\ s^{-1}]$	$WS[m\ s^{-1}]$	$WD_a[^\circ]$	$\theta_v[^o]$	$T_s[^\circ C]$
mean	0.24/0.10	-0.14/-0.20	-0.01/0.07	1.76/1.66	120/153	-4.3/19.3	6.58/6.56
max	2.27/2.21	7.32/7.13	0.52/0.67*	7.64/7.32		56.3/84.1	15.8/13.5
min	-1.98/-1.19	-3.62/-4.52	-0.45/-0.20*	0.11/0.10		-38.5/-44.0	-2.2/-1.8
σ_{tot}	0.84/0.77	1.97/1.91	0.36/0.34	1.31/1.30			3.28/3.16
$\overline{\sigma_S}$	0.57/0.54	0.67/0.62	0.47/0.40	0.60/0.56	40.7/40.8		0.30/0.27
max $\sigma_{\overline{S}}$	1.86/1.75	2.06/2.10	1.44/1.26	1.96/1.95	102/103		2.38/1.43
min $\sigma_{\overline{S}}$	0.06/.04	0.05/.07	0.05/0.04	0.05/0.06	4.8/6.5		**0.03**/0.03

Table 5.2: Statistical parameters of $u_r, v_r, w_r, WS, WD_a, \theta_v$, and T_s for middle S3

variables	$u_r[m\ s^{-1}]$	$v_r[m\ s^{-1}]$	$w_r[m\ s^{-1}]$	$WS[m\ s^{-1}]$	$WD_a[^\circ]$	$\theta_v[^o]$	$T_s[^\circ C]$
mean	**0.18**.....	**-0.25****	0.02	**1.79****	139	6.4	**6.61****
max	2.10**.....	**7.60**.....	0.27**.....	**7.89**.....		51.7**.....	13.8
min	**-1.62**.....	**-4.48**.....	**-0.16**.....	0.08**.....		**-57.8**.....	-2.1
σ_T	0.78.....	**2.07**.....	0.34.....	**1.37**.....			3.19
$\overline{\sigma_{T_{10min}}}$	0.56.....	0.65.....	0.43.....	**0.60**.....	39.0**.....		0.25**
max $\sigma_{T_{10min}}$	1.59**.....	**2.19**.....	1.30.....	1.94**.....	103.....		1.59
min $\sigma_{T_{10min}}$	0.05.....	0.06.....	0.05.....	0.04**.....	4.9.....		0.03

correlation coefficient (R) between $\overline{T_s}^{10s}$ and $\overline{v_r}^{10s}$ ranged from -0.14 (from 1100 UTC, Oct 24) to 0.87 (from 0000 UTC, Oct 16). Despite the correlation between the along-slope velocity and sonic temperature being negative on three of the dates (Oct 14, Oct 24, and Oct 25), there was great significance between the two variables ($p < 10^{-5}$) on the two first dates, but not on Oct 25 ($p \approx 0.03$).

5.1.2 Sonic Temperature

The moving mean of the sonic temperature (T_s) in VH ranged from below -3 $^\circ C$ to above 15 $^\circ C$. The diurnal signal was noticeable every day except a 24 h period starting on Oct 24 at 1100 UTC, which can be seen in Fig 5.1 d. The diurnal signal of $\overline{T_s}$ was present in all other 24 h periods with the largest amplitude (5 $^\circ C$) from Oct 12 0800 UTC to Oct 13 0800 UTC. Significant differences between each individual SA position were not of interest, but S1 had a longer period hit with direct sunlight in late afternoons which resulted in larger positive fluctuations in T_s. This explains the mean 10-min standard deviation of 0.30 $^o c$ for S1, compared to 0.27 $^\circ C$ for S2 and 0.25 $^\circ C$ for S3.

The moving average of T_s was ranging from 9.6 $^\circ C$ to 10.4 $^\circ C$. The 10-min variability of T_s during the stationary temperature period was also low, averaging a 10-min block standard deviation of 0.11 $^\circ C$ with a maximum value of 0.20 $^\circ C$ which was detected on Oct 25 at 0600 UTC together with a 0.5 $^\circ C$ drop in the trend from the moving mean. The minimum standard deviation in this period was σ_{T_s} = 0.04 $^\circ C$ (1300 UTC, Oct 24). This was relatively close to the global minimum for of σ_{T_s} = 0.03 $^\circ C$, which can be found in Table 5.1 and 5.2. This minimum was measured in the morning of Oct 18, approximately 4 hours after the minimum T_s of -2.2 $^\circ C$ at 0530 UTC approximately 1 hour before noon local time. This period was dominated by downwind and crosswind towards the judge tower.

5.1.3 Precipitation

In the morning of Oct 19 about 10 cm of snow were observed in Vikersund. Precipitation data collected from the official weather station in Geithus (64 m.a.s.l) measured a total of approximately 8 mm this night. Except for Oct 19, the campaign period was not associated with any precipitation.

The precipitation intensity at the jumping hill is not measured directly but indirectly captured by the LiDAR radial wind speed v_{rl}. This can be seen in Fig 5.1 b, as a 0.6 ms^{-1} discontinuity in the SA measurements and the LiDAR measurement at 0000 UTC, Oct 19, which corresponds to a terminal velocity of $\sim 1.0\ ms^{-1}$. This terminal velocity is proportional to the tenth root of the equivalent melted drop diameter (*Langleben*, 1954), which is connected to the precipitation intensity. According to *Gergely and Garrett* (2016), the terminal velocity of $\sim 1.0\ ms^{-1}$ is associated with mean precipitation intensity > 1.5 mm h^{-1}.

5.2 Spatial Variability of the (Low-Frequency) Wind Components along the Ski-Flying Slope

Different statistical measures of atmospheric variables for the entire campaign period P_{300} measured at the three SA positions are listed in Tab. 5.1 and 5.2. Extreme values in both the variable and the associated standard deviation are presented as a 10-min mean ($\overline{\mathbf{u}_r}$, $\sigma_{\overline{\mathbf{u}_r}}$). The following subsections will contain the overall description of the mean wind components during the campaign as a function of across-slope position, and along-slope position (WC100s measurements of v_{rl}). Data from the WC100s provide information about the 2D distribution on its scan plane over the ski jumping hill. The reference/center WS ranged from 0.11/0.08 $m\ s^{-1}$ to 7.43/7.89 $m\ s^{-1}$, and the 14-day mean was 1.71/1.79 $m\ s^{-1}$. The time series of WS is not shown, but the magnitude of v_r, where v_r is shown in Fig 5.1b, was often very close to the absolute 3D Wind Speed (WS). The reference/center variability of WS represented as a 10-min standard deviation, ranged from $0.05/0.04\ m\ s^{-1}$ to $1.96/1.94\ m\ s^{-1}$ with a mean of $0.58/0.60\ m\ s^{-1}$.

The mean reference/center along-slope component ($\overline{v_r}$) ranged from -4.07/-4.48 ms^{-1} to 7.22/7.60 ms^{-1}, and with a total mean of -0.17/-0.25 ms^{-1}. Note that the reference maximum is the average between S1 and S2, where S2 had a minimum of -4.52 ms^{-1}, and S1 with much lower magnitude (-3.62 ms^{-1}), as shown in Table 5.1. The slope experienced a reference/center TW (v_r<0 ms^{-1}) 61.4/61.9 % of the total campaign period P_c. The S2 position, closest to the judge tower, experienced 62.5 % TW, but the stronger TW conditions in the S3 positions were enough to still have a $\overline{v_r}^{S3} < \overline{v_r}^{S2}$. The effect of this stronger TW in the center is that a ski jumper is expected to be influenced by a stronger TW than estimated by the current WF, and is further discussed in 6.2. The differential momentum in the S3 position is more complex, and also a function of the reference TW magnitude (See Fig 6.2).

The reference/center variability in v_r, described by the standard deviation ($\sigma_{\overline{v_r}}$), ranged from 0.06/0.06 ms^{-1} to 2.08/2.19 ms^{-1}. On fair weather days, the smallest $\overline{\sigma_{v_r}}$ was typically around 06 UTC (08 LT). This component is also investigated for y_r positions further down the slope profile, and the temporal mean as a function of $(xy)_r$ position is shown in .This is the temporal mean for the time periods of sufficient LiDAR

data shaded gray in Fig 5.1b.

The across-slope wind component ($\overline{u_r}$) ranged from -1.59/-1.62 ms^{-1} to 2.24/2.10 ms^{-1}, and with a mean of 0.17/0.18 ms^{-1}. The reference minimum was the average between two relatively different $\overline{u_r}$ values from the position of S1/S2 (-1.98/-1.19 ms^{-1}). The reference/center standard deviation $\sigma_{\overline{u_r}}$ ranged from 0.05/0.05 ms^{-1} to 1.81/1.59 ms^{-1}. In general, the three positions (S1, S2, and S3) showed a different distribution of the wind vector along the rotated xy plane, where S1 was exposed to the strongest positive u_r components, both for negative and positive v_r (see wind roses in Fig 5.3).

The mean $\sigma_{\bar{u}}$, shown in Table 5.1 and 5.2 as $\overline{\sigma_{\bar{S}}}$, was in the order of 10 % larger on the North side (S1) than the South side (S2), where the value in the center was in between the two boundary sonics. Time series of standard deviations (10 s) of u_r, v_r, w_r are shown in Fig 5.5, which includes 3-h moving means of each individual position (S1, S2, and S3). Despite the xy plane consistency connected to the across-slope distribution of the standard deviation in the wind component, the mean of the standard deviation in horizontal wind direction ($\overline{\sigma_{WD_a}}$) was significantly higher in the center than the boundary positions(also shown in Table 5.1).

Horizontal Wind Direction

Time series of the horizontal wind direction (WD_a) are shown in Fig 5.2a. The overall wind direction typically changes between HW and TW conditions with larger v_r components than u_r components. Except for some time periods of strong TW, the majority of the Vikersund slope experienced wind conditions with small cross-wind components. More precisely, around 55 % of P_{300} measured $0/180^\circ \pm 22.5^\circ$ for S1 and S3, whereas S2 measured more than 60 % of WD_a within the same range. The direction of the mean wind, however, indicated a u_r value in the same order as the v_r. All three sonics are exposed for Not surprisingly, the mean absolute v_r was much larger than the absolute u_r (around 3 times larger for S3, a little less for the boundary positions). The majority of the momentum was either originating from WD_a= 180° or WD_a= 0/360° (along-slope direction), especially in the periods where the variance of the direction was low which are marked gray in Fig 5.2. The along-slope direction is where local maximums both in measurement density and WS are found. However, under TW conditions ($90^\circ \leq WD_a \leq 270^\circ$ in Fig 5.3) there are two local maximums in WS for all three sonic positions. This secondary local maximum is easterly flow typically under synoptic scale forcing, where topographical effects also caused a positive cross-slope component anomaly towards S1 on the north side. This resulted in a $WD_a \approx 155^\circ$ for S3 and S2 positions, but with a peak of WS measured by S1 slightly shifted towards positive u_r ($WD_a \approx 145^\circ$). This is also seen in the higher positive mean u_r in the S1 position. The mean 10-min standard deviation of WD_a was 40.8^o for S_{ref} and only 39.0^o for S3, where S1 and S2 were very similar (40.7° and 40.8°). Maximum of the quantity was similar for all three SAs (103^o), and the minimum was below 5.0^o for S1 and S3, and 6.5^o for S2.

Along-slope Mass Transport

If we assume that the mean wind changes linearly between S1 and S3 (North section), and S3 and S2 (South section), we have a 1D cross-section of mean mass transport at H_S = 3.5 m. Further, based on LiDAR observations of v_r in different heights above

the surface (see Fig 5.7), we assume that v_r is (on average) more or less constant with height (or linearly increasing magnitude). This justifies the assumption of a mean mass transport in $H_S \in [3.0,\ 4.0]$ m is closely similar to the mean mass transport in this 2D section when $\frac{dv_r}{dz} = 0$. This can be used to calculate an estimated mean mass transport through the North and South cross-sections defined by the across-slope length between the measured v_r and in the H_S height. The 14-day mean along-slope mass transport through the North cross-section ($\overline{M_{X^+}}$) becomes

$$\begin{aligned}
\overline{M_{X^+}} &= \overline{v_r}^{X^+} \cdot \overline{\rho_{air}} = \frac{1}{2}(\overline{v_r^{S1}} + \overline{v_r^{S3}}) \cdot \overline{\rho_{air}} \\
&\approx \frac{1}{2}(-0.14\ ms^{-1}\ -0.25\ ms^{-1}) \cdot 1.25\ kg\ m^{-3} \\
&\doteq \underline{\underline{-0.24\ kg\ s^{-1}\ m^{-2}}},
\end{aligned}$$

and the South cross-section ($\overline{M_{X^-}}$) becomes

$$\begin{aligned}
\overline{M_{X^-}} &= \overline{v_r}^{X^-} \cdot \overline{\rho_{air}} = \frac{1}{2}(\overline{v_r^{S3}} + \overline{v_r^{S2}}) \cdot \overline{\rho_{air}} \\
&\approx \frac{1}{2}(-0.25\ ms^{-1}\ -0.20\ ms^{-1}) \cdot 1.25\ kg\ m^{-3} \\
&\doteq \underline{\underline{-0.28\ kg\ s^{-1}\ m^{-2}}},
\end{aligned} \tag{5.1}$$

where X^+ and X^- is the cross-sectional distance X_{S_1} - X_{S_3} and X_{S_3} - X_{S_2} respectively, described in 3. This corresponds to a 14 % stronger mean TW component on the South side (closest to the judge tower) compared to the other side. The WS, however, indicates the opposite (3 % higher WS on North side). This is likely due to the lee effect from steep topography on the South side for negative u_r conditions, which can be seen in Fig 5.3 for horizontal wind direction WD_a between 180° and 225°

The Slope-Perpendicular Component

The steep slope of Vikersund and the complex topography around forced the wind vector to deviate from the $(xy)_r$ plane. The mean w_r, which is forced by topography from all directions, and perpendicular to the plane formed by the steepest gradient in the hill, was as expected slightly positive in the center of the hill (S3), 0.02 ms^{-1}. The mean of the boundary sonic measurements S1/S2 was -0.01/0.07 ms^{-1}, but with a much higher variability due to strong dependency of WD_a. Given that we have rotated the xy plane to align with the steepest topography gradient, one would expect a positive mean w_r. However, the two reference positions measured a wind vector θ_v deviating from the $(xy)_r$ plane in the opposite direction. S1 was located on the southwest side of a steeper gradient than the along-slope direction, which also happened to be one of the most frequent horizontal wind directions. This can be seen in Fig 5.3a, which shows the mean tilt close to -10° for WD_a around 145°, which is substantially steeper than the along-slope mean θ_v. S2 was located further away from this upstream steep gradient, and the most frequent horizontal wind direction was also 10 ° towards the negative u_r for the sonic closest to the judge tower. The S2 measured negative θ_v for a cross-wind component coming from the other side (judge tower side). S3 did not experience similarly high deviations from the $(xy)_r$ plane, but the key finding is the positive tilt for

TW conditions compared to HW conditions, which will be discussed in more detail in Section 6.1. Especially the periods where there is a mean deviation from the angle of the slope.

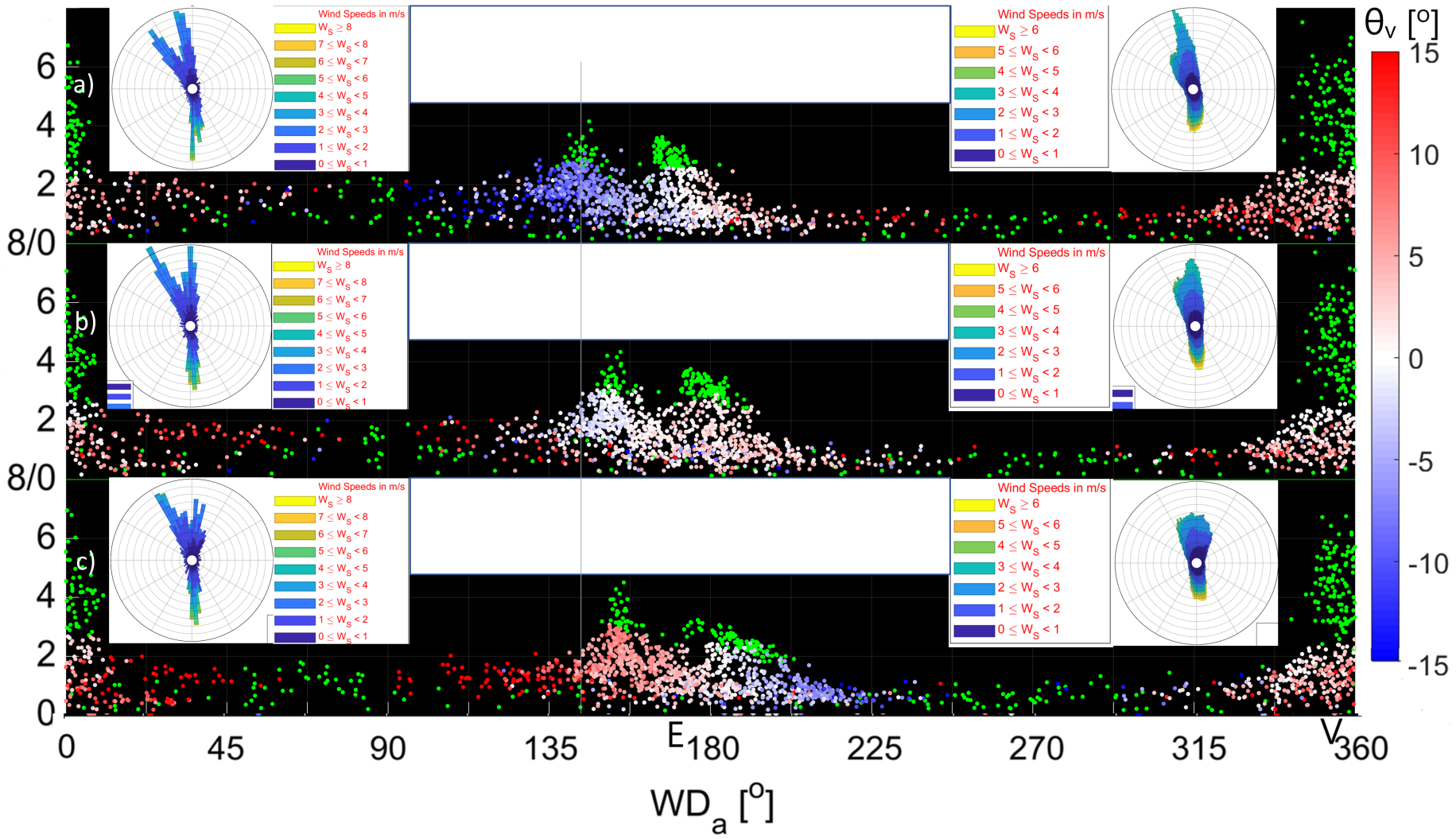

Figure 5.3: WS as a function of horizontal wind direction and tilt from the mean wind plane θ_{v_r} in colors for X-positions a) S1, b) S3, and c) S2. Dots marked in green color is wind conditions outside the wind corridor typically used in competitions. Wind roses on the left represent mean horizontal wind $\overline{\mathbf{u}_{xy}}$ for the X-position corresponding to the panel. Wind roses on the right are 10 s means.

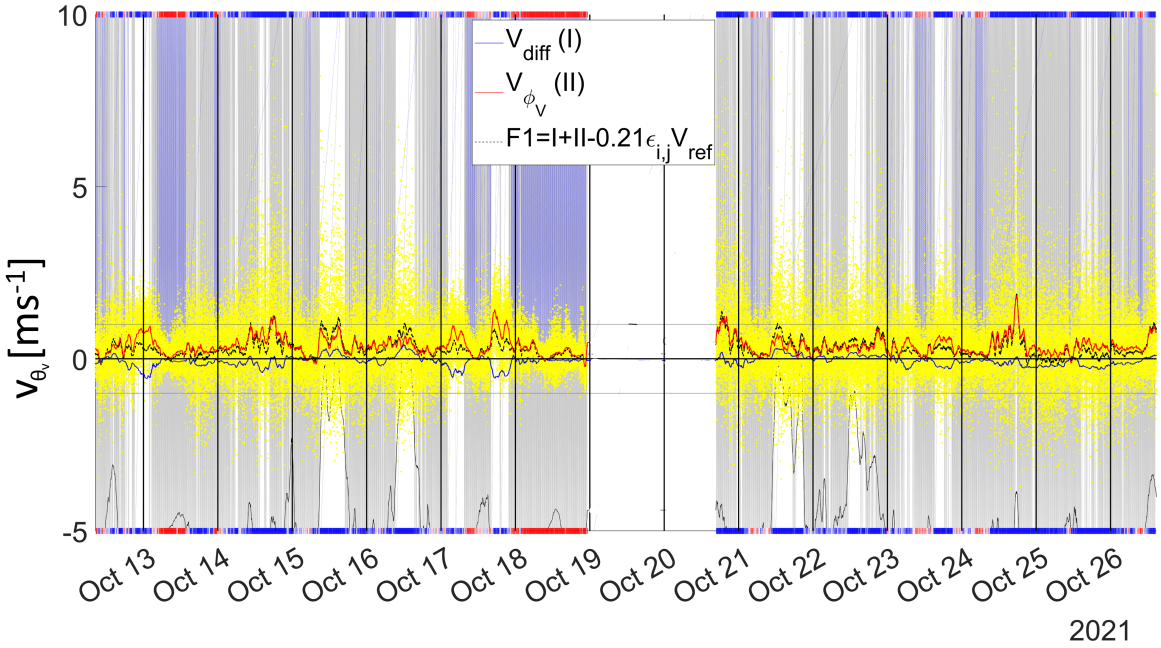

Figure 5.4: 10 s mean of $v_{\theta_{v_r}}$ measured with S3 representing tangential wind speed equivalent effect from the tilt of the relative wind W. The velocity W is in a moving coordinate system with constant velocity v_s = (30,0) ms^{-1} in the $(xy)_r$ plane. Colored lines represent the 1-hour moving mean of the different terms in F1, including v_{diff} and total F1. Time intervals shaded in grey are 10 min periods where at least 68 % of the 10 s mean is inside the corridor of $|v_{ref}| < 2.5ms^{-1}$. Blue shaded area is 10 min. periods of $\sigma_{v_{ref}} < 0.2ms^{-1}$ in at least 68 % of the 10 s means. The shading of the top and bottom frame is the relative amount of $\sigma^{10s}_{v_{ref}} < 0.2ms^{-1}$ for the 10-min period for its position.

5.3 Comparison of Reference Wind to the Center Wind

The mean wind vector $\overline{\mathbf{u}_{ref}}$ often indicates how well the following couple of 10-min periods are expected to fall inside a given competition corridor. Trends of the mean wind are often very well forecasted, and meteorologists working for typical regions as a ski-flying hill often know which kinds of synoptic-scale forcing fits best for competitions. This section is looking more closely at the higher-frequency spatial distribution, which is supposed to give statistics on how the wind vector behaves in different mean wind situations. Time series of difference in 10-s mean wind between center wind and reference wind ($\overline{\mathbf{u}_3 - \mathbf{u}_{ref}}^{10s}$) are shown in Fig 5.6.

During P_c, the magnitude of the transient spatial differences could be as high as above 2 ms^{-1} for u_r, 3 ms^{-1} for v_r, and did exceed 1 ms^{-1} in the w_r component on several occasions, especially on the negative side under strong HW conditions induced by the radiative heating on Oct 16, Oct 17, and Oct 21. The u_r component showed a relatively symmetric variation, giving quite small low frequency (3-h moving mean in Fig 5.6) trends. However, v_r and w_r had periods of stronger low-frequency trends, which correlated negatively to one another. The negative anomalies in the v_r component on Oct 17 and Oct 18 were associated with positive anomalies in w_r, which means the two anomalies act as a negative feedback mechanism on the jump length effect (canceling each other out). The negative periods of the deviation in the v_r component

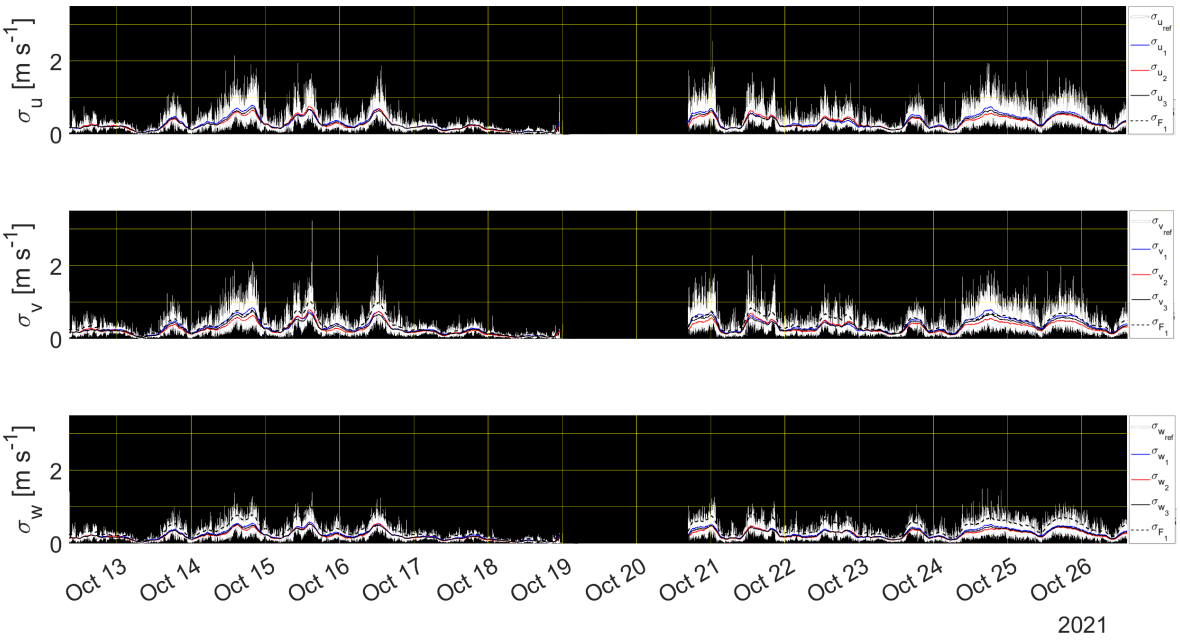

Figure 5.5: Standard deviations (σ) in $u_{ref}, v_{ref}, w_{ref}$ for 10 sec. periods. The variables measured by S1, S2 and S3 are represented as 3hr moving means of σ_{10sec}, and σ_{10sec} in the aerodynamic deviation function F_1 in dashed

were typically strong for reference $\overline{v_r}$ < -1.5 ms−1, which also is indicated in Fig 6.2a and b. Positive anomalies in the deviation were present under strong and turbulent HW periods. Nevertheless, these anomalies are not considered a challenge in the fairness evaluation of ski jumping because they are present in periods that already lie outside of the current FIS competition corridor (*Czarnecki*, 2020).

The variation in the across-slope differences follows the variation in the wind components, and FIS competitions are preferably held under standard deviation under a threshold value, suggested to be defined as 10-min periods having at least, and preferably well above 68 % of 10 s standard deviation of v_r less than 0.2 ms^{-1} on all measurement devices used in competition. During P_c, this threshold value was satisfied approximately one-third of the time, if including the 36-h period with insufficient sonic data (see the blue shaded area in Fig 5.4). The 36-h period did not have the high-frequency sonic data to describe it, but LiDAR (WC100s) captured the v_r scans every 12 s and is presented as 10-min temporal means due to a long time (>4 s) between each across-slope position (North, center, South).

Figure 5.6: Difference in 10 s mean wind components $\overline{\mathbf{u}_3 - \mathbf{u}_{ref}}^{10s}$ for P_c. Shading at the zero-line for the three velocity components indicates a 3-h moving mean.

5.3.1 Expected Deviation of Reference Wind Vector in Different Weather Conditions

The overall results reveal that the expected center wind typically has a negative deviation from the reference for along-slope wind component v_{ref} < -1.5 ms^{-1} as indicated in Fig 6.2a1 and b1, and a (less clear) positive deviation for v_{ref} > 1.0 ms^{-1}. For wind conditions inside the range -1.3 ms^{-1} < v_{ref} < 1.0 ms^{-1}, the expected v_{diff} is close to zero for both σ_{refmax} < 0.2 ms^{-1} and the higher standard deviation periods, and for σ_{refmax} < 0.2 ms^{-1} the zero expectation extended to -1.5 ms^{-1} on the negative boundary. The reference crosswind dependency (u_{ref})) of v_{diff} indicates that higher u_{ref} is associated with less negative v_{diff} (see Fig 6.4a), where the strongest negative is found when $u_{ref} \approx 0$ ms^{-1}, especially for TW conditions below the -1.3 ms^{-1} boundary. For higher standard deviation periods, $\mathbf{u}_{ref}$ gets a clearer tendency of a positive u_r component, especially for the TW conditions. This is also visible in Fig 5.3b, where we see a peak of the WS around 180° at S3, which is slightly shifted towards positive u_r component for S1 (a) and S2 (c).

The total jump length effect on an idealized ski jumper with perfect form and a given weight is a function of the drag and lift force associated with the atmospheric forcing. The w_r component, which is not accounted for in the WF, also has a (positive) effect especially due to a y-acceleration, which is explained in Chapter 4, Fig 4.1. w_r is (not surprisingly) dependent on the WD_a, but the position of the investigated fluid flow was very sensitive to this dependency. The S1 position experienced large negative anomalies in w_r when 90 < WD_a < 180°, whereas S2 experienced positive anomalies in similar wind conditions. However, S3, which is the expected x position of a ski jumper, had positive anomalies around 180° (See Fig 5.3). For S3, 180° and 155° were the most frequent WD_a, but the former cluster is associated with the highest w_r, and also the tilt of wind vector effect ($\chi\theta_v$ or v_{θ_v}) explained in 4. This can be seen visually in Fig 6.2, which also indicates that the periods of highest turbulence (bottom right plot) experience the most positive anomalies for positive u_r.

When analyzing v_{θ_v} independently on the crosswind component, the mean jump length effect becomes positive for v_{ref} < -0.3 ms^{-1}, and increases towards a maximum of $\sim$ 0.6 ms^{-1} (approximately +10 m jump length effect) at $v_{ref} \approx -1.8$ ms^{-1} (see Fig 6.2b, upper right).

5.3.2 WC100s: Comparison between Oct 19-20 and Oct 24-25

Further spatial information from WC100s can be used to describe the y_p dependency of the expected deviation between X_{S3} and X_{ref}. Oct 19 and Oct 20 were humid, cloudy, and calm, and are likely to fall within the category where σ_{refmax} < 0.2 ms^{-1}. Data on radial wind speed (RS) from the WC100s is used from three periods with different turbulent conditions. The earliest period was in the morning of Oct 24 from 0530 to 0900 UTC, which also is marked in gray in Fig 5.1. This morning was quite stable, and also inside the sigma-corridor for v_{ref} marked with blue in Fig 5.4. The temporal mean RS for the spatial mean shaded blue in Fig 3.2c was -0.16 ms^{-1}, which was fairly

comparable to v_{ref} measured by the SAs. This temporal mean was quite independent of the tangential position in VH as shown in Fig 5.7 a. The profiles for HW and TW conditions indicated that v_3 typically was 0.1 ms^{-1} stronger than the reference, and the change along the profile was larger and more consistent for HW - than TW conditions. One thing to note is that the sections in Fig 5.7 are not only along-hill sections but also vertical profiles since height above surface ranges from 3.5 m to 1.8 m from 66 m to 87 m jump length as shown in Fig 5.7 c. Therefore, the change along the section might be a result of the varying height above the surface in combination with wind shear. This difference is not expected to be large since the overall σ_{10s} is relatively small and the v_{ref} inside the 2.5 ms^{-1} corridor. However, this period was influenced by relatively strong cross-wind components oscillating between negative and positive values. Time series of v_{rl}^{diff} as a function of jump length position y_p, the spatial mean of v_{rl}^{diff} on y_p, and the reference v_r^{ref} is plotted in Fig 5.8a, b, and c respectively. Most of this period was associated with HW conditions, with a few periods of negative v_{rl}^{ref}, which is associated with precipitation on Oct 19 (see Fig 5.1d). The key result from the spatial distribution of v_{rl} is the y_p variations and the way it cancels out the total difference when moving down the hill slope y_p. However, the negative differences are noticeably larger in magnitude and the mean difference through this period was -0.03 ms^{-1}. In addition, the spatial mean difference is typically negative for negative v_{ref} and vice versa. The mean correlation coefficient (R) was 0.46 on the y_p position of the maximum positive correlation (y_p = 75 m, see Fig 5.8 a). Another aspect we observe is that the largest negative v_{diff} is typically located between 66 m and 90 m, which is the y_p position where the sonics measure the differences, which also indicates a negative mean difference.

On Oct 24 to Oct 25, the ski-flying hill was forced by a synoptic-scale storm, which carried wind speeds of above 21 ms^{-1} at 850 hPa height from 12 UTC, Oct 24 and almost a day forward in time (*Norwegian Meteorological Institute*, 2023). This period also provided sufficient sonic data, and it was associated with standard deviations of v_r exceeding 1 ms^{-1}. This produced strong turbulence in the hill, with v_r and u_r components with equal order of magnitude ($WD_a \approx 135°$), which can be seen in the black box in Fig 5.9c, and with a v_r component mostly negative, and the u_r only positive. During this period, the low-frequency w_r component was close to zero (see Fig 5.6), whereas the v_{diff} term was negative, and horizontal wind directions with positive u_r and negative v_r ($WD_a \approx 135°$) are associated with a large horizontal gradient in the mean wind vector tilt θ_v. This period indicated a higher positive correlation between the reference tangential wind speed and the difference than the less turbulent humid period (R = 0.66 vs R = 0.46), where v_{diff} had a linear dependency of v_{ref} with higher inclination (see Fig 5.11 a and b) in this period than the less turbulent period starting from Oct 19. However, both days have very small to no correlation for $y_p > 125$ m.

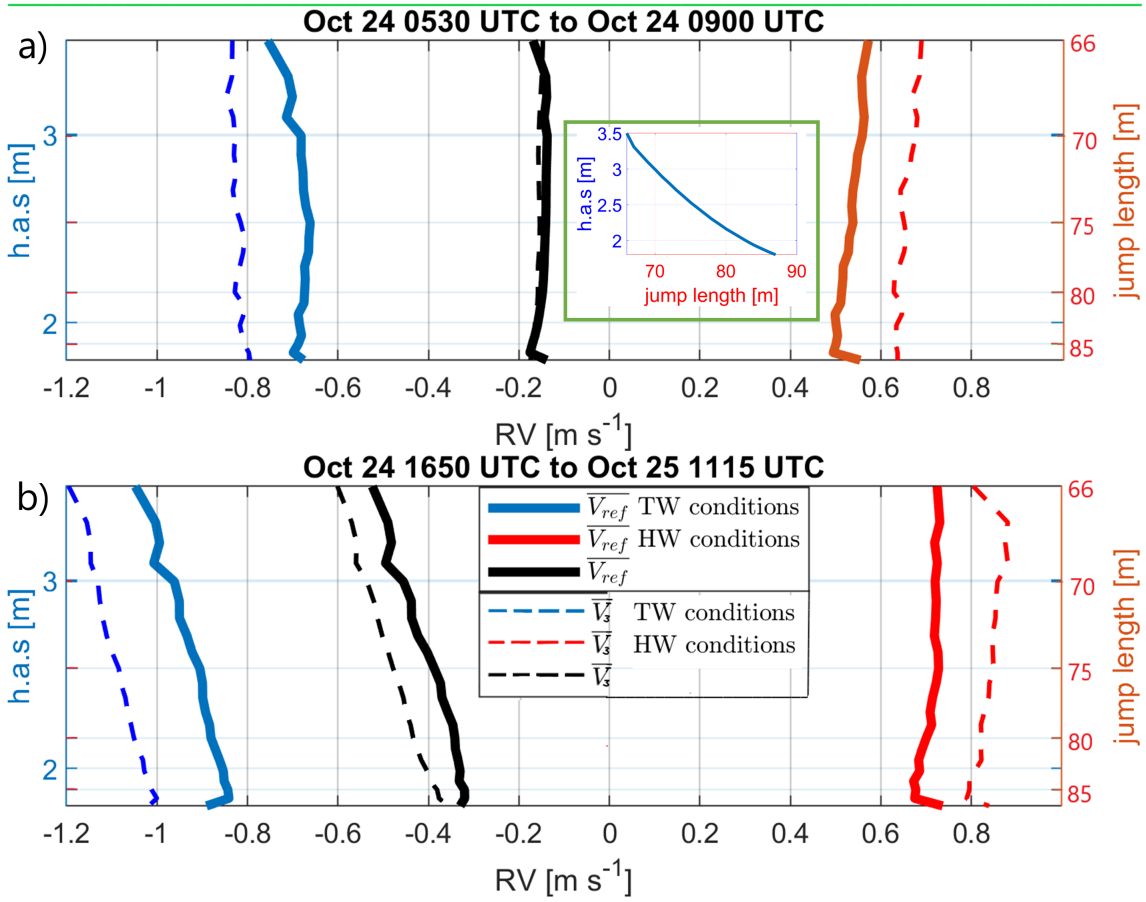

Figure 5.7: Profiles of temporal mean RS along WC100s scan in the nearest 20 m radius from the SA positions. Solid lines indicate a spatial mean between two boundary sections and dashed lines in the center section, which is marked in Fig 3.2c in 4 as two red lines and one black line respectively. Note that the RS value at 66 m jump length is the RS mean measured by the SAs. ***a):*** $\sigma_{v_{ref}} < 0.2\ ms^{-1}$. ***b):*** *height above surface (h.a.s) as function of jump length position of WC100s scan.* ***c):*** $\sigma_{v_{ref}} >> 0.2\ ms^{-1}$.

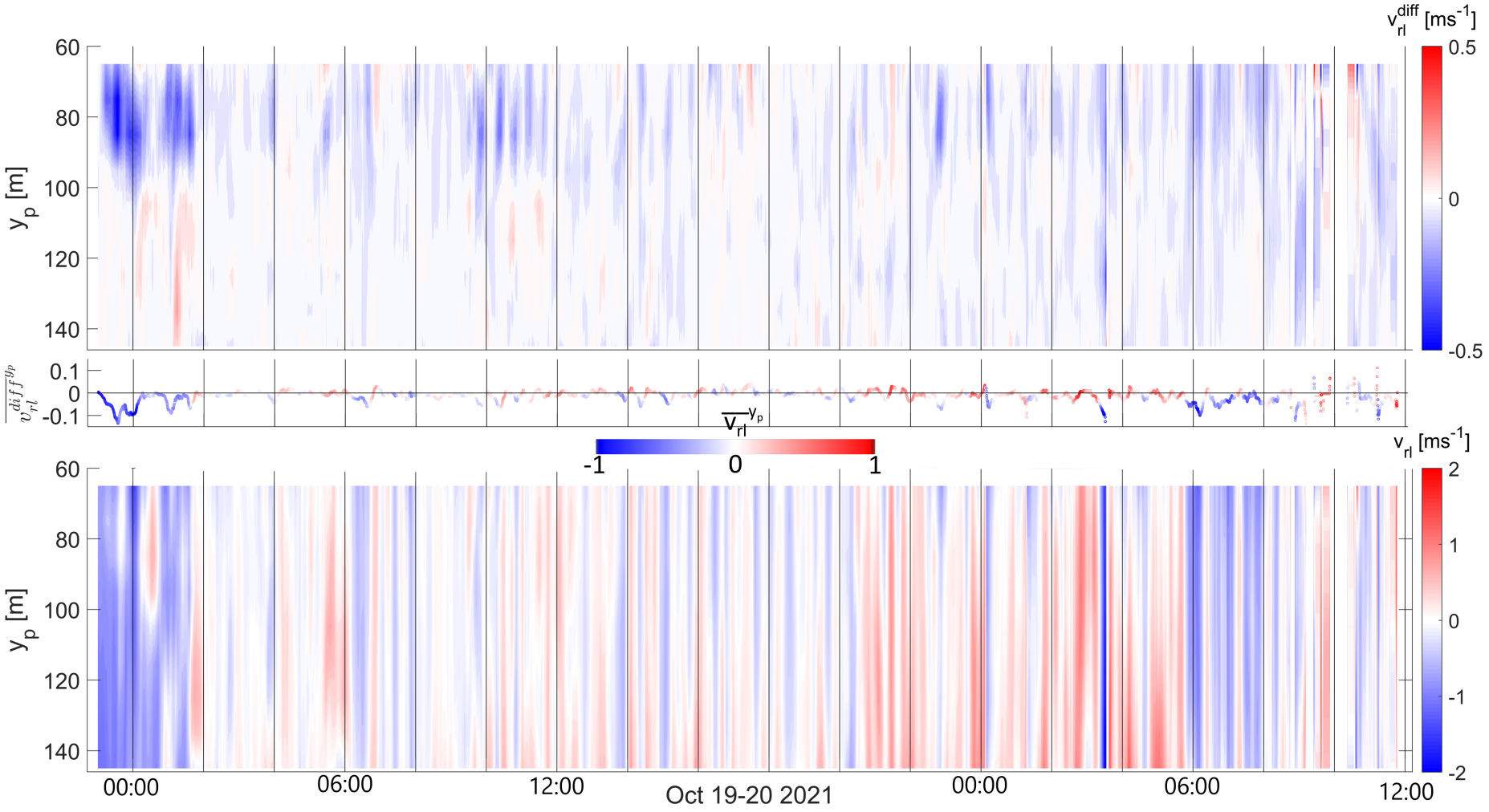

Figure 5.8: Along-slope spatial distribution time series of $\overline{v_{rl}}$ presented as (a): the reference deviation in the center ($\overline{v_{rl}^{mid} - v_{rl}}$), (b): the along-slope mean of this difference, where the color of the line is the along-slope mean reference ($\overline{v_{rl}}^{y_p}$), and (c): $\overline{v_{rl}}^{y_p}$ for as a function of y_p. Note that all velocity units are in ms^{-1} even though it is not specified everywhere.

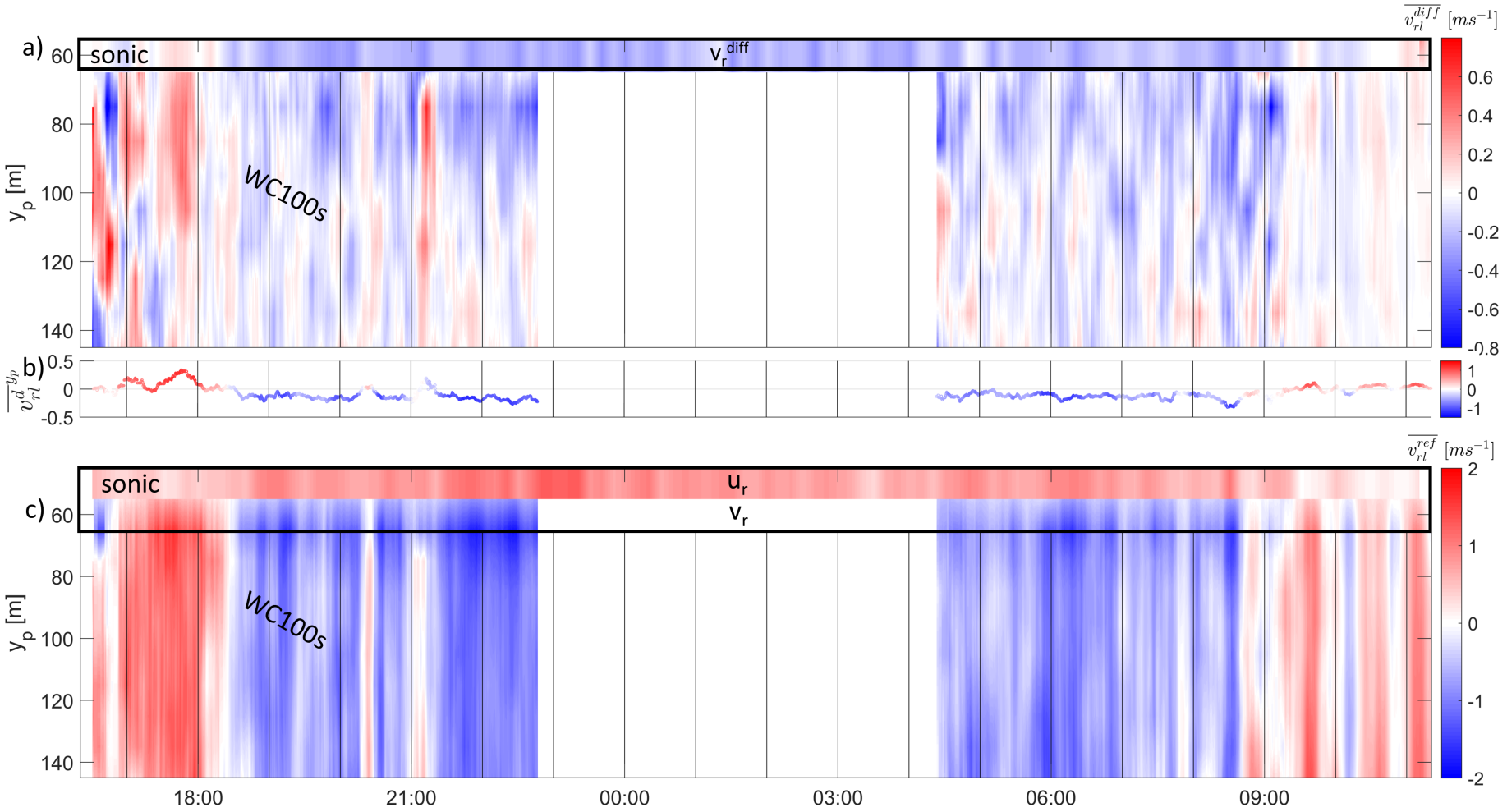

*Figure 5.9: As Fig 5.8 but for 1630 UTC, Oct 24 to 1115 UTC, Oct 25. Top panel in **a** and **c** are for y_p=66 m measured by sonic anemometer.*

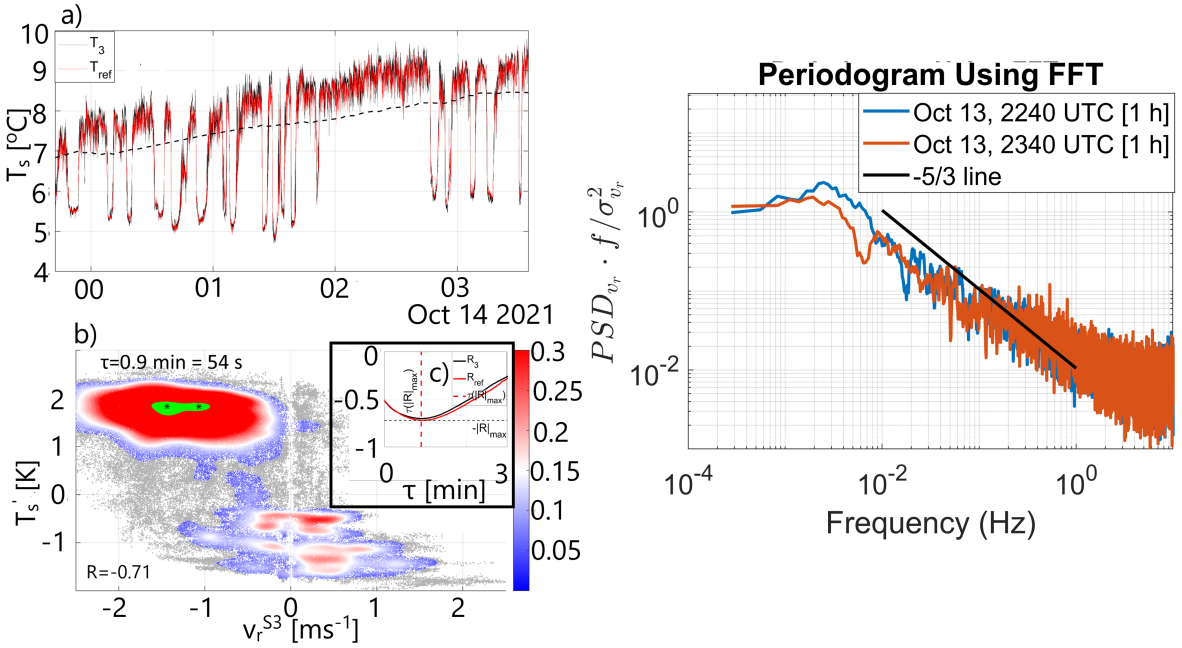

Figure 5.10: NBL oscillation period captured night times on October 14. (a): Time series of T_s. The dashed line represents the background sonic temperature ($\overline{T_s}$) as a 3 h rm. (b): Scatter of v_r and T_s' for the timelag (τ) of maximum $|R|$. Shading is measurement density ρ_{ref} normalized by the maximum measurement density ρ_{max}. Gray dots: $\rho_{ref} < 0.05$. Green shading: $\rho_{ref} > 0.95$. (c): Correlation coefficient R as a function of timelag τ. (d): Normalized PSD (smoothed 10 frequency steps) for two consecutive 1 h periods (before and after the start of the oscillation period).

5.3.3 Oscillating Nocturnal Boundary Layer Observed by the Sonic Anemometers

During two clear nights in Vikersund, especially on Oct 14, the stable nocturnal boundary layer forming in the night stabilized even more during the night due to advection of warmer air in the height that did not reach down to the valley floor. This can be seen in Fig 5.1d, indicating a rapidly cooling valley floor (Geithus, Modum 64 m.a.s.l), whereas the knoll area of Vikersundbakken (300 m.a.s.l) showed a clear warming trend. The background sonic temperature had a positive trend of 0.4 $K\ h^{-1}$, which can not be explained by anything else than an intrusion of warmer air in the height, since longwave radiation forcing led to cooling on the valley floor. However, some mixing of the cold air from the valley floor influenced the slope of Vikersundbakken, likely forced by the shear production between the synoptic-scale warming air layer in the height and the stable and cooling layer below it. This is seen in the T_s measurements from the area, which was intruded by $4°C$ colder air (see Fig 5.10a). The duration of the presence of the $4°C$ colder air ranged from barely a minute up to seven minutes, which also corresponded to oscillations in v_r (not shown in figure). Maximum temperature difference reached 3.5 K around 0130 UTC, which was around 1 minute after the maximum v_r of 2.3 ms^{-1} (not shown). The temperature difference between Vikersundbakken and Geithus was around 5 K in this period.

During the period investigated in Fig 5.10, T_s and v_r correlated negatively $R_{ref} =$

-0.71. Both positions correlated the most for a timelag corresponding to T_s measurements 54s later than the v_{ref} measurements. The none-synchronized ($\tau = 0$) correlation coefficient was approximately 30 % smaller than the optimal timelag ($\tau = 54s$, R=0.71). The correlation coefficient as a function of timelag can be seen in Fig 5.10c. We introduce a period length defined by the number of consecutive 10 s mean v_r ranging from a few to above 200 consecutive 10 s means, but more than 75 % of the period experienced TW ($V < 0$). The sonic temperature T_s varied locally depending on the Lagrangian advection of the inversion due to turbulent kinetic energy fed by shear forces. The exact position of the strongest vertical shear and its magnitude would be helpful to know in context to the larger scale TKE forcing and its influence on the slope of Vikersund. Data from the scanning LiDAR can be found in data from the profiling LiDARs at the top and bottom of the profile (see Chap. 3 for positions of these instruments). However, shear production above the sonic anemometers induced by i.e low-level jets is to some extent visible in the normalized power spectral density (PSD) changes, and *El-Madany et al.* (2014) used three 1 h periods before, under, and after a low-level jet event, and found that PSD dropped substantially in for frequencies of around 0.005 Hz (10-min periods) approximately 1 h after a low-level jet. This also was the case this night in Vikersund, and 1 h before the period discussed in Fig 5.10 there was almost an order of magnitude higher normalized PSD than for the following hour (see Fig 5.10d. This is likely due to a period of strong shear stress between the stable valley surface layer and the synoptic scale warm air intrusion above. Time series of T from the valley floor (Geithus, Modum) shows that the strong inversion in the valley was not replaced by the warmer air mass before the daytime forcing after sunset warmed the valley floor around 11 UTC (see Fig 5.1d). The temperature difference between the two layers indicated a growing trend in the first half part of the period, and stationarity for the rest half period.

5.3.4 Distribution of v_r between the Three Sonics and w_r Effects at S3 Position

After the warm air intrusion starting from around midnight on Oct 14, the center of the y_p = 66 m position experienced negative v_diff, and a strong positive tilt term v_{θ_v}. The mean v_{diff} and v_{θ_v} was -0.1 ms^{-1} and +0.6 ms^{-1}, which also can be seen as time series in Fig 5.4. This period was influenced by two different WD_a (or θ_a) periods, where the dominant one was around 160° (see Fig 5.2). The other WD_a present is HW conditions ($WD_a \approx 0°$). The HW conditions were characterized by a positive v_{diff} and a tilt term close to zero.

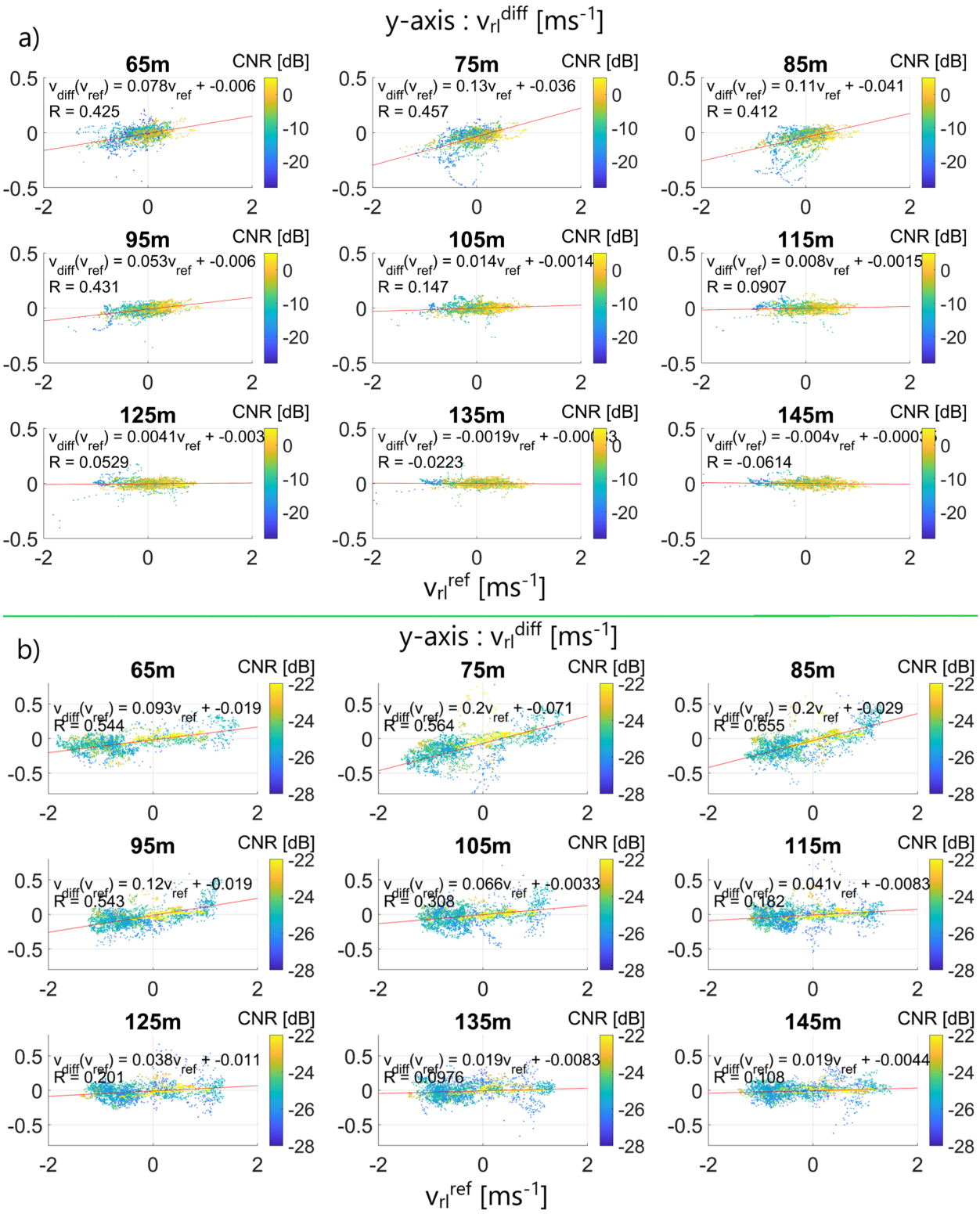

Figure 5.11: Correlation analysis of v_{rl}^{diff} and v_{rl}^{ref} on 9 jump length positions (y_p) in Vikersund ski-flying hill. (a): Oct 19 - Oct 20 (3166 random samples), time series in Fig 5.8. (b): Oct 24 - Oct 25 (3166 samples), time series in Fig 5.9. Shading is CNR value for the given scatter point.

Chapter 6

Discussion

The following sections will focus on the fairness question associated with the WF compensation used in FIS ski jumping competitions, where the main focus is the resulting aerodynamical tangential wind speed function (F1) output value in certain mean wind conditions. Detailed information about F1 can be found in Section 4.2.

6.1 Wind Factor Evaluation Based on the Input of Estimated Wind Component

The fairness associated with the WF compensation by FIS has several shortcomings (see chap 2), where one of them is the measurement and linear estimates of the wind influencing the ski jumper deviating from the true value. The difference in v_{tan} (v_{diff} measured in the center is assumed to be zero for all mean wind conditions, when in fact it has shown to be non-zero for some 10 s mean v_{tan} measured in the center in the knoll area of Vikersundbakken. Probability density function (PDF) analysis of v_{diff} shown in Fig 6.1 indicates that TW conditions are associated with small negative expectations of v_diff. Unfortunately, the distribution (which is fairly well normal distributed) is associated with a high standard deviation of the v_{diff}, which was higher for calm conditions ($|v_{ref}| < 0.5$ ms^{-1}) than for the more windy conditions ($\sigma_{calm} \approx 0.5$ ms^{-1}, $\sigma_{windy} \approx 0.3$ ms^{-1}). For the lower turbulent period (indicated with a red line in Fig 6.1), the opposite distribution was observed ($\sigma_{calm} < \sigma_{windy}$).

The PDF analysis of v_{diff} does not provide any direct information about the u_{ref} dependency associated with v_{diff}. However, the crosswind also has a substantial effect which is visible, especially for the strongest TW conditions in Fig 6.2a which is expected to have the highest negative anomalies for small u_{ref}.

Another aspect to note is that the input value is a 1D wind component v_{tan}, which is expected to be the most influential wind component associated with the jump length effect. The crosswind effect does not have an aerodynamical influence given that the trajectory of the ski jumper is perfectly along-slope (*Mikko and Juha*, 2022). However, crosswind can have an indirect effect, which relates to its dependency on the slope-perpendicular component w_r. Observations of w_r in the center of the hill confirm this dependency, but it also indicates that its high-frequency standard deviation (10 s) can be responsible for very rapid changes in an expected jump length. The key finding on the crosswind effect is that sufficiently strong TW conditions (v_{ref}) < -1.3 ms^{-1}

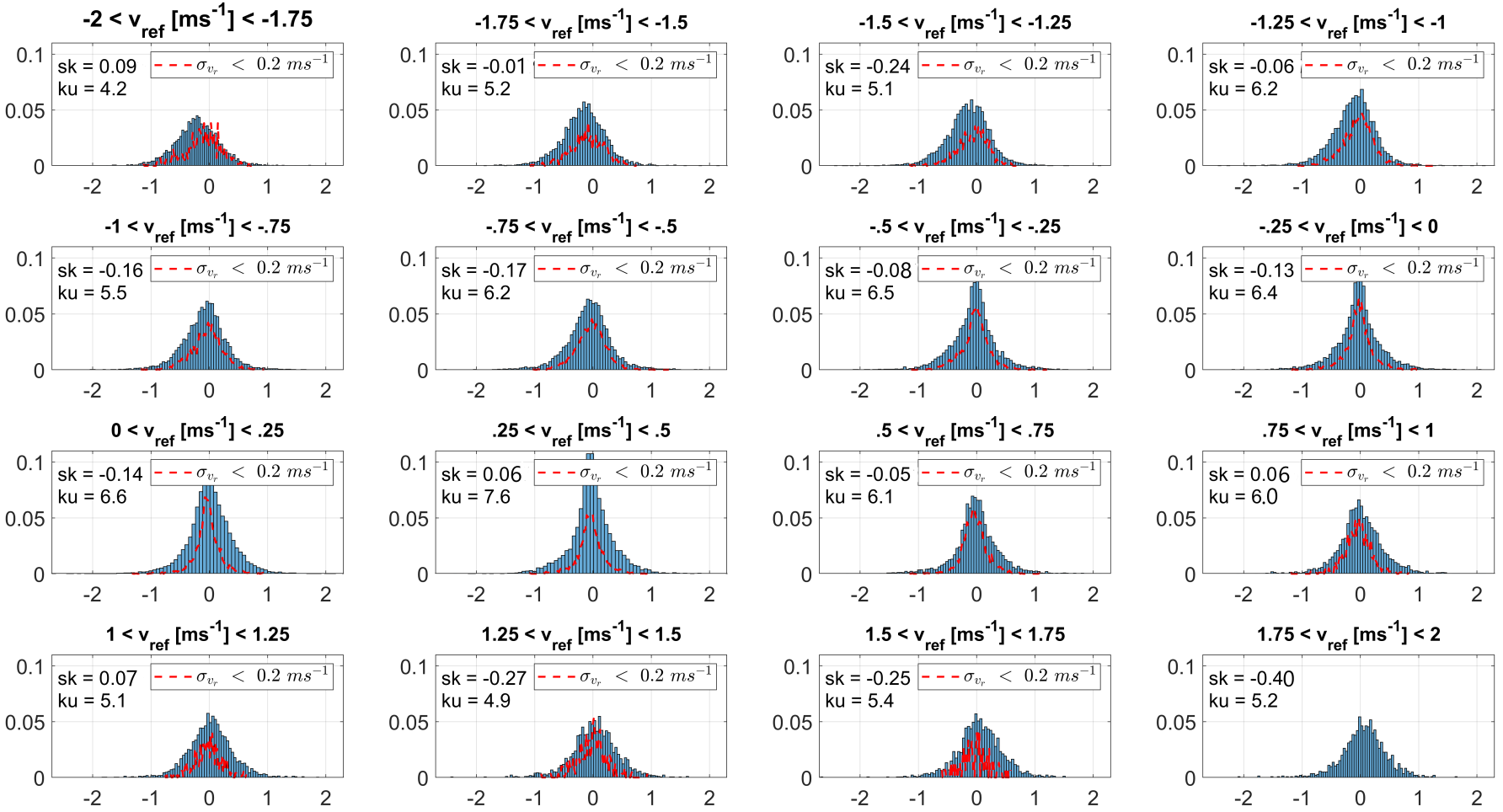

Figure 6.1: PDF analysis of v_{diff} (x-axis) in 16 different v_{ref} categories in wind conditions ranging -2 ms^{-1} < v_{ref} < 2 ms^{-1}. Red line is PDF for lower turbulent periods ($\sigma_{v_{refmax}}$ < 0.2 ms^{-1}).

are associated with positive jump length effects due to positive anomalies in w_r (or tilt term v_{θ_v}), especially for $u_{ref} < 0$ ms^{-1} (see Fig 6.2b). Negative anomalies for v_{diff} for $u_{ref} > 0$ ms^{-1} even strengthen this positive jump length effect for $u_{ref} < 0$ ms^{-1} in this v_{ref} region. For higher turbulent conditions the tilt term is less dependent on u_{ref}, but the v_{ref} dependency changed such that HW conditions are associated with stronger positive anomalies of the tilt term, and TW conditions are more variable and experiencing a mix of negative and positive anomalies (see Fig 6.2b lower panels). Nevertheless, the variability of aerodynamical effects on 10 s timescales can act as a buffer on the total effect (integrated spatially over the slope profile). This is because stochastic forcing on shorter time scales tends to sum up to zero when integrated over a far enough distance. The main issue is to know the expected aerodynamical effect as a function of y_p, and that the shorter eddy length scale associated with higher turbulence becomes an empirical challenge due to the higher observational resolution required. By LiDAR measurements covering at least a y_p section of 70 m (of comparable h.a.s.l of a ski jump trajectory). The LiDAR data shows that the v_{ref} and v_{diff} typically correlate positively but with the highest linear incline rate for $y_p < 95$m. This was the case for both low turbulent and high turbulent conditions (see Fig 5.11). No significant correlation was found for both cases for $y_p > 125$ m.

All the non-linear effects contributing to a fairness challenge associated with the WF compensation (in this study v_{diff} and v_{θ_v}) are very complex. Their expected value becomes dependent on the variables y_p, $\mathbf{u}_{ref}$, and TKE. In addition, the defined center of the hill might deviate from the true ski jumper trajectory, giving the ski jumper position deviations (x'_r, z'_r). From measurements on the knoll in Vikersundbakken, large x_r gradients in $\mathbf{u}_r$ are captured, both in wind speed and direction, but the most groundbreaking was the large tilt-gradient ($\frac{d\,\theta_v}{dx_r}$) between S1 and S2, especially at TW conditions with a positive u_r (see Fig 5.3). By convention, one might therefore expect that a ski jumper having a trajectory on the side closer to the judge tower is expected to fly longer than a ski jumper passing on the other side, and the effect of this becomes larger for higher wind speeds. It might therefore be a benefit for a competitor reading this thesis before the Raw Air competition in Vikersund starting on Mar 17, 2023. It might also be a misleading tip due to the fact that measurements done in this study did not capture snow-covered wind conditions, and, most importantly, they were taken without the windshield nets used during competitions.

The topography perpendicular to the along-slope flow is steep on both sides, which kind of generates a horizontal shear in a similar manner as the vertical shear above the surface. Instabilities arising from horizontal shear have been studied by i.e (*Mathis et al.*, 2004), and one key aspect to take to account is that even though small shears generate non-linear instabilities, other forcing (i.e surface heating, or vertical wind shear) is much more influential. On larger scales, the Coriolis acceleration tends to work as a sink of shear instabilities (*Mathis et al.*, 2004). This means that TKE does not depend significantly on v_{diff} itself, indicating that we can assume that the standard deviation of the velocity components is independent of v_{diff}, but not $\mathbf{u}_{ref}$ and $\frac{d\,T_s}{dt}$. The two latter variables are measured by FIS during competitions, and v_{diff} can be measured outside competitions.

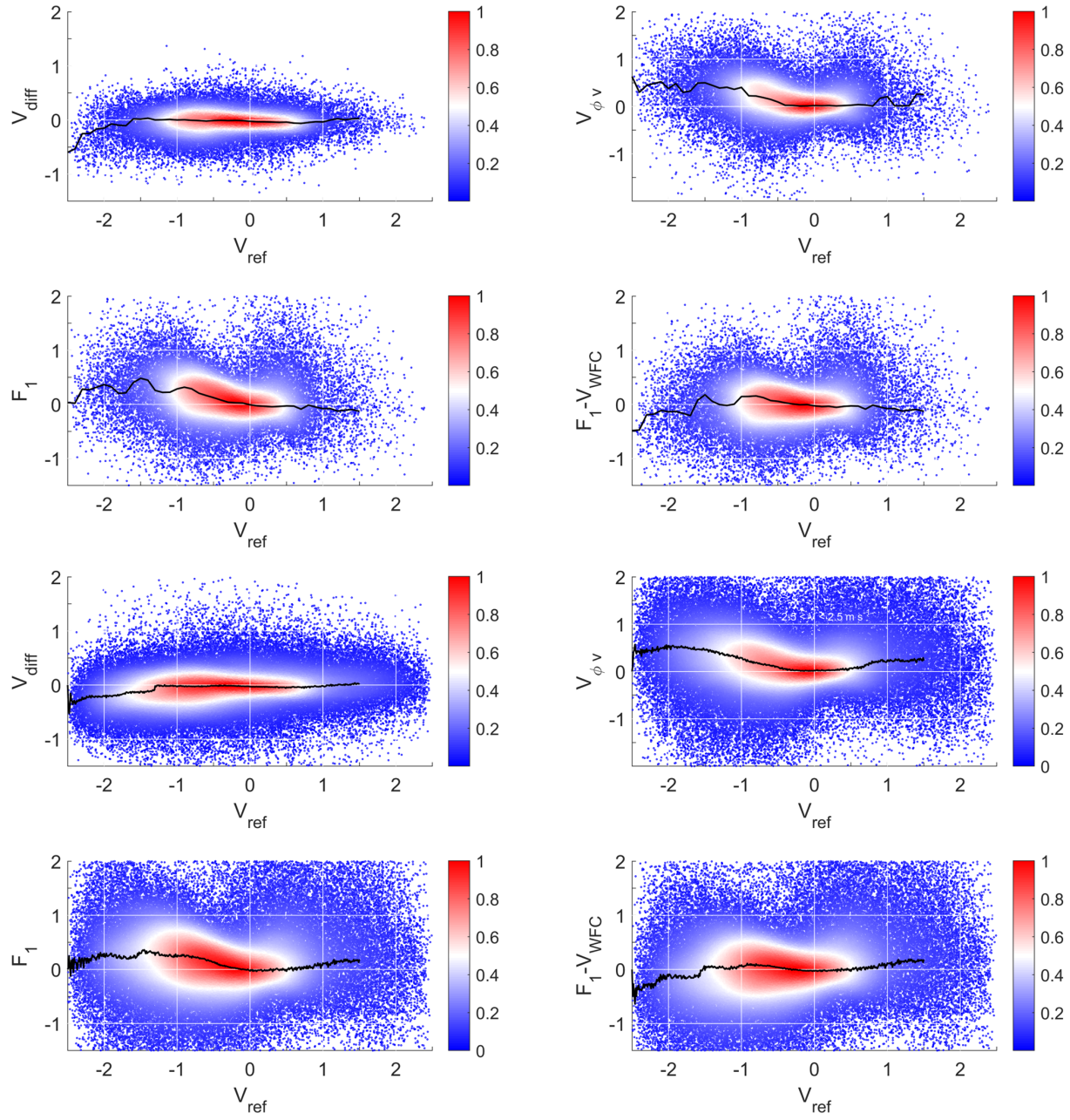

*Figure 6.2: F_1-terms as function of v_{ref} including only wind measurements where $|V_{refmax}| < 2.5\ ms^{-1}$. **a)**: $\sigma_{refmax} < 0.2\ ms^{-1}$. **b)**: all σ. The numbers **1**, **2**, **3** and **4** represents v_{diff}, v_{θ_v}, '$F_1 = V_{diff} + V_{\theta_v}$' and '$F_1 + 0.21\varepsilon_{i,j}v_{ref}$' respectively. Shading is the density of the scatter in the given (v_{ref},$F_1 - term$) - position, where the black line is the v_{ref} position of highest density. The density shading script is from (Nils, 2023)*

6.1.1 Tangential Wind Speed Function

The tangential wind speed function (F1) is simply the sum of the two terms discussed in the previous section. It creates a picture of an expected deviation in the total aerodynamic jump length estimated by the WF. Fig 6.3 Shows the a 2D PDF distribution of the F1 output, as a function of u_{ref} and F1. The distribution reveals that negative v_{ref} are associated with a positive F1 anomaly, especially for low u_{ref} or negative u_{ref}, which corresponds to what is visible in Fig 6.4. For $v_{ref} > -0.75$ ms^{-1}, the distribution is rather symmetrical with the expectation of F1 = 0 ms^{-1}, and the v_{ref} classes shifts between having a positive shifted expected value and a negative expected value.

The resulting F1 is dominated by the positive aerodynamic effect from the tilt term v_{θ_v}, which also is shown to be the term that is the most sensitive to small WD_a changes during wind conditions where $|v_{ref}| > 1.5$ ms^{-1}

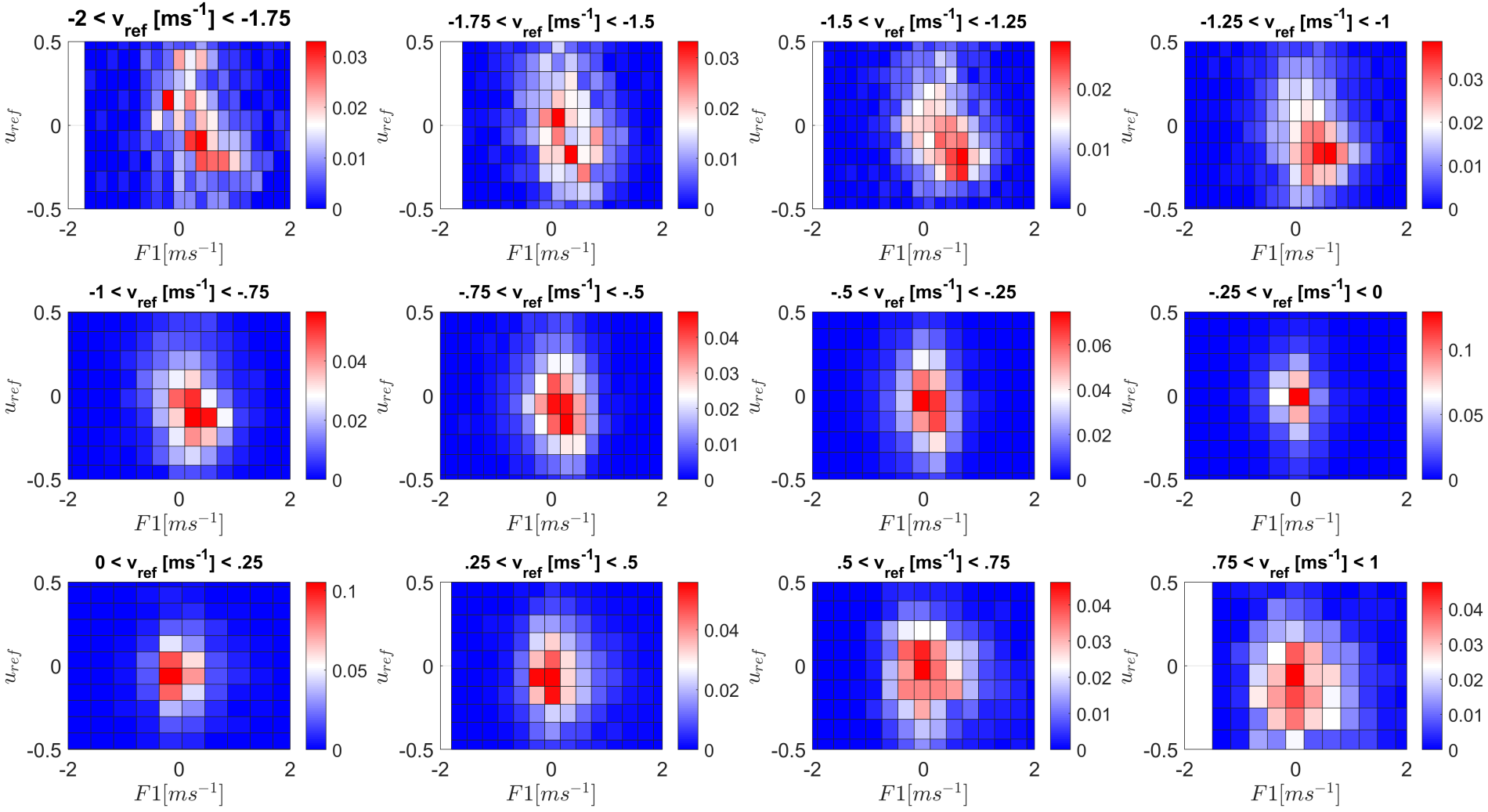

Figure 6.3: PDF analysis of F1 (evaluated for $\varepsilon_{i,j} = 0$) represented by a 2D histogram. The v_{ref} is divided into 12 categories and evaluated against u_{ref} with a requirement of $\sigma_{v_{refmax}} < 0.2\ m\ s^{-1}$.

6.1.2 Topographic Effects

The data was collected in a period of no snow cover and vegetation containing more leaves than average during the winter season. The effect of this is that the roughness length becomes longer, and the turbulent forcing is fed by a strong shear forcing in the total TKE budget. Whereas in February/March, when a cold surface due to snow cover increases the stability of the air, the negative buoyant forcing and the lower shear due to less friction are the main negative (anomaly) contributors in the TKE budget. This means that the higher turbulent periods with $\sigma > 0.2\ ms^{-1}$ do not necessarily create a picture of how the wind vector structure looks in February. However, standard deviations measured by the reference divided into classes could be used to address this problem. For example, if σ_{refmax} measured by FIS is less than 0.1 ms^{-1}, a WF as a function of Y-position could be given for this turbulent period and vice versa.

Another challenge is adjustments in the upwind topography. This could be the production of buildings or structures around the ski flying hill, or it can be forestry or demolition of old human-made structures. Vortices generated by buildings propagate downstream if and only if a so-called cylinder aspect ratio reaches a critical value ratio dependent on the background atmospheric forcing (*Sumner et al.*, 2004). The formed vortices will affect the fluctuations in especially w_r, and potentially change the structure of the spatial turbulence between the two reference anemometers. Due to the coordinate system rotated 28.11^o based on the HW conditions only, the TW-condition tilt anomaly is not centered about zero. In fact, the mean tilt was only 26.1^o in stable TW conditions, which indicates a positive mean tilt effect. This is shown in Fig 5.4, where the mean positive $v_{\theta_{v_r}}$ of 0.3 ms^{-1} is due to the mean positive contribution in TW conditions. The tilt effect is significantly closer to zero for less turbulent periods (σ_{refmax}<0.2 ms^{-1}) than for the remaining period as shown in Fig 6.2a2 and b2. Most importantly, the tilt effect is more consistent as a function of $\overline{v_{ref}}^{10s}$ and $\overline{u_{ref}}^{10s}$ for the low standard deviation periods. Another aspect to mention is that the tilt effect is connected to the discussed crosswind effect, explained by a strong correlation between θ_v and WD_a, especially at the reference positions during TW conditions, $160° < WD_a < 200°$ (R_{S2} = -0.59, R_{S1} = +0.43). The linear relation between θ_v and WD_a and regression analysis can be found in A. This can be explained by the inertia of the mass transport feeling the upwind less steep topographic gradient when $|u_r| >> 0\ ms^{-1}$, which results in a positive anomaly in w_r for TW conditions and a negative anomaly in w_r for HW conditions. Both cases are compensated by a tailwind negative anomaly in v^{diff} and a headwind positive anomaly in v^{diff}. In the HW situation ($0\ ms^{-1} < v_r < 2.5\ ms^{-1}$), an increase in the standard deviation is associated with a positive anomaly in w_r and the tilt term (see Fig 6.4b). This is likely due to HW conditions typically has a strong buoyancy contribution (positive contribution on w') in high TKE periods. This effect might be very different in the snow-covered winter season, but it will be present as long as the buoyancy term in the momentum equation of mean w plays a role. This term is large when the slope is starting to warm by direct sunlight. For Vikersund hill, the warming of the slope starts in the evening transition and is replaced by a rapid cooling of the slope after sunset. The fast resulting decrease in w anomalies during the evening transition is associated with a decrease in the tilt term in F_1, but the magnitude of the tilt term is approximately proportional to v_r for small enough v_r. This means a given wind vector tilt is associated with less jump length effect for $|v_r| < 0.5\ ms^{-1}$ than higher

tangential wind speeds.

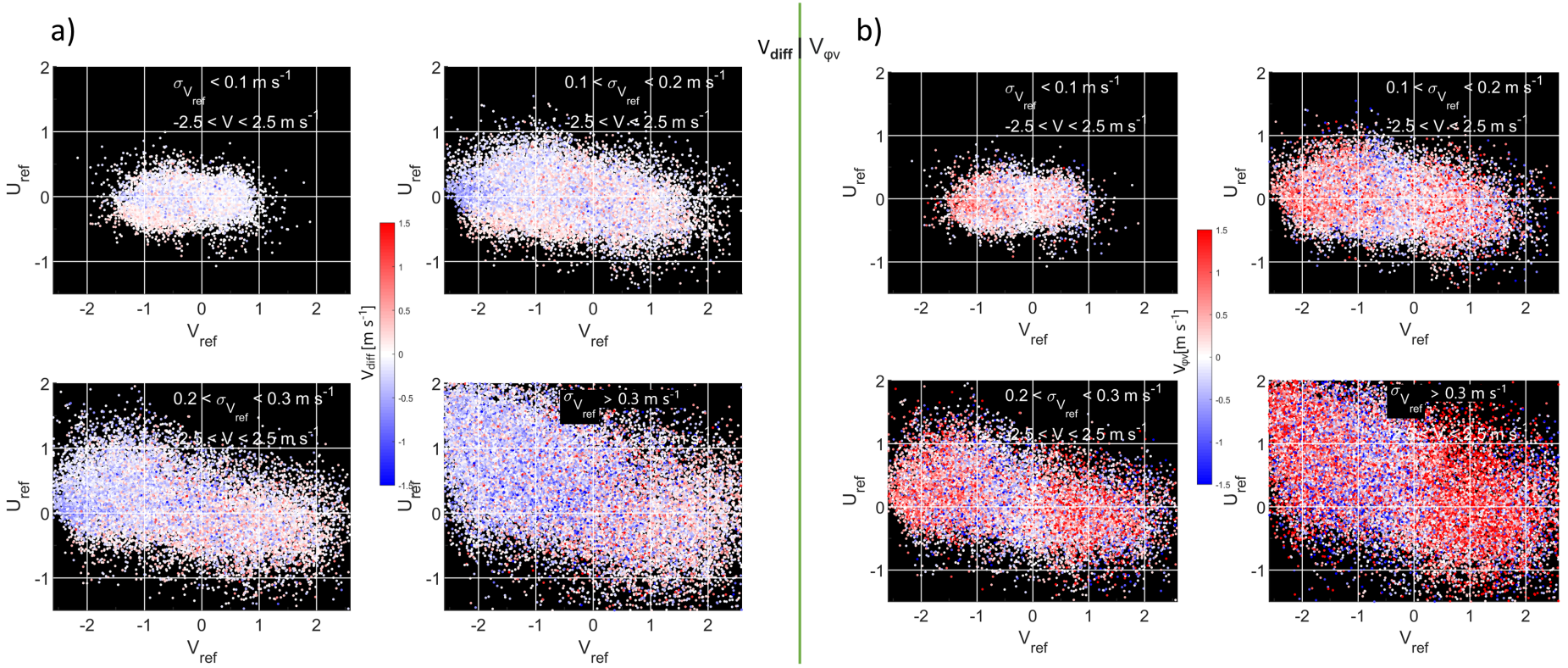

Figure 6.4: 10-sec mean F_1-terms as a function of u_{ref} and v_{ref} in four different turbulent conditions defined by intervals of 10-sec $\sigma_{v_{ref}}$. a) v_{diff} without the $\varepsilon_{i,j}$-factor. Grey shaded areas is inside $|v_{ref}| < 2.5\ m\ s^{-1}$, but it is a region where either v_2 or v_1 is typically lower than $-2.5\ m\ s^{-1}$. b) $v_{\theta_{v_r}}$.

The challenge with TW conditions compared to the HW conditions, as previously addressed in studies as (*Aldrin*, 2015; *Czarnecki*, 2020; *Jung et al.*, 2021a; *Virmavirta and Kivekäs*, 2012a), becomes the main challenge associated with the estimate of the true **u** effect, which includes the most groundbreaking wind vector tilt effect, which in certain horizontal wind ($\mathbf{u}_{xy}$) conditions overcome the negative v_{diff} effect. This effect originates from the upwind topography gradient being dependent on WD_a, and can be fairly approximately to be proportional to anomalies in the wind vector tilt relative to the ski jumper (angle of attack), as deducted in Chap. 4. In the winter/spring season, many FIS competitions are held in the afternoon, typically from 16 LT and towards sunset. Under clear and calm conditions, the radiative heating of the westward-oriented ski flying hill in the hours before sunset transitions to strong radiative cooling. This happens when the sun disappears behind the mountains. The consequence of this is that the cold and dense air formed close to the surface will be denser than the surrounding air and it will slide down the hill. Such periods might be a challenge for the fairness connected to the WF compensation. When conditions change from HW to TW, the wind vector tilt also does (typically from 28° to 26°, see Chap 4). If TW gets strong enough, and the competitors late in the competitions are very lucky with the crosswind component, only the tilt term can be responsible for a jump length effect > +10 m. Another aspect to consider is the stable and cooling layer at the bottom of the hill which also might slow down vertical momentum and force the fluid horizontally out of the hill, which would amplify the tilt effect even more. The evening transition is also associated with rapid cooling, meaning that the mean air density above the slope increases, which also contributes to a positive jump length effect (see Chap. 2). On Oct 17, the temperature dropped from $8°C$ to $4\ ^oC$ in less than one hour from 17:40 to 18:30 LT in the S3 position. By assuming the spatial mean of T for the entire ski flyer path dropped similarly in this period, the air density increase by 1.5 % by using the ideal gas law and assuming $T_s = T_d$ which corresponds to the similar positive change in the lift - and drag forcing given in Chap. 2, eq. 2.13. In a similar manner, a tangential wind increase of 0.25 ms^{-1} will correspond to $\left(\frac{30ms^{-1}+0.25ms^{-1}}{30ms^{-1}}\right)^2 \approx 1.7$ % in both drag and lift, which is equivalent to $\sim$ -3.6 points if $v_{ref} > 0$ ms^{-1}, and $\sim$ -4.4 points otherwise. Typical World Cup competitions or World Championship is held at end of February or the start of March when sunset is approximately at the same Local Time as in the mid of October. The cooling rate of an air layer close to the surface depends on the ground heat flux, turbulence, longwave radiation, and albedo (if shortwave radiation is present). In addition, mainly since the absorption layer of soil is thin and the heat capacity fairly high (40 to 70 % of water), the absorption layer is above a soil layer beneath it close to the annual maximum in October, and the opposite is close to the yearly minimum in February/March. The only factor that is reversing this cooling rate a bit is perhaps the albedo effect. Snow cover prevents the skin layer of the surface from being heated during daytime, keeping the air temperature close to the surface low. A complete cover of new snow avoiding the surface from being heated during the day will dampen the cooling rate after sunset, but this scenario might be rare this late in the winter season, especially according to the climatology in South-East Norway.

6.2 Fair Atmospheric Conditions Based on the WFC System and Predictability of True Wind

One challenge is to give a reasonable compensation score based on atmospheric conditions, another one is to determine time periods where the tangential wind estimated by this method is sufficiently close to the real tangential wind. The center wind is not always close to the linear interpolation between two boundary anemometers. For VH, at approximately 40% of K-point position, the 10s means of v_{diff} shown in Fig. Fig 6.2a1 confirm the expectation that non-linear forcing will be present in - and outside of competitions. In some occasions, this non-linearity will be as high as above 1 ms^{-1} even with conditions considered as non-turbulent ($\sigma_{refmax} < 0.2\ ms^{-1}$). Even though the maximum standard deviation of S1 and S2 is beneath this limit, the standard deviations in the middle S3 positions can be as high as 1 ms^{-1}.

The WF compensation model uses an expected v_{diff} of zero (*Czarnecki*, 2020), but actually, on average, the $|V_{diff}| >> 0$, and especially while TW-conditions. During TW - conditions and small u_r- component ($|u_{ref}| < 0.25\ ms^{-1}$) and low standard deviation in v_{ref} ($\sigma_{10s} < 0.1 ms^{-1}$) the magnitude of the v_r- component is "stably" higher than the reference. The maximum difference from the reference occurs when $v_{ref} = -2.5 ms^{-1}$, measuring a v_{diff} of $-0.5 ms^{-1}$. However, when $u_{ref} < -0.25\ ms^{-1}$ for the same defined turbulent condition, we get the opposite effect with a $v_{diff} > 0$. The negative effect occurring for $|u_{ref}| < 0.25\ ms^{-1}$ is somehow compensated for by a tilt-effect of the wind vector (θ_W) making the total atmospheric forcing closer to the expected forcing calculated by the WFC-methodology with a positive v_{diff}-equivalent effect v_{θ_v} as seen in Fig 6.4b. The wider range of the magnitude of v_{θ_v} is because the Taylor approximation for the tilt term deducted in Section 4.2 is only valid for low relative wind tilt θ_W. The total effect, F_1 turns out to be positive and increasing for higher TW magnitude winds. Shown in 6.2 aIII, we see a trend of -0.6 ms^1 per magnitude of v_{ref} for $v_{ref} < -0.2\ ms^{-1}$. Under HW the standard deviation in the v_{diff} was around 50 % higher than under TW conditions.

During P_c, which happened to experience a wide range of meteorological conditions spanning from high turbulent periods typical when the temporal mean magnitude of the cross-wind component u_r was high, to stable periods of along-slope winds typically in the period between sunset and sunrise. The first thing to note is the mean of the tangential wind speed, which was $-0.21 ms^{-1}$ in the center of the hill and slightly higher on the boundary of $-0.17 ms^{-1}$. This can be explained by the large sheltering effect of the topography on S1 and S2 during a negative v_r- component, which is not present for v_r > 0 ms−1. The mean cross-wind component (u) of S3 (0.18 ms^{-1}) falls nicely between S1 and S2 value, where U1 was largest (0.24 ms^{-1}) and U2 smallest (0.10 ms^{-1}). The high crosswind component in S1 and the significantly higher standard deviation linked to all the velocity components confirm that a higher crosswind is highly correlated with mechanical turbulence which we want to avoid during FIS competitions. Interestingly, the mean w_r - component measured in S1 is negative and has the opposite sign of S2 and S3, and the standard deviation in the w_r component was 13 % higher in the S1 position, whereas it was only 3 % higher in the u_r- and v_r. The nonlinearity of the true tangential wind for 10 s. mean winds are present in every v_{ref} and for both low standard

deviations $\sigma_{refmax} < 0.2$ and standard deviations higher than that. As seen in Fig 6.2a1 and b1 the expected v_{diff} is close to zero for $|v_{ref}| < 1.2\ ms^{-1}$. Approximately 80 % of the wind measurements inside this corridor fall within $|V_{diff}| < 0.3\ ms^{-1}$ in the less turbulent periods, whereas the 80 % confidence interval is higher during high standard deviation periods in Fig 6.2b1, and especially for tangential wind speeds approaching -1 ms^{-1} from the positive side.

In these two boundaries we see an abrupt drop to $v_{diff} \approx -0.2\ ms^{-1}$ followed by a further drop of $0.4\ ms^{-1}$ per magnitude of v_{ref} for $\sigma_{refmax} < 0.2\ ms^{-1}$ and $0.2\ ms^{-1}$ per magnitude for higher standard deviations. One more thing to note in Fig 6.2a is that the abrupt drop in the v_{diff} around $v_{ref} = -1.5\ ms^{-1}$ is added with an abrupt drop in the v_{θ_v}-term, doubling the abrupt negative effect from v_{diff} as to be seen in a3. This makes the $v_{ref} \to -1.5\ ms^{-1}$ region being extra dangerous in context to the fairness question around the WFC system. In the more turbulent case, the v_{θ_v}-term has this smooth 0.6 gradient which not is disturbed by sudden drops or increases.

If we add on the tangential wind effect used by FIS under TW-conditions, like is done in a4 and b4, the function now becomes the tangential wind-equivalent advantage/disadvantage a ski jumper would experience if the 21 % additional compensation was excluded in that position. Evidently, this shows that for TW-conditions with $v_{ref} < -1.5\ ms^{-1}$ are disadvantageous if this requirement is removed. By keeping the same 21 % extra for TW-conditions it still is an advantage as long as $-2.5 < v_{ref} < 0\ ms^{-1}$. However, for $v_{ref} > -1.5\ ms^{-1}$ it is actually still an advantage, but less advantageous than when including the 21 % extra compensation.

Chapter 7

Conclusions and Outlook

Further research on the quality of wind data to be used in the WF compensation model is likely to be essential in the context of improving fairness in ski jumping. More information about the behavior of the wind vector in and around the ski jumping slope is shown to be crucial to have any indication about the expected wind conditions in the center of the hill. This study also reveals that very high spatial resolution might be required. Only by looking at LiDAR data of a small part of the slope profile y_p, we see that the mean expected v_{diff} dependency of v_{ref} starts from having a positive high correlation at y_p = 75 m (R = 0.46, a = 0.13), where **a** indicates the regression line incline (see Fig 5.11 a), to no significant correlation for y_p > 105 m. A similar trend is shown for more turbulent conditions in Fig 5.11b. LiDAR data does not have any information about the crosswind component, but sonic data indicate that the mean crosswind was high and positive during the entire period investigated in Fig 5.11b, which can be seen in time series of $\overline{v_{rl}}$ in 5.9 b. The overall PDF distribution of v_{diff} was close to normal distributed ($|sk| < 0.5$), slightly bell-curved (ku > 3). It would be idealistic to arrange competitions in conditions with high values of ku, which not surprisingly are found for low v_{ref} magnitudes. The ideal wind conditions for competitions would be at high ku values and a low y_p integrated mean v_{diff} having no correlation with v_{ref} and a known expected mean. Unfortunately, the results from this study do not find any evident reason to adjust the WF given from anemometers on the knoll of Vikersund, even though we find expected aerodynamic effects indicating a jump length effect deviating from the current estimated one from FIS. This is because the spatial distribution reveals that the expected v_{diff} (and v_{θ_v}) are very sensitive to small changes in position and/or mean WD_a. The most groundbreaking evidence on this is the large across-slope gradient in θ_v (between S1 and S3) for $135° < WD_a < 180°$. However, statistics on the wind vector from the ski-flying hill in Vikersund can be used to decide wind corridors that are sufficiently predictable in the estimate of v_{tan}. The least non-linear effects on aerodynamics are found for low standard deviation periods in the mean velocity components, and for some WD_a we also expect deviations (See 6.4). The change from $v_{ref} = -1.0$ ms^{-1} to -1.5 ms^{-1} is a dangerous area, mainly because the tilt effect over the knoll area starts to be significantly large, but is slightly compensated by a negative contribution from v_{diff}. One must take into consideration that this is evaluated on only one singular point on the y_p slope, and the integrated total effect over the whole slope profile can potentially be very different.

Speaking of the y_p integrated aerodynamical effect, we suggest that further work in

this study focuses on thinking carefully about the necessary spatial resolution of high-frequency measurements to build a picture of the **u** with a fairly good resolution. The placement of anemometers to perform the best to their purpose also becomes a key recommendation. Initially, we visualized the hill profile and did a rough estimate that 15 sonic anemometers divided into five optimal y_p (and z_p) positions would create a fairly sufficient picture of the **u** on the plane of the expected height of a ski jumper trajectory in the hill. Based on the result, indicating that the distribution of the **u** seems to be very sensitively dependent on both y_p and WD_a, where the latter variable also is likely to be dependent on y_p, we do not see any other solution than trying out adjustments of WF based on expectation in aerodynamical effects for certain mean WD_a and v_{ref} and see whether it statistically makes ski jumping fairer or not.

Another idea is to use multi-rotor unmanned air vehicles (UAV) with anemometers to measure wind in the five centers between the ten anemometers used by FIS in competitions during competitions to see if there are any non-linear effects on the mean center wind.

Recently, media coverage and videography have developed quickly after video coverage from drones was introduced at Vikersund World Championships in 2022 (*Løn-ning*, 2022). Spectacular footage of ski jumpers only a few meters ahead of the drone justifies suggesting that this also can be used for wind measurements a couple of seconds ahead of the ski jumper (instead of behind). Ongoing studies about UAVs and the wake propagation created by their rotors allow users to be ensured accurate sensor data and safe operation (*Throneberry et al.*, 2022).

If for some reason this kind of drone activity is considered too risky, it can also be done in the waiting periods where competitions are postponed due to wind outside a wind corridor based on statistics done with $\overline{U}_{3nc}$. This procedure will either verify the expected uncertainty due to the mean magnitude of the crosswind, or it can disprove it by seeing a confined and inside corridor stationary difference from the reference wind.

Appendix A

Appendix

A.1 List of Abbreviations

Table A.1: List of Abbrevations

ABL	Atmospheric Boundary Layer
CNR	Carrier to Noise Ratio
α_{scan}	azimuth/horizontal direction of scan
SA, S1, S2, S3	Sonic Anemometer, Sonic 1, Sonic 2, Sonic 3
S_{ref}	$\frac{S1+S2}{2}$
ppi or PPI	Plan Position Indicator
rhi	Range Height Indicator
FIS	the International Ski Federation
UAV	multi-rotor unmanned air vehicle
WF	Wind Factor
Δl_{WF}	WF compensation model output of JL effect
K (K-point)	critical point; kind of an expected radial length for a ski jumper giving 60 length points.
CFD	Computational Fluid Dynamics
HW	headwind (i.e positive v-component)
TW	tailwind (i.e v<0)
u_r,v_r,v_{rl},w_r	wind components rotated along the plane created by the mean wind direction (rl - rotated along LiDAR scan plane)
WS	horizontal absolute wind speed (often very close to the magnitude of v_r)
LiDAR	Light Detecting and Ranging
RH	relative humidity
WC100s	LiDAR WindCube 100s
Φ_a	azimuth scan angle
Φ_v	scan elevation
VH	Vikersund ski flying hill
X_{10min}, X_{10sec}	10 minute means, 10 second means
c	speed of sound
q	specific humidity
P_{300}	set of two periods with total length of 300 h {0900 UTC Oct 12 to 2300 UTC Oct 18, 1630 UTC Oct 20 to 1430 UTC Oct 26}
WD_a	Horizontal wind direction
AoA or $\alpha_{1,2,3,ref}$	angle of attack wind vector for S1, S2, S3 and reference respectively
$\sigma_{X1,X2,X3,Xref}$	block standard deviation of variable X for S1, S2, S3 and reference respectively
v_{rl}	LiDAR scan radial velocity component with α_{scan} = 34.54^o
UTC	Coordinated Universal Time
LT	Local Time
v_{tan}	tangential wind speed (rotation of 28.1° on SA positions)
$\overline{v_{tan}}$	weighted 5 s temporal mean in FIS competitions
$\overline{v_{ref}}$	replica of $\overline{v_{tan}}$ estimated from S1 and S2 measurements
$\overline{v_{diff}}$	reference deviation to the center wind v^{S3} (Term I in F1)
QC/QA	quality control/quality assurance
$\theta_{1,2,3}$	azimutal rotation for S1, S2 and S3 respectively
F1	tangential wind speed function
θ_v	tilt of the wind vector with respect to the xy plane
v_{θ_v}	Wind vector tilt effect (term II in F1)

A.2 LiDAR (WC100s) Scans: Oct 12 to Oct 26 2021

The output data given from the WC100s is a one-dimensional velocity component in the radial direction of the scan. Elevation is set to 34.53^o in the default scan loop (ppi), whereas the azimuth (α_{scan}) is changed at a constant rate of $1^o s^{-1}$ and through 24 individual horizontal angles separated by 0.5^o. Which means the scan sector is in total 12 degrees wide ($-5^o < \alpha_{scan} < 7^o$). This scan interval is fixed through the campaign, and uncertainty in the horizontal scan angle is in the same order as for the vertical scan angle (0.05 degrees). One way to capture changes in horizontal orientation is to use data output of Carrier to Noise Ratio (CNR) and detect the position of the pole with the Sonic Anemometers on. The resolution of the grid points at this position is 1 meter, and 0.05 degrees is 10 cm. The elevation, however, is measured as a time series by the LiDAR by an inclinometer level build inside the instrument. Elevation of the scan through the 16 day period can be seen in Fig. A.1. A linear regression of the expected elevation is the following

$$\overline{\beta_{scan}} \;=\; 34.531 + 0.016 \;-\; r \cdot t, \quad r = \frac{0.001 - 0.016}{13} = -0.00115... \tag{A.1}$$

where r is the rate of increase in ${}^o\text{day}^{-1}$, and t is time in days after Oct 13 2021. There is a small systematic error by the WC100s of $< |\pm 0.001^o|$ that corresponds to $3mm$ at 180 meter distance from the scan. This is so small it will be neglected in this study.

However, an uncertainty connected to the change in leveling of the wooden platform, cannot be neglected. Pitch and roll for the instrument due to movement of platform can be seen In Table 3.1. The pitch is added to scan elevation displayed in the data, so the expected true elevation changes linearly from 34.546 ° to 34.531 ° as shown in eq.A.1.

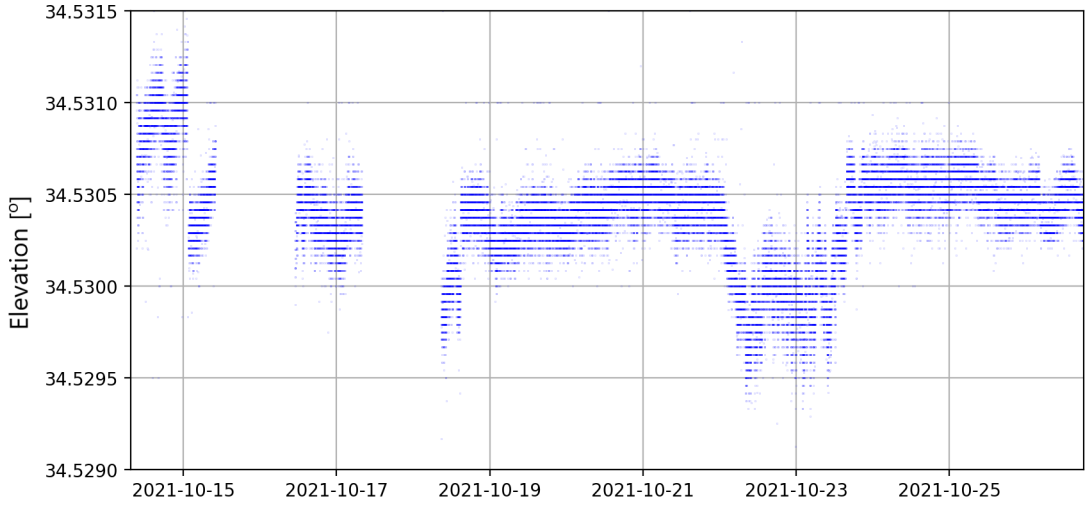

Figure A.1: time series of elevation for the default scan.

A.2.1 Validation of LiDAR (WC100s) Data

Firstly, filtering away data where CNR - values are outside a threshold is important because of the range of the LiDAR varies with atmospheric conditions. Only data of RV where $-28dB < CNR < 0dB$ is analyzed in this study. Secondly, measurements from SA in comparison to the LiDAR data are used to set a limit of a maximum spatial mean. The instantaneous values on one point must not exceed (a factor times perhaps?) maximum/minimum value of a 3 second period (measured by SA) around the time the LiDAR scan was done.

A.2.2 Synchronizing LiDAR - and SA Timestamps

If it is going to be plausible to use SA data for validating quality on LiDAR data, it becomes important to have synchronized TIMESTAMP on the two instruments. S1,S2 and S3 are/is connected to the same datalogger (Campbell Scientific CR3000) and the TIMESTAMP is the reference time for both instruments (LiDAR and SA). Since both systems are connected to a GPS, the times should be similar to the Greenwitch mean time (GMT). However, correlation analysis of RV measured by S3 (1 second mean) and RV measured by LiDAR around point S3 (spatial average 6 m^2) indicates a time difference of around 1 minute in the period Oct 24, 1630 UTC to Oct 25, 11:30 UTC. The precision of the synchronisation will have to be within $\pm$ 1 second. This is mainly because a 1 second difference in time is also a corresponding scan distance of 1 degree. So there will be deviations in the true RV (in the time and position of both instruments when compared) both due to the time difference, but also due to spatial difference. A scatter plot of the two instruments measurement of RV is plotted in figure 13, and illustrates the significant correlation difference between the not synchronized time series (a) and the synchronized time series (b) with R=0.49... and R=0.80... respectively.

In addition, all LiDAR measurements where $-4\ m\ s^{-1} < RV < 4\ m\ s^{-1}$ is removed. This is because above 99.7 % of the RV from SA3 happens to be inside this interval. This corresponds to 3 standard deviations, and this limit is also used detecting spikes in the raw data from the SA.

A.3 Sonic Anemometer (SA): Oct 12 to Oct 26

Raw data retrieved from each three SA (n=1,2,3) is the four variables u_n, v_n, w_n and T_n. This gives a total of 12 variables and one time vector. All three SA measured and gave an output value with 20 Hz sampling frequency. One variable measured by one sonic corresponds to $2.5 \cdot 10^7$ data outputs. The raw data also have an output variable called $diag\_wind\_n$ which is an integer counting periodical between the number 0 and 63 (2^6) total bins (explanation on this please?). The concept of the sampling is explained in detail in section 3.1. The raw data is plotted in a catalogue containing 114 subplots of u_n, v_n, w_n and T_n with a mean value and a mean σ_n calculated with method "block" and with period of 10 minutes (18 "block" σ_n).

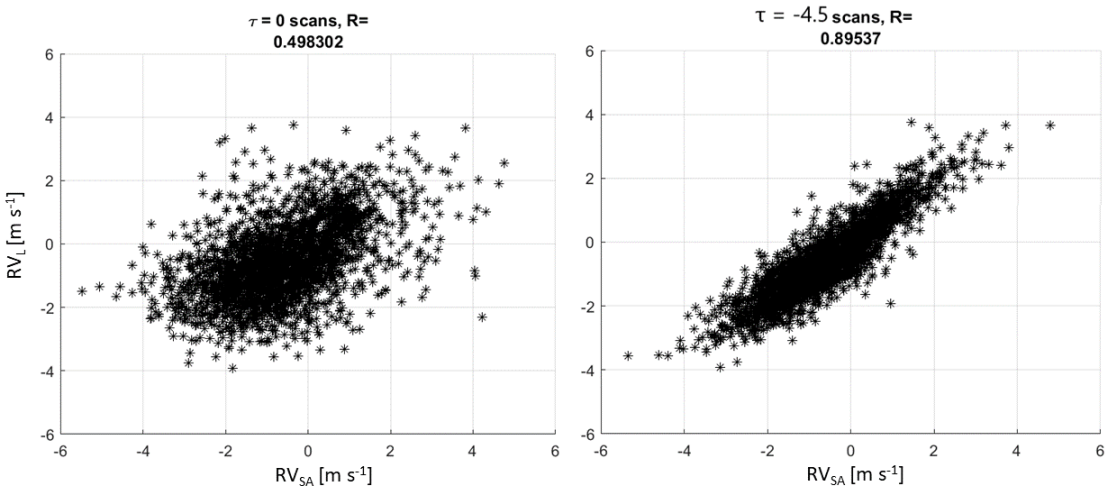

Figure A.2: scatter plot of 1 second mean S3 measurement of RV (X-axis) and 6 grid cell spatial mean of RV where time series are shifted. (a): $\tau = 0$ and (B): $\tau = -4.4$ LiDAR scans. One LiDAR scan is 14 seconds.

A.3.1 Validation of SA Data

Spikes is removed using MATLAB script gfi_spikes. The MATLAB function gives output of indexes in the data that is a spike according to the inputs you give the function.

$$[\text{ind}_r, \text{ind}_c] = \text{gfi\_spikes}(\text{data}_n, \text{thres}, \text{win}, \text{cons\_spikes}, \text{time\_dim}, \text{method}, \text{thr\_mode}) \quad \text{(A.2)}$$

where inputs used in this study were chosen in a window of 10 minutes which is the default mean wind window used in a weather forecast. The threshold is chosen to $3 \cdot MAS$ such that 99.7% of the data is retained assuming the data is perfectly stochastic within a true variance. The inputs is as the follows

$$\begin{aligned} \text{data}_n &= u_{xn}, u_{yn}, u_{zn}, T_n \\ \text{thres} &= 3 \cdot MAS \\ \text{win} &= 12000 \text{ bins} \\ \text{cons\_spikes} &= 3 \\ \text{method} &= \text{"MAS"} \end{aligned}$$

Maximum consecutive spikes of 3 is also used since values outside of $3 \cdot \omega_n$ might not be spikes, especially if the trend of the variable is consistent with the extreme value of the data.

A.4 Competition Analysis in Vikersund World Championship

Results after six rounds of approximately 30 jumps in Vikersund in the World Championship weekend (Mar 10 to Mar 12 2022) showed very little correlation between jump length and radial wind conditions. In Fig. A.3, none of the 6 rounds shows a significant positive correlation, which the use of WFC expects given that each competitor gets completely random wind conditions. The strongest positive correlation, with p=0.11, has a very steep incline. This is expected to be because of the fact that the TW-conditions decreased from $-1.5 < V_{ref} < -1.2\ ms^{-1}$ in the first half time of the round, and increased to $V_{ref} > -1\ ms^{-1}$ at the end of the round which is when the ski jumpers with the best form from this season were jumping. In round 4 we have a negative correlation, which is the opposite effect where the best jumpers have a bit worse conditions, so the longest jumps appear here.

The negative correlation of -0.30 appearing in round 5 could have different explanations, for example, the wind vector tilt effect v_{θ_v} if the strongest TW was close to the area where the curvature of the ski flying slope is the largest. The first anemometer at 10 %, which gives negative compensation for TW there (*Czarnecki*, 2020), is only based on the fact that the loss of drag due to TW is more beneficial for the positive y-acceleration than it is disadvantageous for the negative z-acceleration.

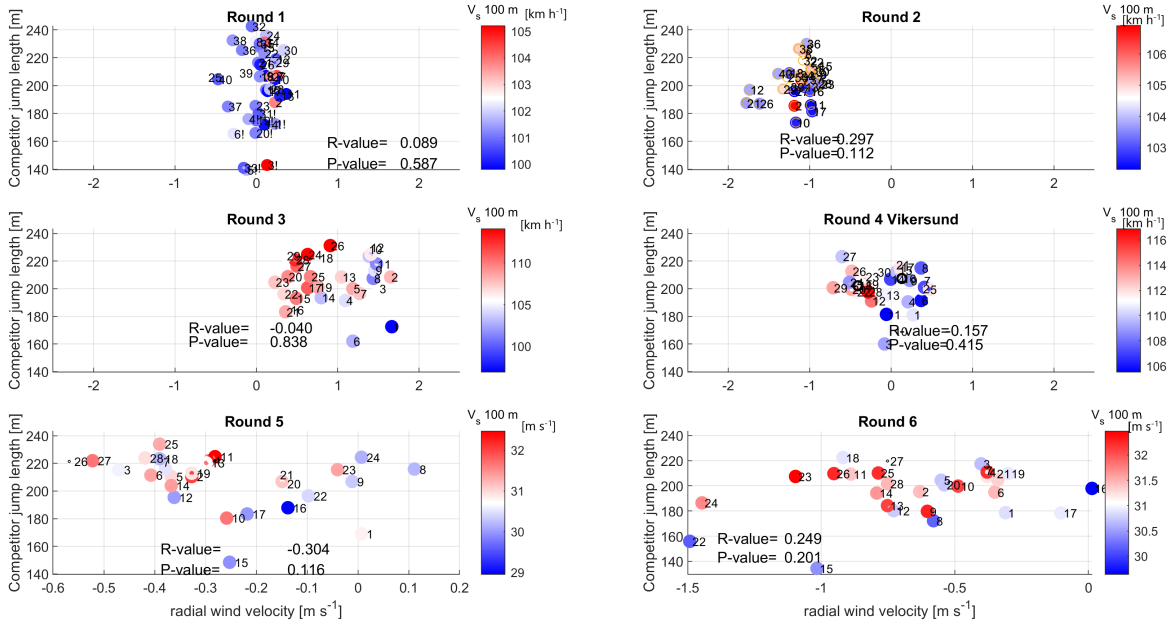

Figure A.3: Scatter plot of jump length as a function of the average tangential wind effect measured as a 5-second mean for each anemometer position in the hill. Rounds 3, 4, and 6 changed the gate (G) during the race, and the fixed lengths are $\frac{-7.3}{1.2} \cdot \Delta G$ *Shading is the competitors speed in the position of jump length = 100 m. Note that rounds 5 and 6 are team competitions, so the number is not correlated with the competitor's form. Results and WF compensation are collected from (Dolhar and Greger, 2022).*

Bibliography

Aldrin, M. (2015), Fair compensation for gate and wind conditions in ski jumping estimated from competition data using a mixed model, *Journal of Quantitative Analysis in Sports*, *11*(4), 231–245, doi:doi:10.1515/jqas-2015-0022. 1, 2.4.4, 6.1.2

Campbell Scientific (2022), CSAT3, https://www.campbellsci.com/csat3, accessed: 2022-12-02. 3.3.1

Carvalho, D., A. Rocha, C. Silva Santos, and R. Pereira (2013), Wind resource modelling in complex terrain using different mesoscalemicroscale coupling techniques, *Applied Energy*, *108*, 493–504, doi:doi.org/10.1016/j.apenergy.2013.03.074. 2.4.1

Czarnecki, M. (2020), Graduate programme major: Advanced analytics-big data optimisation of the wind factor compensation in ski jumping, Ph.D. thesis, the Institute of Econometrics. 1, 2.4.2, 2.4.5, 4.1.3, 4.2, 5.3, 6.1.2, 6.2, A.4

Dolhar, A., and I. Greger (2022), Fis ski fying world championship 2022, https://www.fis-ski.com/DB/general/event-details.html?sectorcode=JP&eventid=49466&seasoncode=2022, accessed: 2022-03-12. 2.2, A.3

El-Madany, T., H. F. Duarte, D. J. Durden, B. Paas, M. J. Deventer, J.-Y. Juang, M. Y. Leclerc, and O. Klemm (2014), Low-level jets and above-canopy drainage as causes of turbulent exchange in the nocturnal boundary layer, *Biogeosciences*, *11*, 4507, doi:doi.org/10.5194/bg-11-4507-2014. 5.3.3

FIS (2022), Seven things you should know before the season 2022/23, https://www.fis-ski.com/en/ski-jumping/ski-jumping-news-multimedia/news/2022-23/seven-things-you-should-know-before-the-season-2022-23, accessed: 2022-11-03. 1

Gergely, M., and T. J. Garrett (2016), Impact of the natural variability in snowflake diameter, aspect ratio, and orientation on modeled snowfall radar reflectivity, *Journal of Geophysical Research: Atmospheres*, *121*(20), 12,236–12,252, doi:doi.org/10.1002/2016JD025192. 5.1.3

Goger, B., M. W. Rotach, A. Gohm, and I. Stiperski (2018), The impact of three-dimensional effects on the simulation of turbulence kinetic energy in a major alpine valley, *Boundary-Layer Meteorology*, *168*(1), 1–27. 2.2.1

Ha, S., and M. Kim (2020), Challenges of designing and carrying out laboratory experiments about newton's second law: The case of korean gifted students, *Science & education*, *29*(5), 1389–1416, doi:1doi.org/10.1007/s11191-020-00155-1. 2.1

Hosch, W. L. (2009), Navier-stokes equation, https://www.britannica.com/science/Navier-Stokes-equation, accessed: 2020-05-28. 2.1

House, M. H. (2022), Edition november 2022 the international ski competition rules (icr), https://assets.fis-ski.com/image/upload/v1671441414/fis-prod/assets/ICR_Ski_Jumping_2023_clean.pdf, accessed: 2022-18-02. 2.4.4

Jung, A., W. Müller, and M. Staat (2018), Wind and fairness in ski jumping: A computer modelling analysis, *Journal of Biomechanics*, *75*, 147–153, doi:doi.org/10.1016/j.jbiomech.2018.05.001. 2.4.4, 2.4.5

Jung, A., W. Müller, and M. Virmavirta (2021a), A heuristic model-based approach for compensating wind effects in ski jumping, *Journal of Biomechanics*, *125*, 110,585, doi:https://doi.org/10.1016/j.jbiomech.2021.110585. 1, 2.4.5, 4.2, 6.1.2

Jung, A., W. Müller, and M. Virmavirta (2021b), A heuristic model-based approach for compensating wind effects in ski jumping, *Journal of biomechanics*, *125*, 110,585–110,585. 2.4

Jung, A., W. Müller, and M. Staat (2021c), Corrigendum to wind and fairness in ski jumping: A computer modelling analysis [j. biomech. 75 (2018) 147153], *Journal of Biomechanics*, *75*, 128, doi:doi.org/10.1016/j.jbiomech.2021.110690. 2.4.4

Kavaya, M. J., J. Y. Beyon, G. J. Koch, M. Petros, P. J. Petzar, U. N. Singh, and J. Yu (2014), The doppler aerosol wind (dawn) airborne, wind-profiling coherent-detection lidar system: Overview and preliminary flight results, *Journal of Atmospheric and Oceanic Technology*, *31(4)*, 826–842, doi:10.1175/JTECH-D-12-00274. 3.3.2

Langleben, M. P. (1954), The terminal velocity of snowflakes, *Quarterly Journal of the Royal Meteorological Society*, *80*(344), 174–181, doi:doi.org/10.1002/qj.49708034404. 5.1.3

Lønning, S. (2022), Tv-bildene fra vm i skiflyging begeistrer. norsk firma står bak den unike seeropplevelsen, https://www.nettavisen.no/sport/rystet-en-hel-ski-verden-na-vekker-bildene-fra-vikersund-oppsikt/s/12-95-3424255352. 7

Macchiavelli, A. O., R. F. Casten, R. M. Clark, H. L. Crawford, and P. Fallon (2020), Coriolis coupling in the continuum, *Journal of physics*, *1610*(1), 12,008, doi:doi.org/10.1088/1742-6596/1610/1/012008. 2.1

Markowski, P., and Y. Richardson (2010), *Mesoscale Instabilities*, chap. 3, pp. 41–70, John Wiley & Sons, Ltd, doi:doi.org/10.1002/9780470682104. 2.2, 2.3.1, 2.2

Maryniak, J., E. adyyska Kozdra, and S. Tomczak (2009), Configurations of the graf-boklev (v-style) ski jumper model and aerodynamic parameters in a wind tunnel, *Human movement*, *10*(2), 130–136. 2.4

Mataji, M. (2022), On the extension of streamwise turbulence intensity profile beyond the atmospheric surface layer under neutral to unstable stratifications, *Journal of Wind Engineering and Industrial Aerodynamics*, *228*, 105,100, doi:https://doi.org/10.1016/j.jweia.2022.105100. 2.3.1

Mathis, S., S. Palacios, and J.-P. Zahn (2004), On shear-induced turbulence in rotating stars, *A&A*, *425*(1), 43–247, doi:10.1051/0004-6361:20040279. 6.1

Mauder, M., M. Cuntz, C. Drüe, A. Graf, C. Rebmann, H. P. Schmid, M. Schmidt, and R. Steinbrecher (2013), A strategy for quality and uncertainty assessment of long-term eddy-covariance measurements, *Agricultural and Forest Meteorology*, *169*, 122–135, doi:https://doi.org/10.1016/j.agrformet.2012.09.006. 4.1.2

Mikko, V., and K. Juha (2022), The effect of wind on jumping distance in ski jumping depends on jumpers aerodynamic characteristics, *Journal of Biomechanics*, *137*, 111,101, doi:https://doi.org/10.1016/j.jbiomech.2022.111101. 1, 2.4.4, 6.1

Mohr, M., T. Laemmel, M. Maier, and D. Schindler (2017), Spatial variability of wind-induced air pressure fluctuations responsible for pressure pumping, *Tellus*, *69*(1), doi:doi.org/10.1080/16000889.2017.1361757. 2.2.3

Muhammad, A. (2021), A study on skewness and kurtosis estimators of wind speed distribution under indeterminacy, *Theoretical and Applied Climatology*, *143*(3-4), doi:doi.org/10.1007/s00704-020-03509-5. 2.3.2

Müller, W., D. Platzer, and B. Schmölzer (1996), Dynamics of human flight on skis: Improvements in safety and fairness in ski jumping, *Journal of Biomechanics*, *29*(8), 1061–1068, doi:doi.org/10.1016/. 2.4.2

Nils (2023), Scatter plot colored by kernel density estimate, Nils(2023).ScatterPlotcoloredbyKernelDensityEstimate(https://www.mathworks.com/matlabcentral/fileexchange/65728-scatter-plot-colored-by-kernel-density-estimate, accessed: 2023-15-03. 6.2

Norwegian Meteorological Institute (2023), AROME Arctic Archive, https://thredds.met.no/thredds/catalog/aromearcticarchive/catalog.html, accessed: 2023-03-10. 5.3.2

Pietschnig, J., M. Pellegrini, J. S. N. Eder, and M. Siegel (2020), After all, it is an outdoor sport: Meta-analytic evidence for negative associations between wind compensation points and round scores in ski jumping competitions, *PloS one*, *15(8)*, e0238,101, doi:10.1371/journal.pone.0238101. 1, 2.4.5

Rampanelli, G., D. Zardi, and R. Rotunno (2004), Mechanisms of up-valley winds, *Journal of the atmospheric sciences*, *61*(24), 3097–3111. 2.2.2

Slyz, A. D., J. E. G. Devriendt, G. Bryan, and J. Silk (2005), Towards simulating star formation in the interstellar medium, *Monthly Notices of the Royal Astronomical Society*, *356*(2), 737–752, doi:10.1111/j.1365-2966.2004.08494.x. 2.3.2

Straumann, R. (1927), Vom skiweitsprung und seiner mechanik, in *Jahrbuch des Schweizerischen Ski Verbandes*, pp. 34–64, Selbstverlag des SSV, Bern. 2.4.2

Stull, R. (1988a), *An Introduction to Boundary Layer Meteorology*, 35-44,198-205 pp., Kluwer Academic Publishers, Dordrecht, Boston and London. 2.2, 2.2.1, 2.2.1, 2.3, 2.3.1, 2.3.1, 2.3.1, 2.3.1, 2.3.2, 2.4.1

Stull, R. (1988b), *An Introduction to Boundary Layer Meteorology*, 1-34 pp., Kluwer Academic Publishers, Dordrecht, Boston and London. 2.2, 2.3.1, 2.3.1

Sumner, D., J. Heseltine, and O. Dansereau (2004), Wake structure of a finite circular cylinder of small aspect ratio, *Exp Fluids*, *37*, 720–730, doi:10.1007/s00348-004-0862-7. 6.1.2

Throneberry, G., A. Takeshita, C. M. Hocut, F. Shu, and A. Abdelkefi (2022), Wake propagation and characteristics of a multi-rotor unmanned vehicle in forward flight, *Drones*, *6*(5), doi:10.3390/drones6050130. 7

Tonboe, R. T., V. Nandan, J. Yackel, S. Kern, L. T. Pedersen, and J. Stroeve (2021), Simulated ka- and ku-band radar altimeter height and freeboard estimation on snow-covered arctic sea ice., *The Cryosphere*, *15(4)*(6), 1811–1822, doi:doi.org/10.5194/tc-15-1811-2021. 2.1

Turner, D. B. (1986), Comparison of three methods for calculating the standard deviation of the wind direction, *Journal of Applied Meteorology and Climatology*, *25*(5), 703 – 707, doi:10.1175/1520-0450(1986)025<0703:COTMFC>2.0.CO;2. 2.3.1, 4.1.4

Villagrasa, D. M., M. Lehner, C. D. Whiteman, S. W. Hoch, and J. Cuxart (2013), The upslopedownslope flow transition on a basin sidewall, *Journal of Applied Meteorology and Climatology*, *52*(12), 27152734, doi:doi.org/10.2307/26175931. 2.2.3

Virmavirta, M., and J. Kivekäs (2012a), The effect of wind on jumping distance in ski jumping - fairness assessed, *Sports biomechanics / International Society of Biomechanics in Sports*, *11*, 358–69, doi:10.1080/14763141.2011.637119. 1, 2.4.5, 6.1.2

Virmavirta, M., and J. Kivekäs (2012b), The effect of wind on jumping distance in ski jumping fairness assessed, *Sports Biomechanics*, *11*(3), 358–369, doi:10.1080/14763141.2011.637119, pMID: 23072046. 2.4.4

Virmavirta, M., and J. Kivekäs (2012c), The effect of wind on jumping distance in ski jumping fairness assessed, *Sports Biomechanics*, *11*(3), 358–369, doi:10.1080/14763141.2011.637119, pMID: 23072046. 4.1.3

Virmavirta, M., and J. Kivekäs (2019), Aerodynamics of an isolated ski jumping ski, *Sports Enginering*, *22*, 111,101, doi:https://doi.org/10.1007/s12283-019-0298-1. 2.4.5, 4.2, 4.2

Weeger, O. (2022), Vikersund skifygingsbakke, http://www.skisprungschanzen.com/EN/Ski+Jumps/NOR-Norway/30-Viken/Vikersund/0005-Skiflygingsbakke/, accessed: 2022-03-10. 3.1, 3.1, 3.2

Zikanov, O. (2010), *Essential Computational Fluid Dynamics*, John Wiley & Sons, Incorporated. 2.1